

# Dynamic behaviour of brittle materials and systems

13th Technical Meeting, 2001  
Saint-Jean-de-Luz, France

# ON THE BEHAVIOUR OF GEOLOGIC MATERIALS UNDER SHOCK WAVE LOADING

K. Tsembeles, W.G. Proud, and J.E. Field

*PCS, Cavendish Laboratory, Madingley Road, Cambridge, CB3 0HE. UK.*

## 1. ABSTRACT

*A series of plate impact experiments has been performed on cement paste and dolerite igneous rock to assess their longitudinal and lateral properties under shock wave compression. The stress components were measured using embedded manganin gauges. Longitudinal stresses in cement paste and grout spanned a range of 0.21-6.20 GPa and 5.16-11.34 GPa respectively, while the lateral stresses spanned a range of 0.09-4.69 GPa and 1.01-6.86 GPa. The dynamic shear stress can be determined by comparison of the longitudinal and lateral stress histories. Results indicate that the cement paste is behaving in an inelastic manner with the shear stress increasing with increasing shock pressure. For the dolerite, results indicate that the longitudinal behaviour is elastic for the stress range involved although shear stresses show deviation from elastic loading for longitudinal stresses higher than 4.3 GPa. Results for both materials are compared with published data for concrete and other geological materials.*

## 2. INTRODUCTION

Considerable interest in characterising the dynamic loading of concrete under impact conditions exists because of its extensive use as a structural material [1-4]. Concrete is a heterogeneous material containing aggregates in a cement matrix, therefore, its response is complicated compared to homogeneous materials. For instance, impedance differences inside the concrete emanating from its constituents lead to local variations in the particle velocities, longitudinal and lateral stresses. One way to study this material is to average these variations using a reverse impact technique, where a disc-shaped concrete specimen is mounted on the projectile which undergoes planar impact on a stationary target of PMMA, copper, or tantalum which is instrumented [1-4]. Only the Hugoniot curve (longitudinal behaviour) can be found using this technique. To determine the constitutive behaviour of the material, the lateral stresses need to be measured. Overall, the material characterisation has been built-up from studies of the matrix (cement paste) and geological materials separately.

The Hugoniot and lateral experiments performed on cement paste and dolerite are presented. Dolerite (also known as Diabase) is a fine-to medium-grained, dark grey to black intrusive igneous rock [5]. Chemically and mineralogically, it closely resembles the volcanic rock basalt, but it is somewhat coarser and contains glass, with increased grain size it resembles gabbro for which data exists in the literature [6].

### 3. EXPERIMENTAL PROCEDURE

All experiments were carried out in the plate impact facility at the University of Cambridge [7], which consists of a single stage 50 mm, bore light gas gun. This is capable of achieving velocities up to  $1200 \text{ m s}^{-1}$ . The impactor materials consisted of polymethylmethacrylate (PMMA), aluminium, lapped copper and tungsten. Impact velocities were measured to an accuracy of 0.5% using a sequential pin-shorting method and the target was aligned to the impactor to less than 1 mrad by means of an adjustable specimen mount. To measure the Hugoniot of the cement paste,

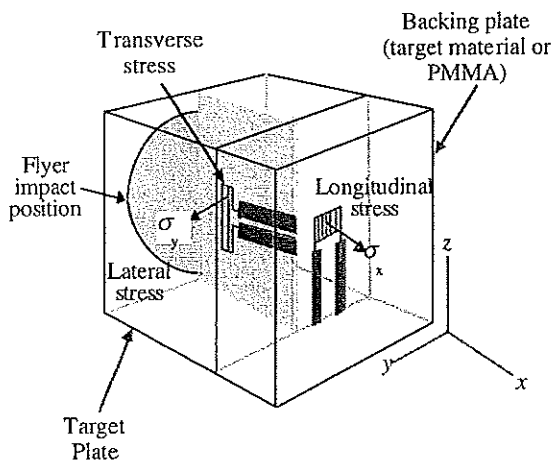


**Figure 1:** Target configuration

manganin stress gauges (MicroMeasurements type LM-SS-210FD-050) were embedded between tiles 2-4 and 4-20 mm, thick. For Dolerite, the tiles were 8 mm and 17 mm thick. One sample of Dolerite was prepared with the stress gauge supported on the rear surface with a block of (PMMA). In such a configuration the gauge had a faster rise time due to the impedance match of the PMMA, epoxy adhesive and the gauge materials. Specimens for lateral gauge experiments were sectioned in two, and commercial stress gauges (J2M-SS-580SF-025) were introduced 2 and 7 mm, from the impact surface of each cement paste sample and 3 and 8 mm for dolerite. Samples were assembled using a low viscosity epoxy with a curing time of approximately 24 hours. Lateral gauge data were reduced using the analysis of Rosenberg and Partom [8]. The shear stress ( $\tau$ ) of the material can thus be calculated through knowledge of the longitudinal ( $\sigma_x$ ) and lateral stresses ( $\sigma_y$ ) through the relation,

$$2\tau = \sigma_x - \sigma_y \quad (1)$$

Our method of determining the shear stress has the advantage of being a direct measure, which does not rely on computation of the hydrostat.

#### 4. MATERIAL DATA

The cement paste and Dolerite used in this study were supplied by Concrete Structures Section (CSS), Department of Civil & Environmental Engineering, Imperial College, London, UK. The paste had a water-to-cement ratio of 0.35 by weight. Specimens were cured for 21 days in a water-bath at 20 °C. The density and ultrasonic measurements were performed for each batch after the sample surfaces were ground flat. The density was  $2000 \pm 200 \text{ kg m}^{-3}$ , while the longitudinal and shear elastic wave velocities, were  $3.70 \pm 0.20$  and  $2.20 \pm 0.20 \text{ mm } \mu\text{s}^{-1}$ , respectively. Density variations resulting from different initial porosity were in agreement with independent measurements performed by CSS.

Dolerite was sent as a single block weighting over 20kg. It was cut into smaller specimens with dimensions 8-20 mm x 50 mm x 50 mm. Density and ultrasonic measurements were performed on several samples after grinding. The density was  $2894 \pm 27 \text{ kg m}^{-3}$ , while the longitudinal and shear elastic wave speeds were  $5.89 \pm 0.07$  and  $3.34 \pm 0.11 \text{ mm} \cdot \text{s}^{-1}$ , respectively.

#### 5. RESULTS AND DISCUSSION

##### *(i) Cement Paste*

Table 1 summarises the impact conditions and Hugoniot stresses for the longitudinal experiments, while table 2 summarises the impact conditions, lateral stresses and shear stresses obtained using equation 1 combined with the Hugoniot data. It should be noted that if multiple Hugoniot measurements correspond to a single lateral result, the mean Hugoniot value is used in equation 1.

Figures 2 and 3 illustrate some typical stress wave profiles for experiments 10HCu/9TCu and 16HCu/10TCu. The solid trace corresponds to the longitudinal stress while the dotted trace corresponds to the lateral stress. It can be seen that the longitudinal stresses have higher values than the lateral ones due to the shear strength of the material, as reflected in equation 1.

**Table 1: Cement Hugoniot Shots**

Shot no.	Impactor material and Thickness (mm)	Target front (mm)	Target back (mm)	Impact Velocity ( $m s^{-1}$ )	Stress (GPa)	Particle Velocity ( $mm \cdot s^{-1}$ )
1HAl	10 Al	2	5	250	$0.84 \pm 0.04$	$0.180 \pm 0.006$
2HAl	10 Al	2	6	511	$1.80 \pm 0.20$	$0.378 \pm 0.040$
3HAl	10 Al	4	10	359	$1.34 \pm 0.06$	$0.260 \pm 0.008$
4HPMMA	10 PMMA	3	10	228	$0.47 \pm 0.01$	$0.100 \pm 0.003$
5HCu	10 Cu	2	13	511	$2.48 \pm 0.11$	$0.442 \pm 0.020$
6HAl	10 Al	2	10	435	$1.92 \pm 0.06$	$0.298 \pm 0.010$
7HCu	10 Cu	2	10	509	$2.80 \pm 0.10$	$0.432 \pm 0.015$
8HAl	10 Al	2	10	510	$2.37 \pm 0.09$	$0.345 \pm 0.020$
9HCu	10 Cu	3	10	569	$3.30 \pm 0.20$	$0.478 \pm 0.030$
10HCu	6 Cu	2	10	641	$4.05 \pm 0.20$	$0.530 \pm 0.030$
11HAl	10 Al	2	10	484	$2.33 \pm 0.10$	$0.320 \pm 0.015$
12HAl	6 Al	2	10	548	$2.63 \pm 0.10$	$0.367 \pm 0.012$
13HAl	10 Al	2	10	314	$0.88 \pm 0.03$	$0.245 \pm 0.007$
14HAl	10 Al	2	10	510	$2.14 \pm 0.04$	$0.359 \pm 0.008$
15HCem	10 Cem	5	5	292	$1.00 \pm 0.03$	$0.228 \pm 0.006$
16HCu	6 Cu	2	20	727	$5.00 \pm 0.15$	$0.590 \pm 0.018$
17HCu	6 Cu	2	10	839	$6.20 \pm 0.19$	$0.672 \pm 0.020$
18HPMMA	10 PMMA			228	$0.47 \pm 0.01$	$0.100 \pm 0.003$
19HAl	10 Al	2	10	396	$2.01 \pm 0.08$	$0.253 \pm 0.010$
20HAl	10 Al	2	10	270	$1.24 \pm 0.05$	$0.170 \pm 0.007$
21HAl	10 Al	2	10	313	$1.37 \pm 0.05$	$0.212 \pm 0.008$
22HPMMA	10 PMMA	2	10	348	$0.97 \pm 0.04$	$0.079 \pm 0.003$
23HPMMA	10 PMMA	2	10	385	$0.95 \pm 0.04$	$0.122 \pm 0.005$
24HPMMA	10 PMMA	2	10	71	$0.21 \pm 0.01$	$0.012 \pm 0.001$
25HPMMA	10 PMMA	2	20	152	$0.44 \pm 0.02$	$0.027 \pm 0.001$

**Table 2. Experimental Parameters, Lateral Stresses and corresponding Hugoniot Data**

Shot no.	Impactor material and thickness (mm)	Impact Velocity ( $m s^{-1}$ )	Lateral Stress (GPa)	Corresponding Longitudinal Stress (GPa)	2*Shear Stress (GPa)
1TAl	10 Al	352	$1.00 \pm 0.03$	$1.34 \pm 0.06$	$0.34 \pm 0.09$
2TAl	10 Al	512	$2.00 \pm 0.06$	$2.25 \pm 0.12$	$0.25 \pm 0.18$
3TAl	10 Al	261	$0.52 \pm 0.02$	$0.84 \pm 0.04$	$0.32 \pm 0.06$
4TAl	10 Al	438	$1.39 \pm 0.04$	$1.92 \pm 0.06$	$0.53 \pm 0.10$
5TAl	10 Al	440	$1.35 \pm 0.03$	$1.92 \pm 0.06$	$0.57 \pm 0.09$
6TCu	10 Cu	499	$2.28 \pm 0.05$	$2.64 \pm 0.16$	$0.36 \pm 0.21$
7TCu	10 Cu	569	$2.66 \pm 0.08$	$3.30 \pm 0.20$	$0.64 \pm 0.28$
8TAl	10 Al	514	$1.64 \pm 0.14$	$2.25 \pm 0.12$	$0.61 \pm 0.26$
9TCu	10 Cu	635	$2.94 \pm 0.15$	$4.05 \pm 0.20$	$1.11 \pm 0.35$
10TCu	6 Cu	724	$3.75 \pm 0.15$	$5.00 \pm 0.15$	$1.25 \pm 0.30$
11TPMMA	10 PMMA	229	$0.09 \pm 0.01$	$0.47 \pm 0.01$	$0.38 \pm 0.02$
12TCu	10 Cu	846	$4.69 \pm 0.10$	$6.20 \pm 0.20$	$1.51 \pm 0.50$

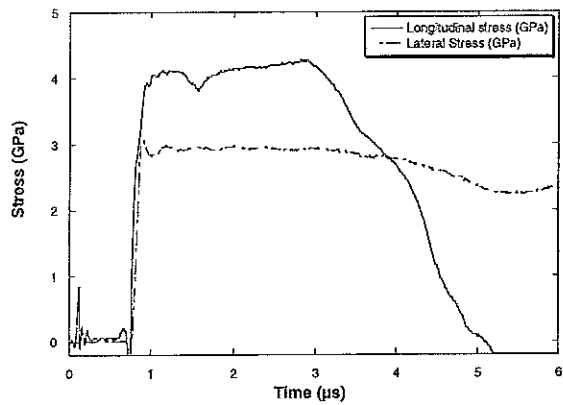


**Figure 2:** Stress Wave Profiles for Experiments 10HCu/9TCu

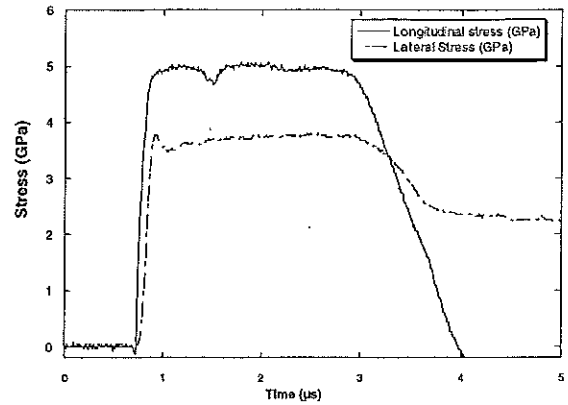


**Figure 3:** Stress Wave Profiles for Experiments 16HCu/10TCu

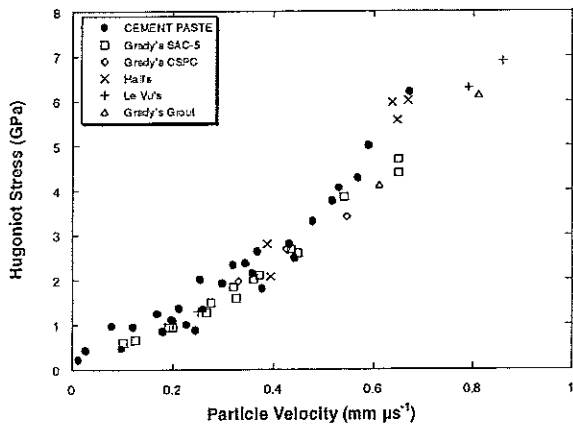


**Figure 4:** Hugoniot of Cement Paste and various Concretes

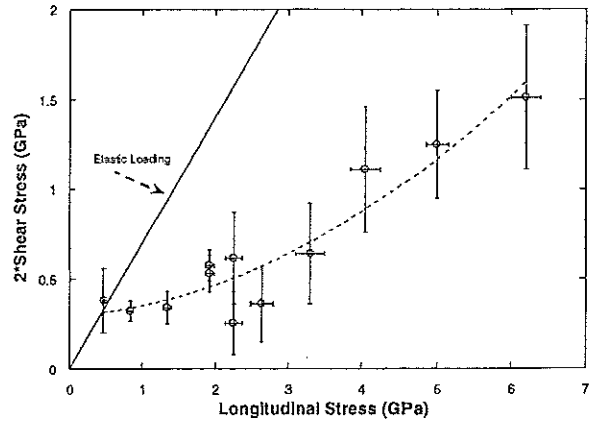


**Figure 5:** Cement paste shear response

Figure 4 shows the cement paste Hugoniot together with 4 different concretes and grout from the literature [1-4, 15]. The Hugoniot Elastic Limit (HEL) was estimated, from the stress profiles which showed a two-wave structure, to be  $0.30 \pm 0.05$  GPa; the particle velocity at the HEL was  $40 \pm 10$  m s<sup>-1</sup>. It can be seen that the data are tightly grouped, suggesting that the inclusion of aggregates does not significantly affect the Hugoniot curve up to stresses of 6 GPa. In addition, there is scatter in the cement paste data up to *ca.* 3 GPa. This can be attributed to differences in the relative humidity of the samples; however, above 3 GPa the scatter reduces. It is believed that up to 3 GPa the porous collapse is affected by differences in humidity and porosity while at higher

stresses the components' compressibility takes over and differences in humidity play a secondary role. Further experiments are under way at higher stresses to assess this hypothesis.

Figure 5 illustrates the lateral data. The shear stress data, calculated from equation 1, are plotted against longitudinal stress. As a comparison, the data are also fitted to the assumed elastic behaviour given by the equations

$$\sigma_y = \frac{\nu}{1-\nu} \sigma_x \quad (2a)$$

and

$$2\tau = \frac{1-2\nu}{1-\nu} \sigma_x \quad (2b)$$

where  $\sigma_y$  is the lateral stress,  $\sigma_x$  is the longitudinal stress,  $\tau$  is the shear stress and  $\nu$  is the Poisson's ratio of the material (0.23). It can be seen that, within the scatter due to the nature of the cement paste, the material behaviour deviates from the purely elastic behaviour around the HEL, in addition, the shear stress increases with increasing impact stress. Some process such as fracture, or pore collapse, reduces the strength, while the shear stress exhibits pressure dependence, indicative of the brittle granular nature of the material. Similar behaviour has been observed in certain filled glasses [9] where the shear stress of the damaged material deviates from the elastic loading line also increasing with pressure.

#### *ii) Dolerite*

Table 3 summarises the impact conditions and Hugoniot stresses for the longitudinal experiments, while table 4 summarises the impact conditions, lateral stresses and shear stresses obtained using equation 1 and the Hugoniot data. Figures 6 and 7 illustrate some typical longitudinal and lateral stress wave profiles for experiments 1Hdol/1Tdol and 4Hdol/4Tdol, respectively (see Tables 1 and 2 for impact conditions). The solid trace corresponds to the longitudinal stress while the dotted traces correspond to the lateral stresses at the two different gauge positions. It can be seen that the longitudinal stresses have higher values than the lateral ones and their difference leads to the shear stress inside the material according to equation 1. Figure 8 illustrates the Dolerite Hugoniot curve together with the Hugoniot data for Gabbro and Diabase [10-12]. It can be seen that all data are tightly grouped.

**Table 3:** Experimental parameters and results for longitudinal data and Hugoniot points

Shot no.	Impactor material (mm)	Target Front (mm)	Target Back (mm)	Impact Velocity ( $\text{m s}^{-1}$ )	Hugoniot Stress (GPa) $\pm 3\%$	Particle Velocity ( $\text{mm} \cdot \text{s}^{-1}$ ) $\pm 3\%$
1Hdol	10 Cu	8.26 Dol	17.16 Dol	519	6.08	0.35
2Hdol	10 Cu	8.20 Dol	17.22 Dol	702	8.39	0.48
3Hdol	10 Cu	7.69 Dol	17.25 Dol	833	10.17	0.57
4Hdol	6 W	7.35 Dol	8.40 Dol	815	11.34	0.67
1Bdol	10 Cu	6.8 Dol	12 PMMA	451	4.36	0.33

**Table 4:** Experimental parameters and results for lateral data and shear stresses

Shot no.	Impactor material (mm)	Impact Velocity ( $\text{m s}^{-1}$ )	Lateral Stress (GPa) $\pm 4\%$	2 * Shear Stress (GPa) $\pm 6\%$
1Tdol	10 Cu	521	2.90	3.18
2Tdol	10 Cu	703	4.49	3.90
3Tdol	10 Cu	835	5.68	4.49
4Tdol	6 W	814	6.86	4.48
5Tdol	10 Cu	265	1.01	2.12

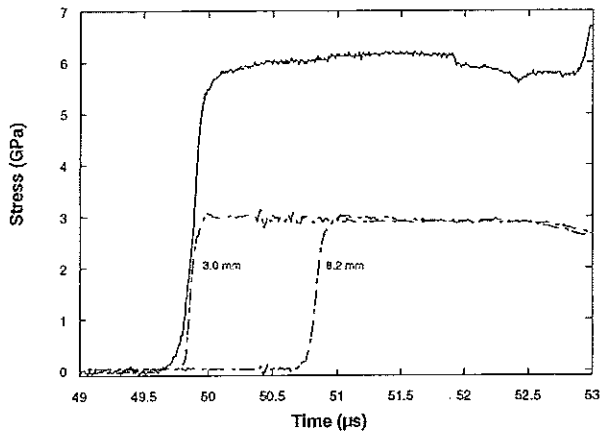


**Figure 6:** Stress wave profiles for Experiments 1Hdol/1Tdol

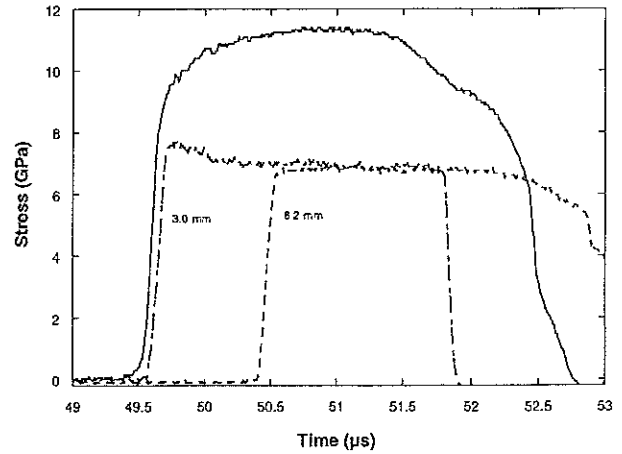


**Figure 7:** Stress wave profiles for experiments 4Hdol/4Tdol

In addition, the Dolerite data have been compared to the elastic impedance of the material using the relationship  $\sigma_x = \rho_0 U_p C_L$ , where  $\rho_0$  is the initial density of the material,  $U_p$  is the particle velocity and  $C_L$  is the longitudinal wave speed. The agreement with this fit is excellent suggesting elastic loading. Although no Hugoniot Elastic Limit (HEL) data are available for Dolerite, HELs for other igneous geological materials have been reported; basalt [13] has an HEL in the vicinity of

5 GPa, while for jadeite the HEL [14] is in the range 5.8-7.2 GPa. It is possible that the elastic impedance and the shock impedance immediately above the HEL are similar and thus make it difficult to resolve a change in slope, at the HEL, in the gauge trace.

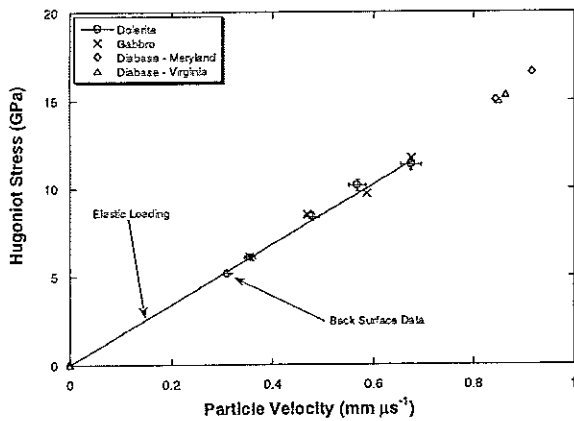


**Figure 8:** Hugoniot of Dolerite and various geologic materials

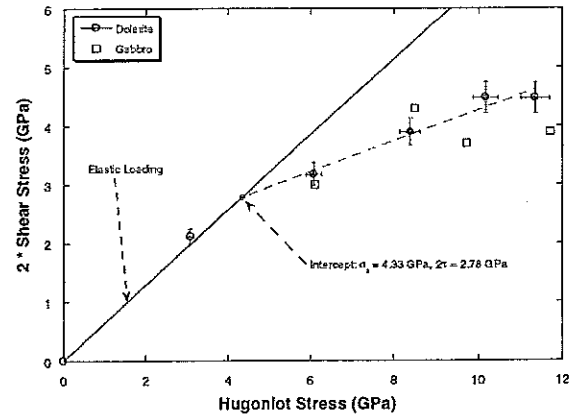


**Figure 9:** Dolerite and Gabbro shear stress

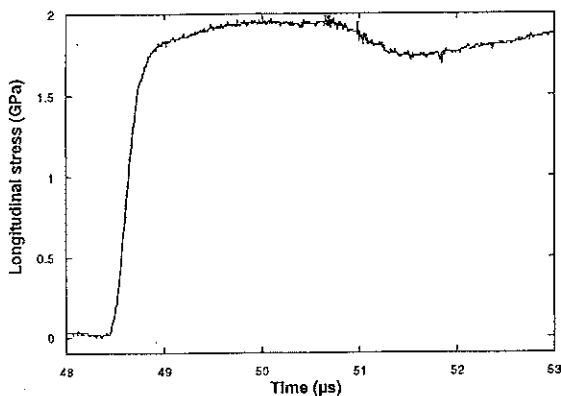


**Figure 10:** Stress wave profile for experiment 1Bdol

Figure 9 illustrates the Dolerite and Gabbro [11] shear stress vs. longitudinal (Hugoniot) stress. The Dolerite data have been fitted to equation (2b). It can be seen that above a Hugoniot stress of *ca.* 4.3 GPa the material behaviour deviated from the purely elastic loading suggesting a process such as fracture or damage in the shock front, which results in a reduction of the dynamic strength of Dolerite. Note when a lateral stress measurement is taken below 4.3

GPa, experiment 5Tdol, assuming elastic  $\sigma_x$ , the shear stress lies on the elastic loading line. This result suggests a stress of 4.3 GPa as a possible HEL value. For this reason, a longitudinal shot was performed where the Dolerite was backed by PMMA. Because of similar impedance of the gauge package and the PMMA the gauge rise time was *ca.* 30ns, compared to 200 ns for a fully embedded gauge. The measured stress in the PMMA ( $\sigma_p$ ) was converted to stress in the Dolerite ( $\sigma_D$ ) through the relation

$$\sigma_D = \frac{Z_D + Z_P}{2Z_P} \sigma_P, \quad (3)$$

where  $Z_D$  and  $Z_P$  are the elastic and shock impedances of the Dolerite and PMMA, respectively. The trace is illustrated in Figure 10. The stress induced in the Dolerite was 5.11 GPa, slightly higher than the presumed HEL. However, no two-wave structure was seen, supporting the view that the elastic and shock impedances are similar. Experiments with VISAR are under way to resolve this issue.

## 6. CONCLUSIONS

Plate impact experiments have been presented to assess the longitudinal and deviatoric behaviour of cement paste and Dolerite. Results indicate that Hugoniot curves of cement paste and concrete are comparable suggesting a weak dependence on aggregate inclusion. In addition, above the HEL the cement paste behaves inelastically indicating a process such as fracture or pore collapse reducing the strength. At the same time, the shear stress increases with increasing pressure.

In the case of Dolerite, results indicate that the Hugoniot curve is elastic up to 11 GPa. However, shear stress data show a deviation from elastic loading at a stress of 4.3 GPa. It can thus be concluded that the HEL is around that value and the gauges were unable to resolve the two-wave structure because of similar elastic and shock impedances.

## 7. ACKNOWLEDGEMENTS

The Defence and Evaluation Agency, UK has sponsored this work, under contract WSS/U3257. Dr. A. Pullen from Imperial College provided the cement samples. Dr J. Sheridan, C. O'Carroll, Dr. I.G. Cullis and P.D. Church are thanked for their interest. Finally, we thank D.L.A. Cross and R. Flaxman for technical support.

## 8. REFERENCES

1. Grady, D. E., "Impact Compression Properties of Concrete", in *Proceedings of the Sixth International Symposium on Interaction of Nonnuclear Munitions with Structures, Panama City Beach, Florida*, pp. 172-175, May 3-7 (1993).

2. Hall, C. A., Chhabildas, L. C., and Reinhart, W. D., "Shock Hugoniot and Release States in Concrete Mixtures with Different Aggregate Sizes from 3 to 23 GPa," in *Shock Compression in Condensed Matter-1997*, edited by S. C. Schmidt et al., AIP Conference Proceedings 429, New York, 1998, pp. 119-122.
3. Grady, D. E., "Shock Equation of State Properties of Concrete," in *Structures under Shock and Impact IV*, edited by N. Jones et al., Computational Mechanics Publications, Southampton, 1996, pp. 405-414.
4. Kipp, M. E., Chhabildas, L. C., and Reinhart, W. D., "Elastic Shock Response and Spall Strength of Concrete," in *Shock Compression in Condensed Matter-1997*, edited by S. C. Schmidt et al., AIP Conference Proceedings 429, New York, 1998, pp. 557-560.
5. Encyclopaedia Britannica, Inc, 2000.
6. Millett, J.C.F., Tsembelis, K. and Bourne, N.K., *Journal Appl. Phys.*, **87**, 3678 (2000).
7. Bourne, N. K., Rosenberg, Z., Johnson, D. J., Field, J. E., Timbs, A. E., and Flaxman, R. P., *Meas. Sci. Technol.* **6**, 1462 (1995).
8. Z. Rosenberg, and Y. Partom., *J. Appl. Phys.*, **58**, 3072 (1985).
9. Radford, D.D., Proud, W.G. and Field, J.E., to appear in: *Proc. Of SHOCK 2001 – APS 12<sup>th</sup> Topical Conference on Shock Compression of Condensed Matter*, Atlanta, 24-29 June 2001, (in press).
10. Millett, J.C.F., Tsembelis, K., Bourne, N.K., and Field, J.E., *Shock Compression of Condensed Matter-1999*, (eds. M.D. Furnish, L.C. Chhabildas and R.S. Hixson), 1247.
11. Millett, J.C.F., Tsembelis, K. and Bourne, N.K., *Journal Appl. Phys.*, **87**, 3678 (2000).
12. March, S.P., *LASL Shock Hugoniot Data* (University of California Press, LA, 1980).
13. Nakasawa, N., Watanabe, S., Kato, M., Iijima, Y., Kobayashi, T. and Sekine, T., *Planet. Space. Sci.*, **45**, 1489 (1997).
14. Takasawa, E., Sekine, T., Kobayashi, T. and Zhu, Y., *J. Geophys. Res. B*, **103**, 12261 (1998).
15. O. Le Vu, Ph.D. thesis "*Etude et modelisation du comportement du beton sous sollicitations de grande amplitude - Application au probleme de la penetration dynamique*", Ecole Polytechnique.

**Discrete element method for predicting the behavior of  
concrete under dynamic loading**

**C. Mariotti, Y. Grillon, F. Camborde,**

Commissariat à l'Energie Atomique, DIF/DASE/LDG, BP 12, 91680 Bruyères-le-Châtel, France,  
mariotti@dase.bruyeres.cea.fr

### Résumé

La modélisation des déformations à grande vitesse est abordée par la méthode des éléments discrets. Cette méthode est bien adaptée aux problèmes mettant en jeu la fracturation et la fragmentation de matériaux hétérogènes ou des géomatériaux. Le maillage est de type Voronoï, le diagramme de Delaunay associé représente l'ensemble des contacts reliant deux cellules voisines. Chacun des liens est caractérisé par des paramètres locaux de raideur normal  $K^n$  et de cisaillement  $K^s$ . De plus, on introduit deux limites de rupture  $\phi^n$  et  $\phi^s$  pour simuler les ruptures en mode-I et en mode-II. Un code numérique construit à partir de cette méthode est utilisé pour modéliser les effets d'une explosion au contact d'une plaque de béton de 20 cm d'épaisseur. Les résultats des simulations sont comparés aux mesures expérimentales. Les phénomènes de compactions, de propagation de fracture et d'endommagement sont bien rendus. On montre que la phénoménologie est complexe et dépend du taux de contrainte et de la porosité du matériau.

### Abstract

High strain rate tests are simulated by a 2D discrete element method. This method is well adapted to problems involving fracturing and fragmentation of heterogeneous materials and geomaterials. The mesh is a Voronoï diagram, the associated Delaunay diagram being the set of the links between each cell and its neighbors. Each link is characterized by local parameters  $K^n$  and  $K^s$ , the normal and the shear stiffness. Furthermore, rupture thresholds  $\phi^n$  and  $\phi^s$  are introduced to simulate mode-I and mode-II crack. A numerical code based on this method is used to simulate the effects of contact explosion on a 20 cm width concrete slab. Synthetic results are compared with experimental data. Compaction, fracture propagation and damage are well-fitted. It is shown that the phenomenology is complex and depends on strain rate loading and porosity of target materials.

**Abstract.** High strain rate tests are simulated by a 2D discrete element method. This method is well adapted to problems involving fracturing and fragmentation of heterogeneous materials and geomaterials. The mesh is a Voronoï diagram, the associates Delaunay diagram being the set of the links between each cell and its neighbors. Each link is characterized by local parameters  $K^n$  and  $K^s$ , the normal and the shear stiffness. Furthermore, rupture thresholds  $\phi^n$  and  $\phi^s$  are introduced to simulate mode-I and mode-II crack. A numerical code based on this method is used to simulate the effects of contact explosion on a 20 cm width concrete slab. Synthetic results are compared with experimental data. Compaction, fracture propagation and damage are well-fitted. It is shown that the phenomenology is complex and depends on strain rate loading and porosity of target materials.

## 1. INTRODUCTION

Understanding the response of aggregate material when subjected to high strain rate is a key point to describe the behavior of structure involved in situations such as impact loading or explosion. Discrete element methods are based on a discretisation of a structure by finite units which are locally driven by mechanical interactions with their neighbors. The discrete element method used in this study approximates these elemental units as rigid particles. Since the problem of studying high strain rate events implies strong inertial effects, Newton's law of motion is used to obtain velocity and displacement of each element. The specificity and the originality of a discrete element method relies mainly on its *description of the medium* (part 2.1) and its *interaction law* (part 2.2) which connects particles.

Previous works were conducted on this subject: Potyondi and Cundall<sup>[2]</sup> had shown the advantage of discrete element method compared to finite element methods regarding the post-failure behavior of material. In the present work, we add the notion of potential shear plan which will be developed in part 2.1. This idea is quite similar to the multiplane model developed by Curran et al<sup>[3]</sup>.

In this study, we use a numerical model SDEC (Spherical Discrete Element Code) developed by F. Donzé<sup>[1]</sup>, based on Discrete Element Method (DEM) to investigate the importance of stress waves in generating fractures and damages. DEM is well-adapted to problems involving cracks and fractures: the medium is described by an assembly of particles, each one is linked to its neighborhood by an interaction, generating a mesh. Interaction between two elements has to be defined to describe the mechanical properties of the medium. Furthermore, characteristics of a link could be modified or changed to provide for example local weakness. The numerical model is basically 3D with spherical rigid elements. Nevertheless, in the present paper, the model is used with an option providing polygonal elements (Voronoi) in a 2D axisymmetric configuration.

This paper focuses on a set of experiments conducted with a MB50 concrete slab submitted to a central explosive blast.

## 2. NUMERICAL ANALYSES

### 2.1 Description of the medium

The method developed in the present work consists of creating Voronoï polygons or cells associated with a lattice bond (Delaunay tessellation) shown in Fig. 1. Four steps are necessary to provide all the mesh:

1. The whole structure is filled by a set of points equally distributed onto a regular triangular mesh.
2. Each point is randomly displaced from its initial position.
3. A Voronoï cell is created from each point with its nearest neighbors (from 5 to 7 neighbors)
4. This last step is to determine and to build each interaction between two contiguous cells.

Finally, the constructed mesh has no residual geometric porosity and allows mapping of complex structure.

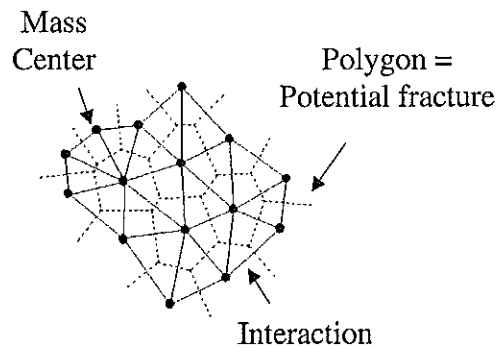


Fig 1: Typical Voronoï mesh, the red color is for interaction links and blue color for polygonal particles. It is assumed that the mass of a particle is reported to its center.

### 2.2 Interaction law

Each element represents a mesoscale aspect of the medium. The elementary cell for concrete is a mix of cement grains and voids. Initially, each interaction link is able to transmit tensile, compressive and shear forces. Figure 2 shows the decomposition of the force  $F$  between two cells. A normal  $F_n$  and a tangential  $F_s$  components are respectively associated with an elastic normal and shear spring ( $K_n$  and  $K_s$  stiffness). The numerical model supposes that stiffness' are constant and independent of the relative movement of the linked elements, as long as the behavior of the medium is elastic. These two parameters are evaluated following Kusano's relation<sup>[4]</sup> (1a-b):

$$K_n = \frac{1}{\sqrt{3}} \frac{E}{(1+\nu)(1-2\nu)} \quad (1.a)$$

$$K_s = \frac{1}{\sqrt{3}} \frac{E(1-4\nu)}{(1+\nu)(1-2\nu)} \quad (1.b)$$

where  $E$  and  $\nu$  are respectively the Young's modulus and the Poisson's ratio of the medium. These two relations are strictly valid in 2D for a thickness unity and have to be adapted to axisymmetric geometry. The normal and tangential forces are calculated following a time centered scheme (2a-b):

$$F_n(t + \Delta t) = F_n(t) + K_n (\Delta U_x + \Delta U_y) \quad (2.a)$$

$$F_s(t + \Delta t) = F_s(t) + K_s \Delta \gamma \quad (2.b)$$

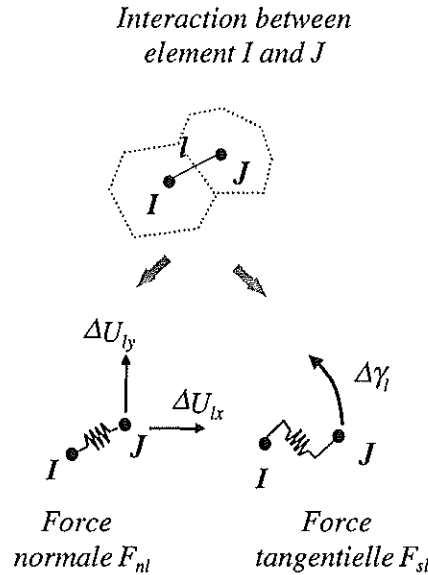


*Fig 2: Particles interactions are splitted to normal and tangent elastic forces.  
 $\Delta U$  and  $\Delta \gamma$  are respectively normal and tangential displacements*

The stress tensor  $\sigma_{ij}$  must be calculated from an average of the forces on a homogenization surface (or volume for 3D problems) which contains about 30 polygonal cells, following equation (3).

$$\sigma_{ij} = \frac{1}{2A} \sum_{k=1}^n F_i^k l_j^k \quad (3)$$

where  $A$ ,  $l_j$ ,  $F_i$  and  $n$  are respectively the surface of homogenization, the intercentroïdal distance projected on  $j$ -axe, the interaction force projected to  $i$ -axe and the number of interactions into the surface  $A$ . It is generally assumed that the surface is a square.

The constitutive model is separated in a linear elastic model for the uncracked material and a softening model for the cracked material. Drucker-Prager failure criterion, generally adopted for concrete and geomaterials, is locally defined by a Mohr-Coulomb threshold. Mode-I (traction damaging) and Mode-II (compression damaging) are separately modeled by a tensile threshold and a shear threshold.

Uniaxial and triaxial experiments conducted by Buzaud<sup>[5]</sup> in 1998 provide macroscopic parameters of MB50 (Tab. 1). Previous analysis and modeling of these experiment by SDEC have been performed by Brara et al<sup>[6]</sup> and have given a set of parameters  $C$ ,  $\phi$  and  $T$  well adapted to describe the behavior of MB50. Le Vu experiments<sup>[7]</sup> in 1997 provide the parameters of the constitutive equation of MB50 (Tab 2).

Density	2800 kg.m <sup>-3</sup>
Young's modulus	35 Gpa
Poisson's ration	0.2
Compressive strength	70 Mpa
Strain failure	0.3 %
Tensile compressive strength ratio	10

Table 1: Macroscopic parameters of MB50 concrete

### 3. EXPLOSIVE LOADING OF MB50 CONCRETE

#### 3.1 Experimental setup

The aim of the present experiment is to characterize the behavior of a concrete slab loaded by a near field detonation wave. These experiments were conducted at Centre d'Etude de Gramat in the experimental GEO campaign<sup>[8]</sup>. Figure 3 shows the tested structure with the priming device. Concrete slab is a 1-meter diameter and 20-cm width cylinder. Six slabs have been built, three with 32-mm diameter explosive charge and the other ones with a 45-mm diameter charge. For each group, two slabs were instrumented with strain gages and the third was unmodified. Three gages were placed in the instrumented slabs at 50, 100 and 150 mm deep with regard to the front face. A laser velocimeter was installed behind the slab to measure the rear face velocity.

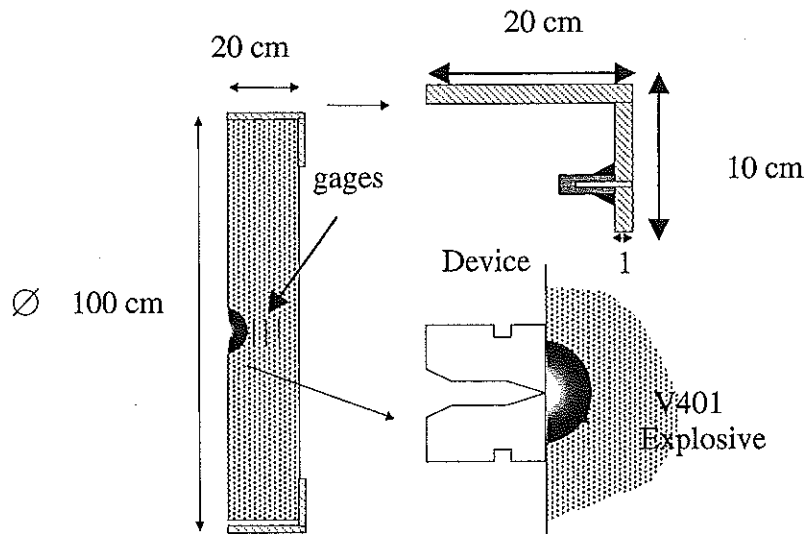


Fig 3: MB50 Concrete slab with the explosive device (V401 explosive).

After the detonation of V401 explosive, the direct hemispheric shock wave (and the rarefaction wave following) and the induced damaging such as cratering on front face or flaking on rear face. All the experiments have caused a rear flake of about 450 mm diameter with a 10 ms<sup>-1</sup> and a 2.6 ms<sup>-1</sup> ballistic velocity respectively for 45 mm and 32 mm diameter charge. The generated crater at the front face had a diameter 2.5 times larger than the explosive charge.

### 3.2 Numerical setup

The simulation was carried out with 37000 cells. A JWL (John-Wilkens-Lee) equation of state of the V401 explosive was used to provide the loading rate of the concrete within a finite difference numerical code. The form of the JWL equation is shown in equation (4). The loading peak pressure is about 20 GPa beside the symmetry axe.

$$P = A\left(1 - \frac{\omega\rho}{R_1\rho_0}\right)\exp\left(-R_1\frac{\rho_0}{\rho}\right) + B\left(1 - \frac{\omega\rho}{R_2\rho_0}\right)\exp\left(-R_2\frac{\rho_0}{\rho}\right) + \frac{\omega\rho^2}{\rho_0}Em_0 \quad (4)$$

### 3.3 Results

Figures 4a and 4b show a comparison of the calculated and the measured pressure. The results are excellent with regard to time arrival of the peak of the compressive wave and the pressure level. The loading slopes for the 45mm diameter charge are  $35 \cdot 10^4 \text{ GPas}^{-1}$  for gage #1,  $2 \cdot 10^4 \text{ GPas}^{-1}$  for gage #2 and  $0.8 \cdot 10^4 \text{ GPas}^{-1}$  for gage #3. The compressive strength is supposed unmodified in the vicinity of sensor #2 and #3, so we are able to provide the strain rate at these locations:  $500 \text{ s}^{-1}$  and  $200 \text{ s}^{-1}$  for gages #2 and #3 respectively. We note a rapid decrease of this strain rate due to the effect of porosity in MB50. Figure 5 shows global pressure snapshots at time  $22 \mu\text{s}$ ,  $72 \mu\text{s}$  and  $110 \mu\text{s}$  for the 45mm diameter. We remark at earlier time a sharp hemispherical shock wave (yellow color) which is spread during propagation of the wave. Behind the compressive wave is a rarefaction wave due to the spherical divergence of the propagation. The shock wave interaction with the rear face of the slab generates a strong depletion wave, which returns to the front face of the slab (dark blue color).

Quantitative damaging of the medium is given by the ratio of the numbers of broken links and initial links for each element. Figure 6 shows total damaging of the specimens at time  $110 \mu\text{s}$ . Following Kutter<sup>[9]</sup>, three domains can be characterized by their damaging rate: the first one is in the vicinity of the explosive charge, where concrete is totally plastified (100%). The second domain is characterized by a diffuse damaging (~50%) and a non-vanishing cohesion. The third domain has kept its elastic properties yet but contains local failures. Numerical simulations allow the distinction between Mode-I and Mode-II cracks. We show that Mode-II cracks have a limited extension to the neighborhood of the explosive charge and are induced by uniaxial deformation. Far field localized cracks are mainly produced by Mode-I mechanism.

Fragmentation is shown in figure 7. The reflection of the direct shock wave at the rear face of the specimen generates a depletion wave, which is reflected to the front face. Mode-I cracks appear and cause flaking. We note that in ours experiments the presence of the third gage weakens the specimen. This phenomenon has been simulated, and we have got the radial extension of the main flake: 410 mm and 380 mm for the 45 mm and 32 mm explosive charge respectively. The velocity of the flakes has been measured by the velocimeter. We note in Table 2 that the synthetic results are in good agreement with the experiments.

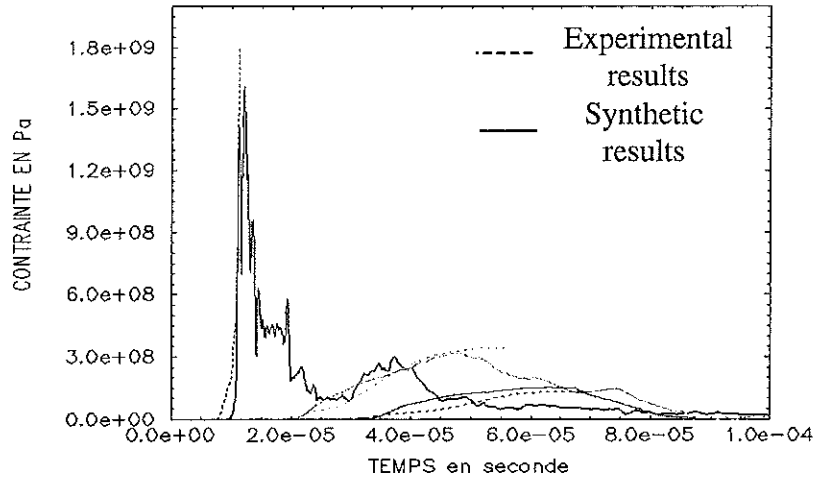


Fig 4a: Comparison of experimental and simulated pressures in a MB50 slab loaded by a 45 mm diameter charge (V401 explosive).

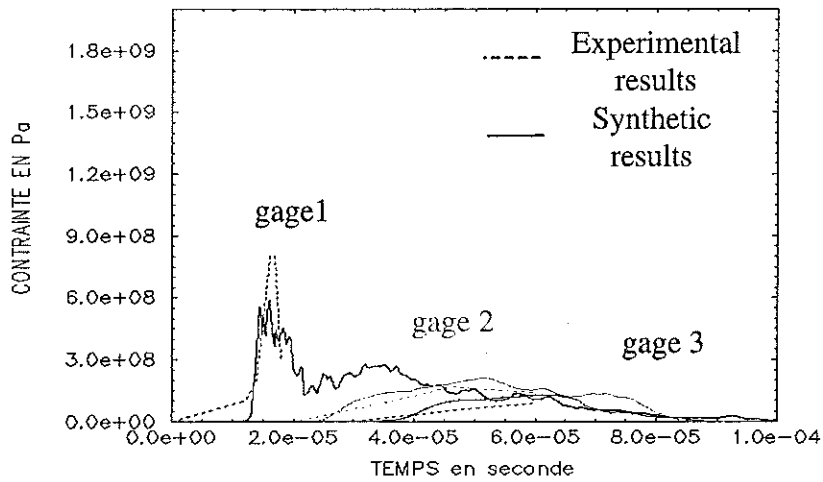


Fig 4b: Comparison of experimental and simulated pressures in a MB50 slab loaded by a 32 mm diameter charge (V401 explosive).

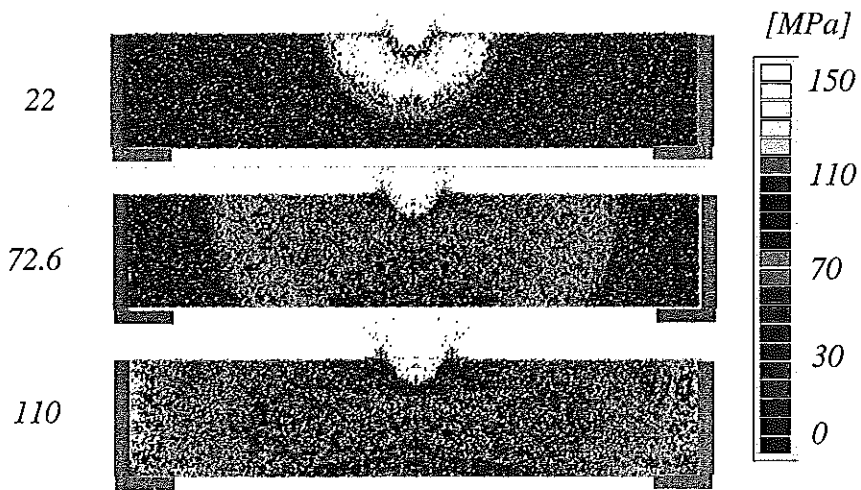


Fig 5: Pressure snapshot into the MB50 concrete slab loaded by a 45 mm explosive charge. Time t=22, 72 and 110 μs.

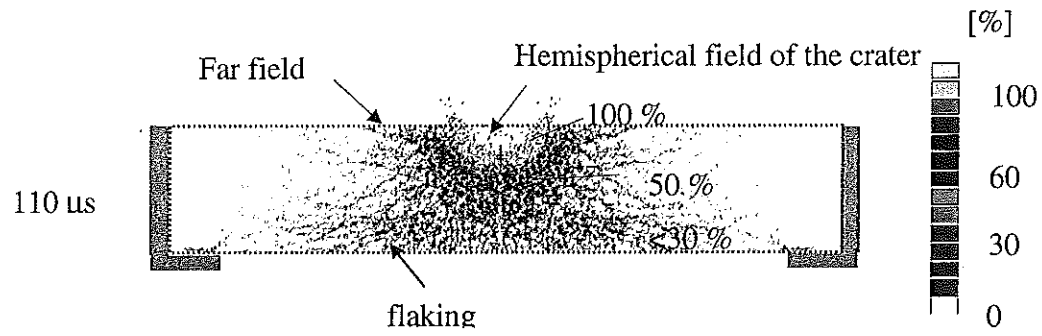


Fig 6: Total damaging (Mode-I and Mode-II) of the MB50 concrete slab loaded by a 45 mm explosive charge. Time  $t = 110 \mu\text{s}$ .

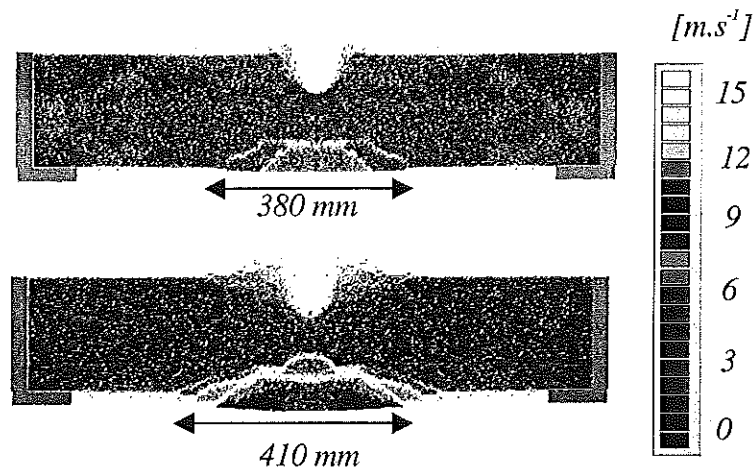


Fig 7: Vertical velocity snapshot into the MB50 concrete slab loaded by a 32 mm (top) and a 45 mm (bottom) explosive charge. Time  $t = 110 \mu\text{s}$ .

	$D_{32 \text{ mm}}$		$D_{45 \text{ mm}}$	
	<i>Expérimental</i>	<i>Synthetic</i>	<i>Expérimental</i>	<i>Synthetic</i>
<i>Hemispherical crater diameter</i>	80 mm	65 mm	112 mm	100 mm
<i>Total Crater diameter</i>	192 mm	-	270 mm	290 mm
<i>Rear flake diameter (unmodified slab)</i>	No flaking	-	420 mm	-
<i>Rear flake diameter (instrumented slab)</i>	450 mm	380 mm	450 mm	410 mm
<i>Rear flake velocity</i>	$2.6 \text{ ms}^{-1}$	$4 \text{ ms}^{-1}$	$\sim 10 \text{ ms}^{-1}$	$10 \text{ ms}^{-1}$

Table 2: comparison of the macroscopic damages

#### 4. CONCLUSION

In the case where very large deformation exist, fragmentation occurs, and the classical description of the medium becomes insufficient. Discrete Element Method (DEM) and its associated interaction laws are well suited to treat such problems. These experiments have shown high strain rate of about  $500 \text{ s}^{-1}$  and a complex behavior of the concrete slab: high compressive followed by tensile stresses, crushing, plastic failure and fragmentation, flaking and craterization. As regards of these phenomena, DEM has given encouraging results, and allows us to plan a direct 3D simulation of such high strain rate loading.

#### References

- [1] **Donzé F.V., Magnier S.A.**, Numerical simulation of impacts using a discrete element method, *Mech. Cohes.-frict. Mater.*, vol. 3, pp.257-276, 1998
- [2] **Poyondi D.O., Cundall P.A., Lee C.A.**, Modelling rock using bonded assemblies of circular particles, *Rock Mech.* pp. 1937-1944, 1996.
- [3] **Curran D.R., Seaman L., Cooper T., Shockey D.A.**, Micromechanical model for comminution and granular flow of brittle material under high strain rate. Application to penetration of ceramic targets, *Int. J. of Impact Eng.*, vol. 13, n°1, pp.53-83, 1993
- [4] **Kusano N., Aoyagi T., Aizawa J., Ueno, Morikawa H., Kobayashi N.** Impulsive local damage analysis of concrete structure by the distinct element method, *Nuclear Engineering and Design*, vol. 138, pp 105-110, 1992)
- [5] **Buzaud E.**, Performance mécanique et balistiques du microbéton MB50, *Contrat n°97.25.022.00470.46.51*, 1998
- [6] **A.Brara, F.Camborde, J. Klepaczko, C.Mariotti**, Experimental and numerical study of concrete at high strain rates in tension, *Mechanics of Materials*, n° 33,pp. 33-45, 2001
- [7] **Le Vu O.**, Etude et modélisation du comportement du béton sous sollicitations de grande amplitude, Thèse de l'Ecole Polytechnique, 1995
- [8] **Rouquand A., Grouffal J.Y.**, Présentation et résultats des essais en dynamique rapide sur dalle en béton, *Communication au GEO'99*, Aussois, février 1999
- [9] **Kutter H.K., Fairhurst C.**, On the fracture process in blasting, *Int. J. Rock. Mech. Min. Sci.*, vol. 8, pp 181-202, 1971

# DYNAMIC FAILURE OF GLASSES

D.D. Radford, G.R. Willmott, W.G. Proud and J.E. Field

*PCS, Cavendish Laboratory, Madingley Road, Cambridge, CB3 0HE, UK.*

**ABSTRACT** There has been considerable interest in the dynamic failure of silica-based glasses since the first observation of the so-called "failure wave" by Kanel and co-workers in 1991 [72, 85]. As a result, evidence obtained from a number of experimental techniques is now available. Three main theories have recently been proposed that attempt to describe the mechanism of failure in glasses. The experimental results showing the existence of failure waves, or propagating damage fronts are summarized and the three theories are reviewed. Recent results from symmetric Taylor and plate impact tests are presented that provide further insight into the process of failure in glasses.

## INTRODUCTION

Over the past 40 years, there have been a large number of investigations into the deformation behaviour of silica-based glasses under shock loading conditions [1-94]. As a result, the properties of a number of glass materials including borosilicate [4, 7, 55, 78-81], soda-lime [2, 13, 18, 19, 31, 35-37, 61, 62, 64-66, 81-87] and "filled" glasses [21, 50, 59, 61] are reasonably well defined.

Previous work at the Cavendish Laboratory on the properties of glasses under shock loading has demonstrated that the material response is highly dependent upon the composition of the glass [19, 40]. The shock response of glass materials with an open structure, such as borosilicate, exhibits a ramping behaviour in the longitudinal stress due to structural collapse. Glasses with a filled microstructure, as in the case of Type-D, *Extra Dense Flint* (DEDF) do not exhibit a ramping behaviour and behave in a manner similar to polycrystalline ceramics [21]. Partially filled materials, such as soda-lime glass, show an intermediate response. Although the shock response of these glasses varies considerably, one common feature to all is the existence of a damage front that propagates behind the initial shock over a certain range of stresses [21, 57, 60, 61, 65].

It is generally accepted that Kanel and co-workers [72, 85] in 1991 were the first to present conclusive evidence of the existence of a propagating damage front, denoted as a "failure wave", in K-19 (similar to soda-lime)

glass. Shortly thereafter, Brar and co-workers demonstrated that the shear strength undergoes significant reduction and the spall strength is essentially reduced to zero across the damage interface [69, 86]. Since then, numerous experimental studies have focused on the failure process in glasses [14, 22, 45, 47, 57, 59, 62, 66, 71, 74, 85, 87-90].

Three main theories on the mechanism of failure in glasses have been suggested by Clifton [91], Grady [92], and Espinosa and co-workers [93, 94]. Clifton's theory is based on the assumption that the failure front is a propagating phase boundary. The mechanism for failure is the nucleation of shear cracking due to the densification caused by the initial shock. Grady's theory is applicable to the failure of brittle materials in general, and is based on the transfer of elastic shear strain energy to dilatant strain energy. Espinosa proposed that failure front formation is due to a unique inelastic behaviour in silica-based glasses containing modifier ions.

In this investigation, a brief overview of the current understanding of dynamic failure in glasses is presented and the theories attempting to describe the failure process are discussed in terms of existing experimental evidence. In addition, recent results from plate and Taylor impact experiments are described that provide further insight into the kinetics of failure.

## BACKGROUND

### The Existence of Failure Waves

The experimental evidence provided by Kanel and co-workers [1, 2] consisted of small reload signals on the free-surface velocity histories of K-19 specimens measured using VISAR. The small recompression signals observed were thought to be due to the failed material having a lower mechanical impedance, as compared to the “intact” material. Similar results were subsequently obtained for experiments performed on soda-lime glass [14, 37].

In experiments designed to measure the spall strength in the region ahead of and behind the failure front using manganin gauges, Brar et al. [69-71] demonstrated that the spall strength is essentially reduced to zero in soda-lime glass shocked in the range of 4 to 7 GPa. Similar results were obtained in aluminosilicate glass by Raiser et al. [87] using VISAR.

The lateral stress behaviour of a material can be measured by embedding a manganin stress gauge in the transverse orientation [95-101]. The so-called lateral gauge experiment has been used extensively in silica-based glasses [18, 20, 21, 57, 60-62, 66-69, 72, 85, 86]. In this configuration, the lateral stress increases upon the arrival of the failure front at the gauge location. Using the measurements ahead of, and behind the failure front, the shear stress ( $\tau$ ) defined by,

$$2\tau = \sigma_x - \sigma_y \quad (1)$$

can be calculated, where  $\sigma_x$  and  $\sigma_y$  are the longitudinal and lateral stress, respectively.

Previous work performed at the Cavendish Laboratory demonstrated that failure fronts occur in soda-lime, borosilicate and DEDF glasses, and the shear strengths lie on the same non-failed and failed curves when plotted against longitudinal stress [40]. It was speculated that the silica-based network common to the glasses was responsible for the similarity in deviatoric response. Further work on three filled glasses over a larger pressure range subsequently showed a consistent dependence on impact pressure [59], shown in figure 1. The shear stress ahead of the failed

material is seen to increase linearly along the estimated elastic response. Behind the front, however, the shear stress first decreases and then increases as the impact stress increases.

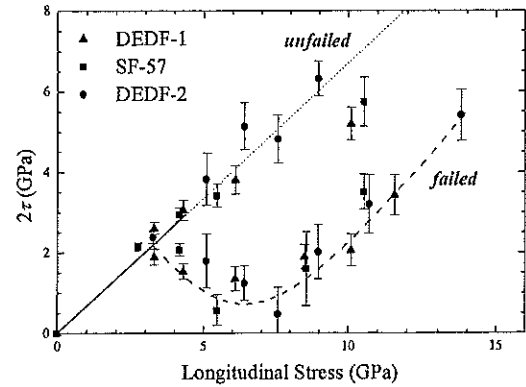


FIGURE 1: Deviatoric responses of dense glasses tested up to ca. 14 GPa longitudinal stress [57].

This observation modifies the previous interpretation based on longitudinal stress data to ca. 8.5 GPa, which suggested that the shear stress behind the failed material remains constant. A plausible explanation is that the comminuted material behind the failure front consists of fragments that will impart force/resistance as they attempt to move past one another under a shear force. As the pressure is increased, more force is required to move the fragments, due simply to mechanical constraint.

Using high-speed photography, failure fronts have been visualized in borosilicate and soda-lime glasses during plate [66] and Taylor impact tests [102] at the Cavendish Laboratory, and in borosilicate rods during Taylor tests by Brar and co-workers [70, 103]. In the plate impact experiments, an advancing dark zone termed the failure wave follows the initial shock. When lateral gauges were embedded in the target, the arrival of the dark zone at the gauge location corresponded to the second step in the measured stress history. In the Taylor impact tests, failure fronts were observed to propagate along the length of the bar and the structure of the radially expanding (failed) material was dependent upon the type of glass. Also, the velocity of the failure front increased as the impact pressure increased.

A comprehensive study on the failure of glasses, ranging from the fully open structured fused-quartz to the fully filled DEDF, is currently ongoing at the Cavendish Laboratory. Further evidence of failure fronts has been observed in two new filled glasses during plate impact experiments. Also, the impact pressure dependence of failure front velocity during symmetric Taylor impact tests has been characterised for five glasses. Some of these results are presented below.

### **The Mechanism of Failure**

In 1993, Clifton [91] proposed that a propagating boundary moves through a shocked glass at a constant velocity causing the silica in the glass to undergo a phase transformation. The transformation will be to another amorphous state or crystalline phase and will induce large strains and microcracking within the material. This manifests itself in the complete loss of spall strength, characteristic of experimental observations related to failure fronts. However, a phase transformation must be accompanied by a discontinuity in either volume or density, which would lead to a corresponding change in the longitudinal stress. To date, no discontinuity in longitudinal stress, measured by gauges or VISAR, has been observed.

Grady's approach [92] does not explain the incubation and nucleation of fracture, but seeks to explain two phenomena observed in failure front experiments. Firstly, particle velocity does not change significantly as the failure front passes implying that the change in volume at the failure front interface is negligible. Secondly, the axial stress does not alter significantly until it slowly attenuates after the failure front has passed. Grady found that these two requirements could be satisfied if the volumetric compressibility of the material changes as the failure front passes. Moreover, the dilatant strain caused by fracture under these conditions is consistent with the transfer of elastic shear strain energy in the shocked glass to dilatant strain energy in the failed glass. The mechanism for this

energy transfer is microcracking, resulting in failure front formation.

Using this approach, Grady has proposed a characteristic curve for axial strain as a failure wave passes. That is, a sharp rise to the Hugoniot Elastic Limit (HEL) of the material upon the arrival of the elastic shock wave followed by a shallow 'ramp' as the failure front passes, and eventually a large rise as the material is deformed and radial expansion occurs. Such a curve can be compared to gauge traces to confirm the passage of a failure front.

The theory proposed by Espinosa and co-workers [93, 94] refutes crystallization as a cause of crack nucleation due to studies of confined glass bars recovered from impact experiments. Such samples retained their amorphous structure. They present an alternate mechanism, in which the characteristic microcracking of failure nucleates at shear induced flow surfaces. Such a surface is formed when the shear stress exceeds the flow stress of the glass.

Simulations incorporating this theory have been able to reproduce observed trends in axial and transverse stress histories, spall strength and radial characteristics. Also, the model can simulate damage-induced anisotropy.

An important consequence of this mechanism is that cracks propagate from flow surfaces. Therefore, it is to be expected that the behaviour of failure, as it propagates from these surfaces, will be determined by shear crack mechanics.

### **EXPERIMENTAL PROCEDURES**

In this investigation, results from plate impact experiments on a filled glass (DEDF) and symmetric Taylor impact tests on soda-lime and fused-quartz are presented. The properties of the DEDF glass are provided in ref. [57], denoted there as DEDF-1. The properties of the soda-lime glass are provided in ref. [102]. Two single-stage light gas guns (20 and 50 mm) at the Cavendish Laboratory were used in this investigation. In the plate impact

experiments, longitudinal stress measurements were taken by embedding piezoresistive manganin gauges (Micromeritics type LM-SS-210FD-050) between tiles of the target materials. Impact velocities were measured by the shorting of sequential pairs of pins to an accuracy of  $\pm 0.5\%$ , and the specimen alignment was fixed to be less than 1 mrad by of an adjustable specimen mount. High-speed photographic sequences were taken using an UltraNAC-FS501 camera.

### RESULTS AND DISCUSSION

Figure 2 shows a sequence from a symmetric Taylor test performed with 10 x 100 mm soda-lime rods at an impact velocity of 391 m/s. Each frame is labelled with the time, in microseconds, after impact has occurred. The exposure time for each of the photographs was 0.2  $\mu$ s. The projectile rod is observed, having just left the gun barrel, entering from the left and impacting the other rod. After impact, dark fronts are observed to propagate into the rods. In similar experiments performed with higher magnification, a shock wave may be observed as the initial thin dark line in the first few microseconds after impact (see figure 3). In all the experiments performed the material behind the initial dark line became opaque, indicating that the material comminuted. As the comminuted interface (failure front) propagated into the rod, material either side of the rod-rod interface starts to expand radially, as shown in figure 2. It is interesting to note that in a number of the frames the failure front appears jagged across the width of the specimen.

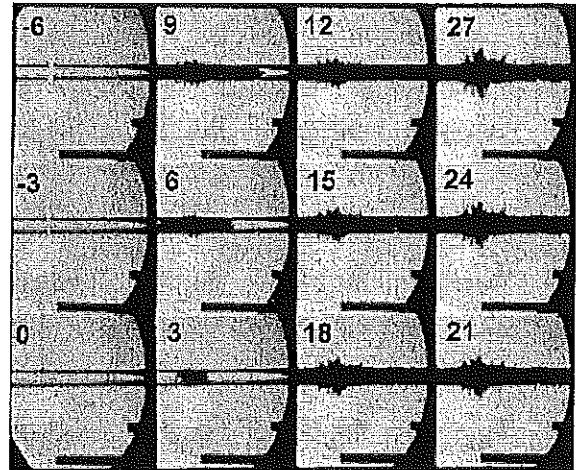


**FIGURE 2:** Photographic sequence of a symmetric Taylor impact test using 10 mm diameter soda-lime rods (impact velocity = 391 m/s).

This observation indicates that the failure front is not a continuous interface, supporting the idea that microcracking at localised flaws causes failure front advancement. As seen in a previous investigation [102], the structure of the radial expansion is material dependent. These results indicate that the composition of the material affects the micro-mechanics of failure.

Symmetric Taylor tests were also performed on fused-quartz rods that had a diameter of 25 mm. Figure 3 shows a high-speed photographic sequence for an experiment conducted where the flyer rod was travelling at 534 m/s at impact. The exposure time for each of the photographs was 0.1  $\mu$ s. The time after impact is indicated in microseconds in each frame. Again, the flyer rod was travelling from the left to the right. It should be noted that the wide vertical lines along the edges of the specimen are due to the refraction of light through the curved surface of the rod.

In the first frame (0.3  $\mu$ s after impact), two vertical dark lines are observed. The line at the left is the impact face. The line to the right is a shock wave that can be clearly seen propagating at a higher velocity in front of the other waves in subsequent frames. Another front is observed in the frames labelled 1.5  $\mu$ s and 1.8  $\mu$ s after impact, which has become the failure front by 2.1  $\mu$ s after impact. Until the release waves from the outer edges converge along the centre of the specimen, a 1-D state of

strain will exist. Therefore, figure 3 shows the development of failure under the same conditions experienced during plate impact, including a transition to a 1-D stress state. It is interesting to note that the second front visible at 1.5  $\mu\text{s}$  does not advance significantly until the material behind it becomes fully comminuted (opaque). Subsequent frames clearly show that the advancement of the radial expansion corresponds with the leading edge of the failure front.

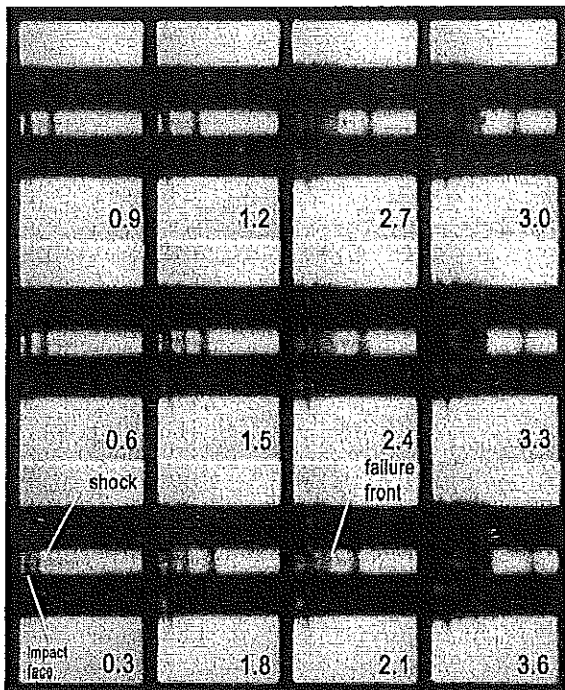


FIGURE 3: Photographic sequence of a symmetric Taylor impact test using 25 mm diameter fused-quartz rods (impact velocity is 534 m/s)

Based on measurements from the photographs, the first front is calculated to slow from a velocity approximately equal to the longitudinal wave speed in fused-quartz (5.96 mm/ $\mu\text{s}$ ) during the initial 2.1  $\mu\text{s}$  after impact, to  $5.2 \pm 0.3$  mm/ $\mu\text{s}$  after 3.9  $\mu\text{s}$ . It is believed that the incident shock appears to slow due to the transition from 1-D strain to

1-D stress as the release waves move in from the edges. As this transition occurs, the pressure difference across the shock will decrease resulting in less light being refracted. Eventually, the pressure difference is reduced to the point where the incident wave is not visible.

The velocity of failure fronts in several glasses has been extensively studied using symmetric Taylor tests. This work will be published in future articles. Overall, it was observed that the failure front velocity asymptotically approaches a value of  $\sqrt{2}c_s$  (where  $c_s$  is the shear wave speed) as the impact pressure increases. This value is consistent with current proposals for the maximum velocity of shear crack propagation based on theory and experimental evidence, as summarized by Rosakis et al.[104].

Figure 4 shows the longitudinal stress measured during a plate impact experiment conducted at 843 m/s on DEDF using a W-Alloy flyer. The gauge was embedded between DEDF plates, with the front plate being 6.1 mm thick. From the longitudinal traces it is seen that the stress initially rises

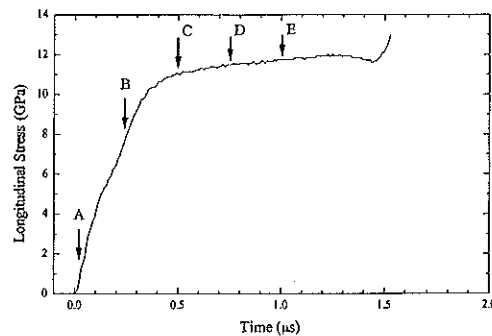
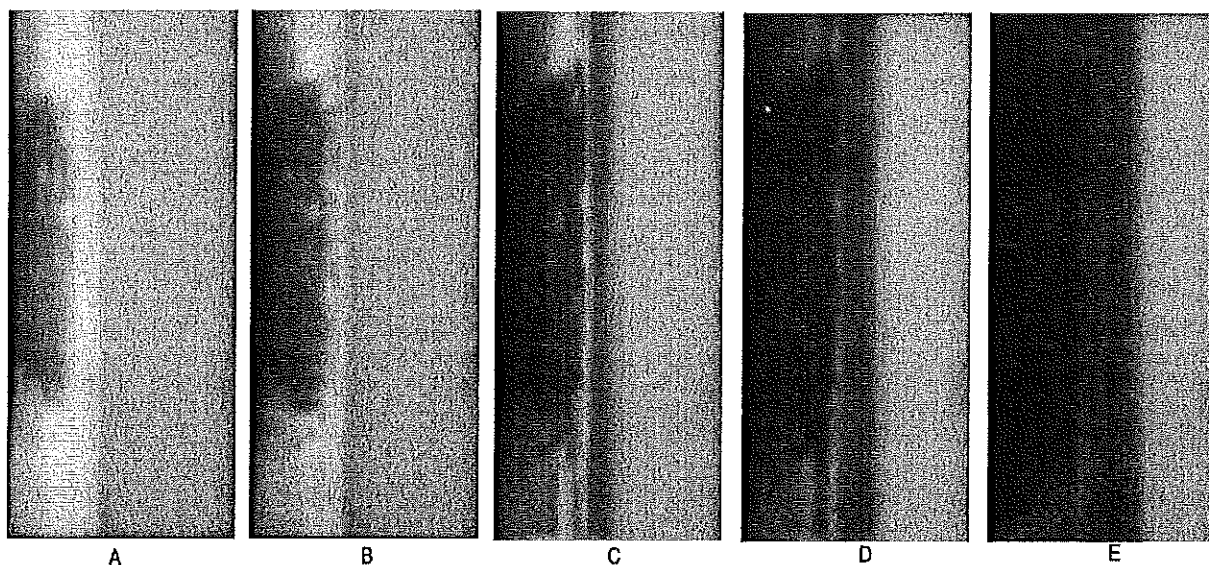


FIGURE 4: In-material longitudinal stress history experiment on DEDF using W-Alloy flyer. (impact velocity = 843 m/s).



**FIGURE 5:** Photographic sequence of a plate impact experiment on DEDF (impact velocity is 843 m/s, inter-frame time is 0.25  $\mu$ s)

quickly to a value of *ca.* 4.5 GPa, which agrees closely with the previously reported HEL of  $4.3 \pm 0.2$  GPa [68]. At this point, the slope of the stress trace decreases, indicative of inelastic deformation. The stress continues to increase until reaching an equilibrium stress of  $11.6 \pm 0.3$  GPa. It is interesting to note that this profile is very similar to that from which Grady developed his failure model [92].

Figure 5 shows a number of frames from the high-speed photographic sequence taken during this experiment. The inter-frame time for sequences was 0.25  $\mu$ s, and the flyer struck the target from the left-hand-side. The figure shows a side-view of the specimen. The entire specimen thickness is shown, and approximately 35 mm of the central vertical section.

From frame A it is seen that the leading edge of the incident shock appears light and the visibly failed material, following the shock, appears dark. This photograph appears different to previous photographs of shock loaded glass where failure was observed [66, 67]. Typically, the incident shock appeared as a dark line, not a light area, and the failed material appeared as a continuous black region usually extending a width equal to the diameter of the flyer. Frames A and B, however, show

that the incident shock appearing as a light area and that the dark zone grows initially from the centre of the target. It is believed that the impact pressure, being well above the HEL, causes near instantaneous failure of the material as the incident shock propagates into the material. As the glass fails, or fractures due to the induced shear stress, light is emitted by fracto-emission. As a result, the shock-unshocked interface is visible, the shocked material being visibly lighter. This light zone represents failed, or comminuted material. As the cracks in the comminuted material begin to separate, the light from the light source used to take the photographs is scattered causing a dark image to appear. The distance that a crack must be opened to cause scattering of light is *ca.*  $\frac{1}{2}$  the wavelength of the particular light source. Therefore, the dark zone (generally referred to as a failure front) represents material that has numerous cracks separated by at least  $\frac{1}{2}$  a wavelength. The material between the dark zone and the incident shock has also failed, but the evidence of the failure is not yet visible. It can be said then, that the failure of glass, and likely brittle materials in general, is a time dependent process rather than an instantaneous process that sweeps through the material.

The time at which each photograph was taken is indicated in figure 4, with frame A corresponding to the arrival of the incident shock at the gauge location. The inelastic portion of the stress profile corresponds to frame B. It is seen that as the highly comminuted material (dark zone) passes by the gauge location, the stress reaches equilibrium.

The remaining frames in figure 5 further demonstrate the development of failure under high pressure. The light zone, or shocked (comminuted) material quickly turns opaque in frames B to D forming a dark region across the width of the specimen. Here, it is seen that the dark zone initially behind the leading shock, has caught up with the incident shock. If one measures the rate of growth of specific dark zones, values greater than the longitudinal wave velocity are obtained. These measurements, therefore, demonstrate that it must be pre-cracked material that is becoming visible rather than crack initiation and propagation because cracks cannot propagate faster than the longitudinal wave velocity in a material [105, 106].

### CONCLUSIONS

The current experimental evidence demonstrating the existence of the so-called failure wave in glass materials has been reviewed, and three theories attempting to explain the mechanism of failure were summarized. In terms of the existing data, it appears that the elastic shear/dilatant strain energy model by Grady [92] and the inelastic deformation model by Espinosa [93, 94] are more plausible than Clifton's model [91].

Recent results from plate impact experiments on three dense glass materials showed that behind the failed front, the shear stress shows a dependency on impact stress [59]. This data provides further information on the failure process and suggests a pressure/time dependence.

Results from symmetric Taylor tests showed that the failure front propagating in glass rods is highly irregular and the structure of the failure is material dependent. Results from

plate impact experiments further demonstrated the pressure/time dependence of the failure process. It is believed that dynamic failure of glasses is not due to a continuous boundary sweeping through the material (failure wave), but a time dependent process that evolves from inelastic deformation and subsequent microcracking due to shear failure.

### ACKNOWLEDGEMENTS

The authors acknowledge financial support and encouragement from QinetiQ, under contract SMC/4U1348. Also, we would like to thank Drs. S.M Walley, K. Tsembeles and B.A.M. Vaughan for valuable discussions, and D.L.A. Cross and R.P. Flaxman for technical support.

### REFERENCES

1. Kanel, G.I., S.V. Rasorenov, and V.E. Fortov, in *Shock Compression of Condensed Matter - 1991*, S.C. Schmidt, R.D. Dick, J.W. Forbes, and D.G. Tasker, Editors. 1992, Elsevier: Amsterdam. pp. 451-454.
2. Rasorenov, S.V., G.I. Kanel, V.E. Fortov, and M.M. Abasehov, *High Press. Res.*, 1991. 6: pp. 225-232.
3. Bless, S.J., N.S. Brar, and Z. Rosenberg, in *Shock Waves in Condensed Matter 1987*, S.C. Schmidt and N.C. Holmes, Editors. 1988, North Holland: Amsterdam. pp. 309-312.
4. Cagnoux, J., in *Shock Waves in Condensed Matter - 1981*, W.J. Nellis, L. Seaman, and R.A. Graham, Editors. 1982, American Institute of Physics: New York. pp. 392-396.
5. Dremin, A.N., A.V. Orlov, and A.M. Molodets, in *Proc. 2nd Int. Symp. on Intense Dynamic Loading and its Effects*, Z. Guanren and H. Shihui, Editors. 1992, Sichuan University Press: Chengdu, China. pp. 415-420.
6. Rosenberg, Z., D. Yaziv, and S.J. Bless, *J. Appl. Phys.*, 1985. 58: pp. 3249-3251.
7. Yeshurun, Y., G. Rosenberg, and Z. Rosenberg, in *Shock Waves in Condensed Matter*, Y.M. Gupta, Editor. 1986, Plenum Press: New York. pp. 431-435.
8. Dremin, A.N., A.V. Orlov, and A.M. Molodets, in *High Pressure Science and Technology 1993*, S.C. Schmidt, J.W. Shaner, G.A. Samara, and M. Ross, Editors. 1994, American Institute of Physics: New York. pp. 1445-1448.
9. de Rességuier, T. and F. Cottet, *J. Phys. IV France Colloq. C8 (DYMAT 94)*, 1994. 4: pp. 629-634.

10. Zhuk, A.Z., A.V. Ivanov, G.I. Kanel, and O.K. Rozanov, *Combust. Explos. Shock Waves*, 1993. **29**: pp. 760-764.
11. Akishin, A.I., S.V. Akimenko, N.V. Berbash, L.I. Ivanov, N.F. Orlov, Y.I. Tyutrin, and V.A. Yanushkevich, *Sov. Phys. Dokl.*, 1980. **25**: pp. 195.
12. Schmitt, D.R. and T.J. Ahrens, *J. Geophys. Res.*, 1989. **94**: pp. 5851-5871.
13. Gibbons, R.V. and T.J. Ahrens, *J. Geophys. Res.*, 1971. **76**: pp. 5489-5498.
14. Dandekar, D.P. and P.A. Beaulieu, in *Metallurgical and Materials Applications of Shock-Wave and High-Strain-Rate Phenomena*, L.E. Murr, K.P. Staudhammer, and M.A. Meyers, Editors. 1995, Elsevier: Amsterdam. pp. 211-218.
15. Ananin, A.V., O.N. Breusov, A.N. Dremin, S.V. Pershin, A.I. Rogacheva, and V.F. Tatsii, *Combust. Explos. Shock Waves*, 1974. **10**: pp. 504-508.
16. Ahrens, T.J., R.L. Fleischer, P.B. Price, and R.T. Woods, *Earth Planet. Sci. Letts*, 1970. **8**: pp. 420-426.
17. Jeanloz, R., T.J. Ahrens, J.S. Lally, G.L. Nord Jr., J.M. Christie, and A.H. Heuer, *Science*, 1977. **197**: pp. 457-459.
18. Rosenberg, Z., N.K. Bourne, and J.C.F. Millett, *J. Appl. Phys.*, 1996. **79**: pp. 3971-3974.
19. Bourne, N.K., Z. Rosenberg, and A. Ginzburg, *Proc. R. Soc. Lond. A*, 1996. **452**: pp. 1491-1496.
20. Dandekar, D.P., in *Structures under Shock and Impact IV*, N. Jones, C.A. Brebbia, and A.J. Watson, Editors. 1996, Computational Mechanics Publications: Southampton. pp. 439-448.
21. Bourne, N.K., J.C.F. Millett, and Z. Rosenberg, *Proc. R. Soc. Lond. A*, 1996. **452**: pp. 1945-1951.
22. Bourne, N.K., J.C.F. Millett, and Z. Rosenberg, *J. Appl. Phys.*, 1996. **80**: pp. 4328-4331.
23. Braue, W., H. Schneider, and U. Hornemann, in *Shock Compression of Condensed Matter 1995*, S.C. Schmidt and W.C. Tao, Editors. 1996, American Institute of Physics: Woodbury, New York. pp. 725-728.
24. Li, X.-Z., M. Nakano, Y. Yamauchi, K. Kishida, and K.A. Tanaka, in *Constitutive Relation in High/Very High Strain Rates*, K. Kawata and J. Shioiri, Editors. 1996, Springer-Verlag: Tokyo. pp. 209-216.
25. Li, X.-Z., M. Nakano, Y. Yamauchi, K. Kishida, and K.A. Tanaka, in *Proc. 2nd Int. Symp. on Impact Engineering*, C.-Y. Chiem, L.L. Wang, and S. Tanimura, Editors. 1996, Chinese Journal of Mechanics Press: Beijing. pp. 295-300.
26. Rosenberg, Z., *J. Phys. D: Appl. Phys.*, 1988. **21**: pp. 543-545.
27. Kleeman, J.D., *J. Geophys. Res.*, 1971. **76**: pp. 5499-5503.
28. Valitskii, V.P., N.A. Zlatin, and A.A. Kozhushko, *Sov. Phys. Tech. Phys.*, 1967. **12**: pp. 1546-1547.
29. Alekseevskii, V.P., V.F. Mazanko, L.E. Pechentkovskaya, and V.M. Falchenko, *Sov. Phys. Tech. Phys.*, 1979. **24**: pp. 477-479.
30. Korner, S.B., G.V. Krushkevich, and K.B. Yushko, *Sov. Phys. JETP*, 1967. **25**: pp. 980-985.
31. Ivanov, A.G. and V.I. Tsyppkin, *Mech. Compos. Mater.*, 1987. **23**: pp. 332-339.
32. Kobayashi, T., T. Sekine, O.V. Fatyanov, E. Takazawa, and Q.Y. Zhu, *J. Appl. Phys.*, 1998. **83**: pp. 1711-1716.
33. Li, X.-Z., M. Nakano, Y. Yamauchi, K. Kishida, and K.A. Tanaka, *J. Appl. Phys.*, 1998. **83**: pp. 3583-3594.
34. Khasainov, B.A. and B.S. Ermolaev, *Khim. Fiz.*, 1992. **11**: pp. 1588-1600.
35. Khasainov, B.A., B.S. Ermolaev, and H.N. Presles, in *Proc. 10th Int. Detonation Symposium*, J.M. Short and D.G. Tasker, Editors. 1995, Office of Naval Research: Arlington, Virginia. pp. 749-757.
36. Dandekar, D.P., in *Shock Compression of Condensed Matter - 1997*, S.C. Schmidt, D.P. Dandekar, and J.W. Forbes, Editors. 1998, American Institute of Physics: Woodbury, New York. pp. 525-528.
37. Ginzburg, A. and Z. Rosenberg, in *Shock Compression of Condensed Matter - 1997*, S.C. Schmidt, D.P. Dandekar, and J.W. Forbes, Editors. 1998, American Institute of Physics: Woodbury, New York. pp. 529-531.
38. Kobayashi, T., T. Sekine, O.V. Fatyanov, E. Takazawa, and Q.Y. Zhu, in *Shock Compression of Condensed Matter - 1997*, S.C. Schmidt, D.P. Dandekar, and J.W. Forbes, Editors. 1998, American Institute of Physics: Woodbury, New York. pp. 797-800.
39. Dandekar, D.P., *J. Appl. Phys.*, 1998. **84**: pp. 6614-6622.
40. Bourne, N.K., J.C.F. Millett, and J.E. Field, *Proc. R. Soc. Lond. A*, 1999. **455**: pp. 1275-1282.
41. Nakano, M., Y. Yamauchi, K. Kishida, K. Watanabe, M. Hara, N. Ozaki, K.A. Tanaka, and M. Yoshida, in *Impact Response of Materials and Structures*, V.P.W. Shim, S. Tanimura, and C.T. Lim, Editors. 1999, Oxford University Press: Oxford. pp. 215-220.
42. Arndt, J., H. Hornemann, and W.F. Müller, *Phys. Chem. Glasses*, 1971. **12**: pp. 1-7.
43. Reynard, B., M. Okuno, Y. Shimada, Y. Syono, and C. Willaime, *Phys. Chem. Minerals*, 1999. **26**: pp. 432-436.
44. Stepanov, G.V. and V.V. Astanin, *Strength Mater.*, 1978. **10**: pp. 344-346.
45. Feng, R., *J. Appl. Phys.*, 2000. **87**: pp. 1693-1700.

46. Millett, J.C.F., N.K. Bourne, and Z. Rosenberg, in *Shock Compression of Condensed Matter - 1999*, M.D. Furnish, L.C. Chhabildas, and R.S. Hixson, Editors. 2000, American Institute of Physics: Melville, New York. pp. 607-610.
47. He, H.L., X.G. Jin, F.Q. Jing, and G.I. Kanel, *Chinese Phys. Letts*, 1997. **14**: pp. 538-541.
48. Dhareshwar, L.J., N. Gopi, C.G. Murali, B.S. Narayan, and U.K. Chatterjee, *Laser Particle Beams*, 1997. **15**: pp. 297-316.
49. Sugiura, H., A.R. Ikeda, K. Kondo, and T. Yamadaya, *J. Appl. Phys.*, 1997. **81**: pp. 1651-1655.
50. Millett, J.C.F., N.K. Bourne, and Z. Rosenberg, *J. Appl. Phys.*, 2000. **87**: pp. 8457-8460.
51. Mallory, H.D. and W.S. McEwan, *J. Appl. Phys.*, 1961. **32**: pp. 2421-2424.
52. Syono, Y., T. Goto, Y. Nakagawa, and M. Kitamura, in *High-Pressure Research: Applications to Geophysics*, M.H. Manghnani and S. Akimoto, Editors. 1977, Academic: New York. pp. 477-489.
53. Stöffler, D. and U. Hornemann, *Meteoritics*, 1972. **7**: pp. 371-394.
54. Boslough, M.B., T.J. Ahrens, and A.C. Mitchell, *Geophys. J. R. Astron. Soc.*, 1986. **84**: pp. 475-489.
55. Millett, J. and N. Bourne, *Scripta mater.*, 2000. **42**: pp. 681-685.
56. Millett, J. and N. Bourne, *Scripta mater.*, 2000. **43**: pp. 77-82.
57. Bourne, N.K. and J.C.F. Millett, *Proc. R. Soc. Lond. A*, 2000. **456**: pp. 2673-2688.
58. Lambert, P. and M.A. Lange, *J. Non-Cryst. Solids*, 1984. **67**: pp. 521-542.
59. Radford, D.D., W.G. Proud, and J.E. Field. in *Shock Compression of Condensed Matter*. 2001. Atlanta, Georgia.
60. Bourne, N.K. and J.C.F. Millett, *J. Phys. IV France Pr. 9 (DYMAT 2000)*, 2000. **10**: pp. 281-286.
61. Bourne, N.K. and J.C.F. Millett, *J. Appl. Phys.*, 2001. **89**: pp. 5368-5371.
62. Bourne, N.K., J.C.F. Millett, and Z. Rosenberg, *J. Appl. Phys.*, 1997. **81**: pp. 6670-6674.
63. Bourne, N.K., J.C.F. Millett, Z. Rosenberg, and N.H. Murray, *J. Mech. Phys. Solids*, 1998. **46**: pp. 1887-1908.
64. Bourne, N.K. and Z. Rosenberg, in *Shock Compression of Condensed Matter 1995*, S.C. Schmidt and W.C. Tao, Editors. 1996, American Institute of Physics: Woodbury, New York. pp. 567-572.
65. Bourne, N.K. and Z. Rosenberg, in *Shock Compression of Condensed Matter - 1997*, S.C. Schmidt, D.P. Dandekar, and J.W. Forbes, Editors. 1998, American Institute of Physics: Woodbury, New York. pp. 849-852.
66. Bourne, N.K., Z. Rosenberg, and J.E. Field, *J. Appl. Phys.*, 1995. **78**: pp. 3736-3739.
67. Bourne, N.K., Z. Rosenberg, Y. Mebar, T. Obara, and J.E. Field, *J. Phys. IV France Colloq. C8 (DYMAT 94)*, 1994. **4**: pp. 635-640.
68. Bourne, N.K., Z. Rosenberg, and J.C.F. Millett, in *Structures under Shock and Impact IV*, N. Jones, C.A. Brebbia, and A.J. Watson, Editors. 1996, Computational Mechanics Publications: Southampton. pp. 553-562.
69. Brar, N.S., Z. Rosenberg, and S.J. Bless, *J. Phys. IV France Colloq. C3 (DYMAT 91)*, 1991. **1**: pp. 639-644.
70. Brar, N.S., S.J. Bless, and Z. Rosenberg, *Appl. Phys. Letts*, 1991. **59**: pp. 3396-3398.
71. Brar, N.S. and S.J. Bless, *High Press. Res.*, 1992. **10**: pp. 773-784.
72. Brar, N.S., in *Shock Compression of Condensed Matter - 1999*, M.D. Furnish, L.C. Chhabildas, and R.S. Hixson, Editors. 2000, American Institute of Physics: Melville, New York. pp. 601-606.
73. Kanel, G.I. and A.M. Molodets, *Sov. Phys. Tech. Phys.*, 1976. **21**: pp. 226-232.
74. Kanel, G.I., S.V. Razorenov, A.V. Utkin, H.L. He, F.Q. Jing, and X.G. Jin, *High Press. Res.*, 1998. **16**: pp. 27-44.
75. Grady, D.E., in *Shock Compression of Condensed Matter 1995*, S.C. Schmidt and W.C. Tao, Editors. 1996, American Institute of Physics: Woodbury, New York. pp. 9-20.
76. Grady, D.E., *Mech. Mater.*, 1998. **29**: pp. 181-203.
77. Grady, D.E., W.J. Murri, and P.S. de Carli, *J. Geophys. Res.*, 1975. **80**: pp. 4857-4861.
78. Cagnoux, J. 1985, Poitiers.
79. Cagnoux, J., *J. Phys. France Colloq. C5 (DYMAT 85)*, 1985. **46**: pp. 343-350.
80. Bourne, N.K., L.C. Forde, J.C.F. Millett, and J.E. Field, *J. Phys. IV France Colloq. C3 (EURODYMAT 97)*, 1997. **7**: pp. 157-162.
81. Kim, K.Y. and K.W. Sachse, *J. Mater. Sci.*, 2000. **35**: pp. 3197-3205.
82. Lopatin, C.M., S.J. Bless, and N.S. Brar, *J. Appl. Phys.*, 1989. **66**: pp. 593-595.
83. Lopatin, C.M., S.J. Bless, and N.S. Brar, in *Shock Compression of Condensed Matter - 1989*, S.C. Schmidt, J.N. Johnson, and L.W. Davidson, Editors. 1990, Elsevier: Amsterdam. pp. 633-636.
84. Sundaram, S. and R.J. Clifton, in *Shock Compression of Condensed Matter - 1997*, S.C. Schmidt, D.P. Dandekar, and J.W. Forbes, Editors. 1998, American Institute of Physics: Woodbury, New York. pp. 517-520.
85. Clifton, R.J., M. Mello, and N.S. Brar, in *Shock Compression of Condensed Matter - 1997*, S.C. Schmidt, D.P. Dandekar, and J.W. Forbes,

- Editors. 1998, American Institute of Physics: Woodbury, New York. pp. 521-524.
86. Bless, S.J., N.S. Brar, G. Kanel, and Z. Rosenberg, *J. Amer. Ceram. Soc.*, 1992. **75**: pp. 1002-1004.
87. Raiser, G. and R.J. Clifton, in *High Pressure Science and Technology 1993*, S.C. Schmidt, J.W. Shaner, G.A. Samara, and M. Ross, Editors. 1994, American Institute of Physics: New York. pp. 1039-1042.
88. Espinosa, H.D. and Y.P. Xu, *J. Amer. Ceram. Soc.*, 1997. **80**: pp. 2061-2073.
89. Partom, Y., *Int. J. Impact Engng*, 1998. **21**: pp. 791-799.
90. Cazamias, J.U., P.S. Fiske, and S.J. Bless, in *Fundamental Issues and Applications of Shock-Wave and High-Strain-Rate Phenomena*, K.P. Staudhammer, L.E. Murr, and M.A. Meyers, Editors. 2001, Elsevier: New York. pp. 173-179.
91. Clifton, R.J., *Appl. Mech. Rev.*, 1993. **46**: pp. 540-546.
92. Grady, D.E. 1995, Sandia National Laboratories: Albuquerque, New Mexico.
93. Espinosa, H.D., in *Structures under Shock and Impact IV*, N. Jones, C.A. Brebbia, and A.J. Watson, Editors. 1996, Computational Mechanics Publications: Southampton. pp. 449-458.
94. Espinosa, H.D., Y.P. Xu, and N.S. Brar, *J. Amer. Ceram. Soc.*, 1997. **80**: pp. 2074-2085.
95. Rosenberg, Z. and N.S. Brar, in *High Pressure Science and Technology 1993*, S.C. Schmidt, J.W. Shaner, G.A. Samara, and M. Ross, Editors. 1994, American Institute of Physics: New York. pp. 1707-1710.
96. Rosenberg, Z. and N.S. Brar, *Appl. Acoustics*, 1994. **41**: pp. 377-386.
97. Rosenberg, Z. and N.S. Brar, *J. Appl. Phys.*, 1995. **77**: pp. 1443-1448.
98. Rosenberg, Z. and Y. Partom, *J. Appl. Phys.*, 1985. **58**: pp. 3072-3076.
99. Rosenberg, Z. and Y. Partom, in *Shock Waves in Condensed Matter - 1985*, Y.M. Gupta, Editor. 1986, Plenum: New York. pp. 525-530.
100. Rosenberg, Z. and N.S. Brar, *J. Appl. Phys.*, 1988. **63**: pp. 349-354.
101. Rosenberg, Z., in *Shock Compression of Condensed Matter - 1999*, M.D. Furnish, L.C. Chhabildas, and R.S. Hixson, Editors. 2000, American Institute of Physics: Melville, New York. pp. 1033-1037.
102. Murray, N.H., N.K. Bourne, J.E. Field, and Z. Rosenberg, in *Shock Compression of Condensed Matter - 1997*, S.C. Schmidt, D.P. Dandekar, and J.W. Forbes, Editors. 1998, American Institute of Physics: Woodbury, New York. pp. 533-536.
103. Bless, S.J., N.S. Brar, and Z. Rosenberg, in *Shock Compression of Condensed Matter - 1989*, S.C. Schmidt, J.N. Johnson, and L.W. Davidson, Editors. 1990, Elsevier: Amsterdam. pp. 939-942.
104. Rosakis, A.J., O. Samudrala, and D. Coker, *Science*, 1999. **284**: pp. 1337-1340.
105. Schardin, H. and W. Struth, *Z. tech. Phys.*, 1937. **18**: pp. 474-477.
106. Schardin, H., in *Fracture*, B.L. Averbach, D.K. Felbeck, G.T. Hahn, and D.A. Thomas, Editors. 1959, John Wiley: New York. pp. 297-330.

## Lateral stress behaviour of alumina ceramics

B.A.M. Vaughan, W.G. Proud and J.E. Field.

*PCS Group, Cavendish Laboratory, Madingley Road, Cambridge CB3 0HE, UK.*

**Abstract.** T-gauges have been used to measure lateral stress in five alumina ceramics subjected to shock compression. A review of the experiments carried out at the Cavendish Laboratory is presented. When manganin gauges are used to measure lateral stress near an alumina's Hugoniot Elastic Limit, a two-step stress profile is often observed. Failure fronts are assumed to occur across the second rise in the lateral stress profile. It is shown that the time for this rise to occur after impact decreases with longitudinal stress and increases with distance into the target. When a symmetric alumina flyer or cover plate is used however, no two-step profile is observed.

### INTRODUCTION

There has been a great deal of interest in the properties of brittle materials shocked near to their Hugoniot Elastic Limit (HEL). At these stress regimes, there have been observations of a failed state in glasses and ceramics behind the elastic wave. Some contradictory results have been published for the same ceramics with some authors claiming, for example that pure alumina shows compaction but no sign of fracturing even when shocked to twice its HEL [1] whereas Rosenberg and Yeshurun [2] demonstrated a reduction in spall strength for alumina shocked to only half of the HEL. Rosenberg *et al.* [3] concluded that the HEL marks the point at which cracks coalesce into a network. Much work has been undertaken on glasses of various types, see for example refs [4,5]. Rasorenov *et al.* [6] and Kanel *et al.* [7] showed that failure in shocked glass propagated behind a compressive shock. This phenomena has been called a failure wave, but is also referred to as a failure front. These papers resulted in a number of studies into this phenomenon [8-31].

Failure fronts have also been sought in other brittle materials [32, 33, 42]. Some researchers claim that in certain brittle materials, such as alumina, failure does not propagate very far into the material from the impact surface [34-36]. Others claim this may be a measurement artefact [37, 38]. Brar and Espinosa [49] give a review of the types of experimental arrangements used to detect this failure state and summarise three proposed mechanisms for failure put forward by Clifton [11], Grady [39] and Espinosa [40].

This paper summarises the results in five types of alumina ceramic using embedded lateral gauges, taken from previous work at the Cavendish Laboratory [35, 36, 44, 46-48]. A typical response from a lateral T-gauge, indicated in Fig. 2 (a) shows an initial rise to a plateau, followed by a second rise to a higher value. This onset of the second rise is

taken to be the failure front across which the lateral stress increases and the shear strength drops [18]. This loss in shear strength is shown to be dependent on impact stress and distance into the target. Other factors, such as the projectile material or whether a metal or ceramic cover plate is placed ahead of the target, seems to affect the presence of a failure front. There appears to be no loss in shear strength when an alumina ceramic flyer or cover plate is used.

## MATERIALS

Five alumina ceramics have been studied using the plate impact facility at the Cavendish Laboratory [41]. These alumina ceramics are referred to as 880, 975, 999, Sintox FA and Sintox CL. They differ in their purity (880, 975, 999 representing 88.0%, 97.5% and 99.9% pure respectively) and production techniques. Sintox FA is 96.0% pure and Sintox CL is 98.5% pure. The two types of Sintox also exhibit some differences in their chemical composition. Table 1 gives some of their measured elastic properties.

Material	HEL (GPa)	Density (kg m <sup>-3</sup> )	Longitudinal wave velocity, $c_L$ (mm $\mu$ s <sup>-1</sup> )	Shear wave velocity, $c_S$ (mm $\mu$ s <sup>-1</sup> )	Bulk wave velocity, $c_O$ (mm $\mu$ s <sup>-1</sup> )	Poisson ratio, $\nu$
880	5.4 ± 0.6	3546	9.09	5.41	6.61	0.23
975	7.7 ± 0.7	3797	10.30	6.07	7.55	0.23
999	13 ± 1	3989	10.82	6.39	7.91	0.23
Sintox FA	11 ± 1	3694	9.89	5.80	7.28	0.24
Sintox CL	11 ± 1	3864	10.73	6.21	7.97	0.25

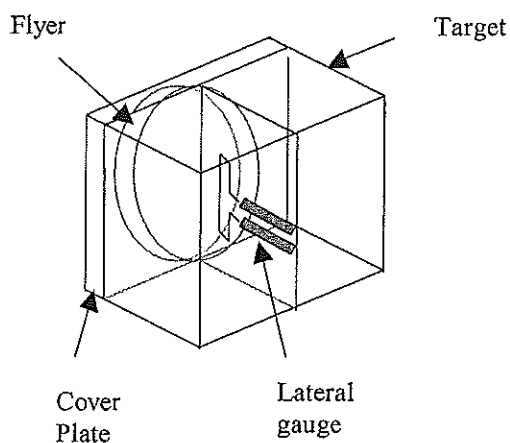
Table 1 Material properties of the five aluminas tested.

## EXPERIMENT

The samples were typically 50 mm square and *ca.* 15 mm thick. These were cut to produce two pieces of dimensions 50 x 25 x 15 mm and reassembled with low viscosity epoxy after inserting one or two manganin t-gauges of type J2M-SS-580SF-025 at known distances from the impact surface (see Fig. 1). A constant current was supplied to the gauges during an impact event, and the output voltages recorded on a digital storage scope. These were used to calculate the lateral stress in the target using the resistance calibration data of Rosenberg and Partom [43].

Several experiments were performed on each material. To study the effect of impact stress on the failure state behind the elastic wave, a gauge was placed at 2 mm from the impact surface and the velocity of the flyer plate was varied. In some cases, a higher impedance flyer (tungsten) was used to achieve higher stresses than possible with copper

Figure 1 Target arrangement showing the placement of the lateral gauge.



at the highest attainable velocities. To study the effects of propagation distance into the material, gauges were placed at increasing distances from the impact surface while the impact stress was held constant. In some cases, one experiment yielded data for both avenues of investigation. Finally the effect of the flyer material has been studied briefly using a ceramic flyer of the same type as the target. It has also been shown that placing a 2 mm thick ceramic or copper cover plate on the impact surface affects

the formation of a two-step stress profile [35]. It has been observed that when a ceramic cover plate or flyer is used, there is no second rise in the gauge response, indicating that the target material has not undergone a reduction of shear strength during the recording time of the experiment.

## RESULTS

The results from lateral gauge experiments on five alumina ceramics are presented in Figures 2 and 3.

### Stress dependence

Figure 2 shows the measured lateral stress for T-gauges placed at 2 mm from the impact face for the five variants of alumina studied. Three types of behavior are shown. The typical case shows the lateral stress rising to an initial plateau and remaining at that level for some time, before rising to a higher level. This second rise or step, is taken as an indication of a loss in shear strength. The effect appears to be material dependent, with higher purity alumina withstanding a higher longitudinal stress before immediate loss in shear strength. The second type of behaviour, shown in Fig. 2 (a), occurs at high longitudinal stress, where the lateral stress rises to a high level in a single step. This indicates that by the time the shock has reached the gauge, the target has failed immediately behind the initial elastic wave. The third type of behaviour, as shown in Fig. 2 (d), is observed when symmetric alumina flyers or alumina cover plates are employed and shows a single rise to a plateau at a low lateral stress. This level has approximately the same value as the initial plateau reached in a typical trace subjected to a similar longitudinal stress. This implies that the material has not failed and has maintained its initial shear strength. The apparent velocity of the failure front can be determined using the time at which the second rise in lateral stress occurs at a known distance from the impact face. This velocity increases as impact stress increases, up to a point where the lateral gauge records a single step, indicating that the failure front is progressing immediately behind the elastic wave. The loss in shear strength inferred by

the onset of a second rise in lateral stress may be a time-dependent phenomena, occurring when damage caused by the initial shock wave grows to a given point. The speed of growth of this damage, which may take the form of microcracks, depends on the strength of the shock.

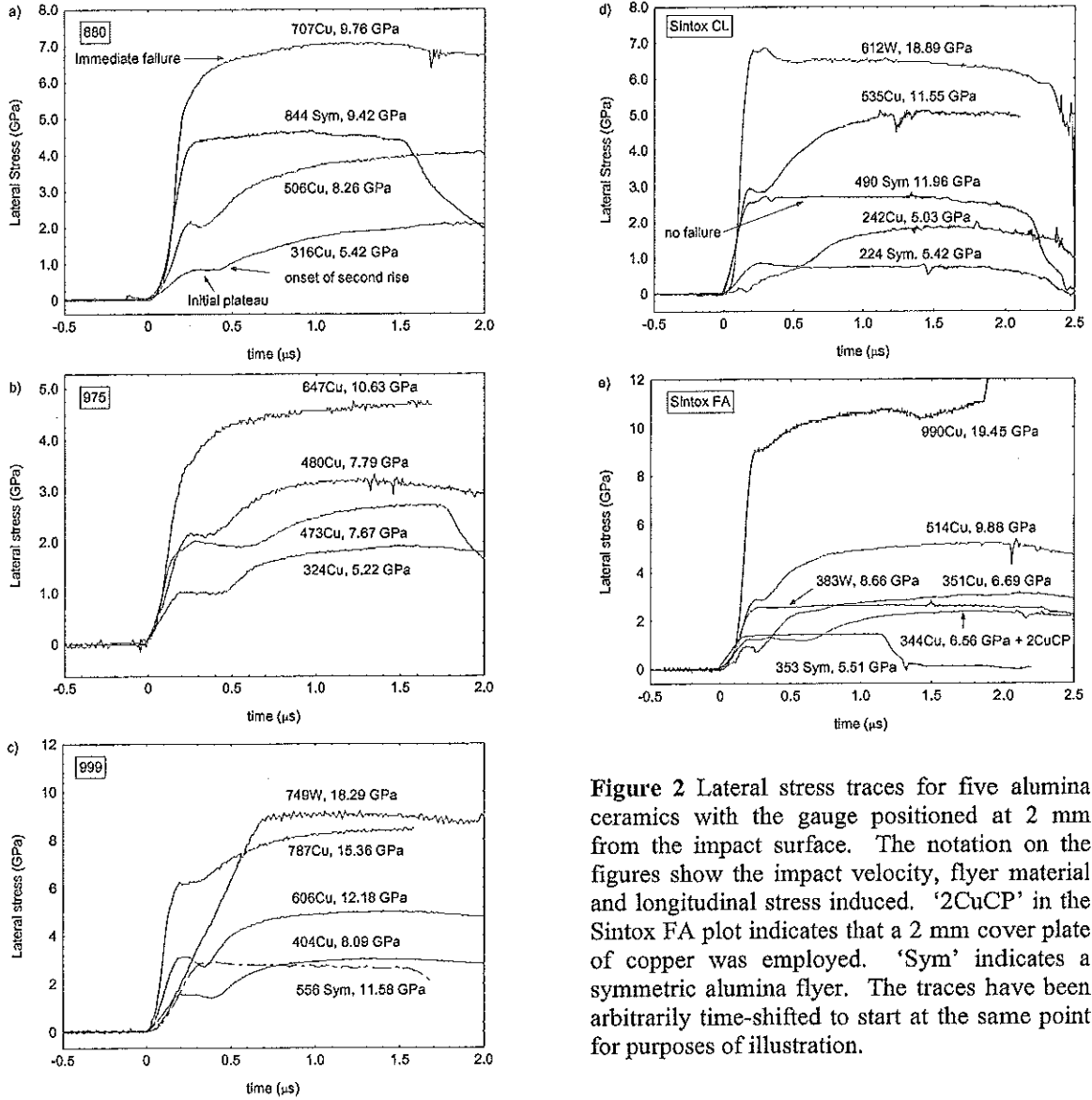


**Figure 2** Lateral stress traces for five alumina ceramics with the gauge positioned at 2 mm from the impact surface. The notation on the figures show the impact velocity, flyer material and longitudinal stress induced. '2CuCP' in the Sintox FA plot indicates that a 2 mm cover plate of copper was employed. 'Sym' indicates a symmetric alumina flyer. The traces have been arbitrarily time-shifted to start at the same point for purposes of illustration.

## Distance dependence

Figure 3 shows lateral stress recorded at different distances from the impact face under similar loading conditions. The lateral stress reaches the same initial level for a given longitudinal stress and does not decay with distance into the target. Failure is therefore not simply directly related to the lateral stress experienced. The velocity of the failure front decreases with increasing distance and no second rise in lateral stress is observed after five or six millimetres into the target, as shown in Fig. 3 (a). This deceleration is not linear as shown by the quadratic nature of the time-distance (t-x) diagram shown in Fig. 4. The velocity of the failure front increases with longitudinal stress, approaching the velocity of the elastic wave in the alumina.

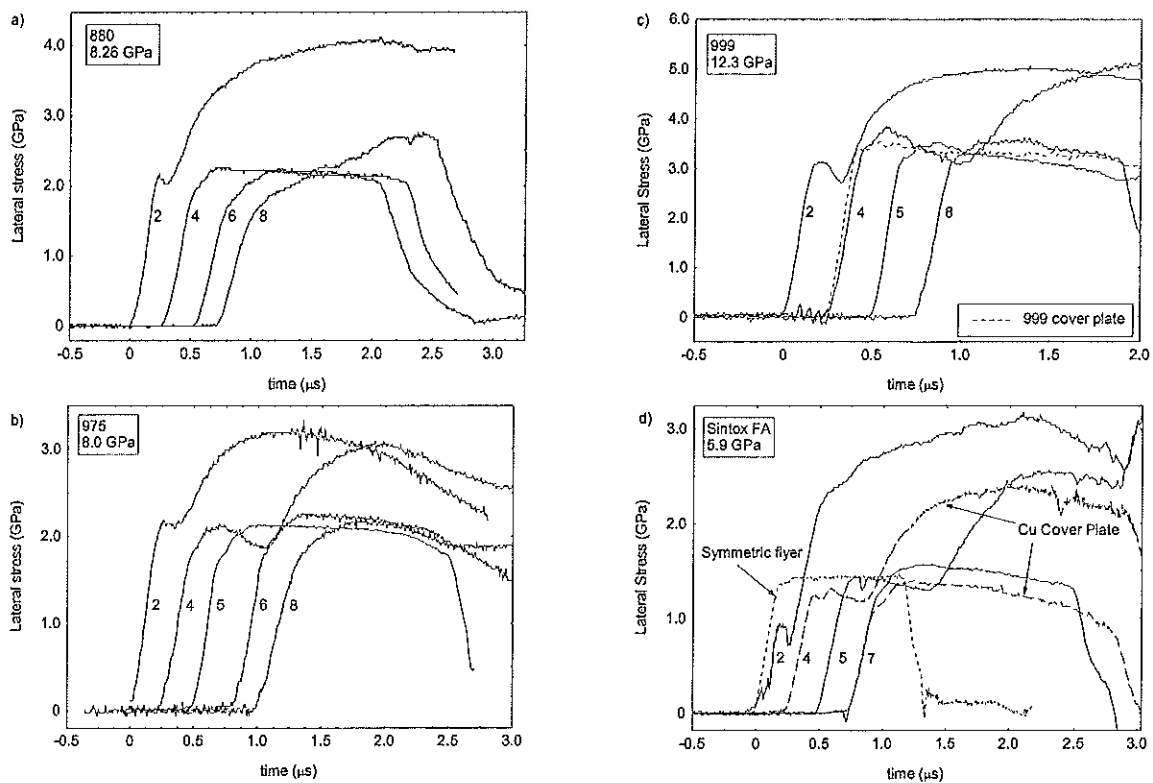


**Figure 3** Lateral stress traces for four of the alumina ceramics showing the effect of target thickness. The longitudinal stress induced is shown in the key for each plot. The notation next to the curves shows the distance of the gauge from the impact surface in millimetres. All flyers were OFHC copper, except where indicated. The traces have been arbitrarily time-shifted for purposes of illustration.

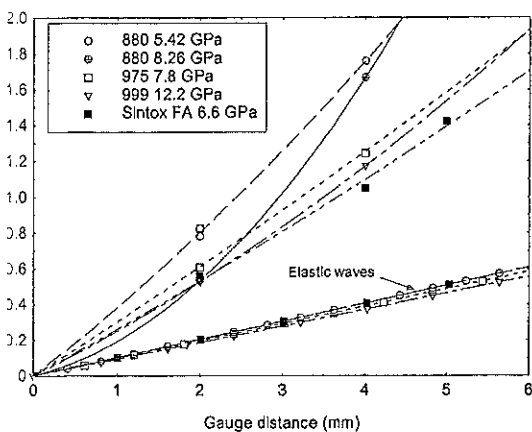


**Figure 4** Time for onset of the second rise as distance from impact face increases. Second order polynomial curves are fitted to the data. Failure velocity can be calculated from the inverse gradient and can be seen to decrease with distance into the target. For comparison, the elastic wave velocities are also plotted.

### Cover plates and symmetric impact

A cover plate of alumina or copper was placed ahead of the target and impacted by a metal flyer. Experiments were also performed in which the target did not include a cover plate. In targets without cover plates the lateral stress response shows a two-step structure. At similar longitudinal stresses in targets with alumina cover plates, the lateral stress does not exhibit a two-step structure, as shown in Fig. 3 (c). Instead the lateral stress rises to a single plateau at approximately the same level as the first plateau in targets without a cover plate. In cases such as that in Fig. 3 (d) where the cover plate is copper at similar longitudinal stress, a two-step structure is observed near to the impact face. When an alumina flyer impacts a target without a cover plate in a symmetric impact, a single-step up to the first plateau is recorded by the embedded lateral gauge. Fig. 3 (d) shows an example of this behaviour.

### DISCUSSION

The reason for the phenomena reported here is unclear, but may be related to the geometry of the target and the fact that it must be divided to include the gauge. This introduces stress concentrations either side of the gauge. This can be avoided by using the method of Rasorenov *et al.* [6] instead of manganin gauges. The rear surface of the alumina is monitored with a VISAR during loading. If a failed region exists within the target, it will have a lower impedance than the shocked material. The release wave from the rear of the target will encounter this impedance difference and will partially reflect from it back towards the rear of the target. This manifests as a small reloading pulse superimposed on the main velocity trace ahead of the release wave from the rear of the flyer plate.

Although the difference in the time between the first and second rise in lateral stress has been interpreted as a velocity, it may instead be the case that failure is a time dependent phenomena. Radford *et al.* [50] presented high-speed photograph sequences of glass materials which show an apparent failure front velocity that exceeds the elastic wave speed. This can be explained as a time related effect, with microcrack failure

commencing close behind the elastic wave, but not being detectable by the camera until the cracks reach a critical size. Bourne *et al.* [44] and Murray *et al.* [45] have demonstrated that precursor decay in aluminas steadies to a constant value after *ca.* 6 mm. This is much less than that for glasses, for which the precursor amplitude decreases up to 15 mm. In aluminas, this is similar to the distance over which the second rise in lateral stress is observed. However, it has yet to be shown that these effects are related. Grady, using VISAR [37] found no evidence of decay, and Marom *et al.* [38] have suggested that the apparent decay in the Hugoniot elastic limit is probably a measurement artefact, resulting from the relatively slow response times of manganin gauges.

## SUMMARY

Manganin T-gauges have been used to measure lateral stresses in five aluminas. A characteristic two-step structure has been observed in aluminas at different distances into the target when copper flyers are employed to induce different longitudinal stress levels. The time at which the second rise occurs after impact decreases as longitudinal stress increases, and increases as the gauge is placed further into the alumina. This two-step profile is not observed when alumina flyers are used or when an alumina cover plate is placed on the target. Although no two-step profiles were observed when using tungsten flyers, this is because the longitudinal stresses applied were so high that the alumina failed immediately. It is unclear why a symmetric flyer or a two millimetre alumina cover plate should prevent the second rise in lateral stress from occurring, whereas a copper flyer or cover plate does not. This is currently under investigation by the authors.

## ACKNOWLEDGEMENTS

Thanks go to S.M Walley for providing valuable help in locating many of the references.

## REFERENCES

- [1] Longy, F. and Cagnoux, J. 'Macro- and micro-mechanical aspect of shock-loading of aluminas', in *Impact Loading and Dynamic Behaviour of Materials*, ed. C.Y. Chiem, H.-D. Kunze and L.W. Meyer, publ. Oberursel, Germany, DGM Informationsgesellschaft mbH: pp. 1001-1008, (1988).
- [2] Rosenberg, Z. and Yeshurun, Y. 'The relation between ballistic efficiency and compressive strength of ceramic tiles', *Int. J. Impact Eng.* 7, pp. 357-362, (1988).
- [3] Rosenberg, Z., Brar, N.S. and Bless, S.J. 'Determination of the strength of shock loaded ceramics using double impact techniques', in *Shock Compression of Condensed Matter-1989*, ed. S.C. Schmidt, J.N. Johnson and L.W. Davidson, publ. Amsterdam, Elsevier: pp. 385-388, (1990).
- [4] Bless, S.J., Brar, N.S. and Rosenberg, Z. 'Strength of soda-lime glass under shock compression', in *Shock Compression of Condensed Matter-1987*, ed. S.C. Schmidt and N.C. Holmes, publ. Amsterdam, North Holland: pp. 309-312, (1988).
- [5] Rosenberg, Z., Marmor, E. and Mayselless, M. 'On the hydrodynamic theory of long-rod penetration', *Int. J. Impact Eng.* 10, pp. 483-486, (1990).
- [6] Rasorenov, S.V., Kanel, G.I., Fortov, V.E. and Abasehov, M.M. 'The fracture of glass under high pressure impulsive loading', *High Press. Res.* 6, pp. 225-232, (1991).

- [7] Kanel, G.I., Rasorenov, S.V. and Fortov 'The failure waves and spallations in homogenous brittle materials', in *Shock Compression of Condensed Matter-1991*, ed. S.C. Schmidt, R.D. Dick, J.W. Forbes and D.G. Tasker, publ. Amsterdam, Elsevier: pp. 451-454, (1992).
- [8] Brar, N.S., Rosenberg, Z. and Bless, S.J. 'Spall strength and failure waves in glass', *J. Phys. IV France 1, Colloq. C3 (DYMAT 91)* pp. 639-644, (1991).
- [9] Bless, S.J., Brar, N.S., Kanel, G. and Rosenberg, Z. 'Failure waves in glass', *J. Amer. Ceram. Soc.* **75**, pp. 1002-1004, (1992).
- [10] Brar, N.S. and Bless, S.J. 'Failure waves in glass under dynamic compression', *High Press. Res.* **10**, pp. 773-784, (1992).
- [11] Clifton R.J. 'Analysis of failure waves in glasses', *Appl. Mech. Rev* **46**, pp. 540-546, (1993).
- [12] Raiser G. and Clifton R.J. 'Failure waves in uniaxial compression of an aluminosilicate glass', in *High Pressure Science and Technology 1993* ed. S.C. Schmidt, J.W. Shaner, G.A. Samara and M. Ross, publ. New York, American Institute of Physics: pp. 1039-1042, (1994).
- [13] Bourne, N.K., Rosenberg, Z. and Field, J.E. 'High-speed photography of compressive failure waves in glasses', *J. Appl. Phys.* **78**, pp. 3736-3739, (1995).
- [14] Bourne, N.K., Millett, J.C.F. and Rosenberg, Z. 'Failure in a shocked high- density glass', *J. Appl. Phys.* **80**, pp. 4328-4331, (1996).
- [15] Bourne, N.K., Millett, J.C.F. and Rosenberg, Z. 'The shock wave response of a filled glass', *Proc. R. Soc. Lond. A* **452**, pp. 1945-1951, (1996).
- [16] Bourne, N.K., Rosenberg, Z. and Ginzburg, A. 'The ramping of shock waves in three glasses', *Proc. R. Soc. Lond. A* **452**, pp. 1491-1496, (1996).
- [17] Bourne, N.K., Rosenberg, Z. and Millett, J.C.F. 'The plate impact response of three glasses', in *Structures under Shock and Impact IV*, ed. N. Jones, C.A. Brebbia and A.J. Watson, publ. Southampton, Computational Mechanics Publications: pp. 553-562, (1996).
- [18] Bourne, N.K., Millett, J.C.F. and Rosenberg, Z. 'On the Origin of failure waves in glass', *J. Appl. Phys.* **81**, pp. 6670-6674, (1997).
- [19] Espinosa, H.D. 'Modelling failure waves in brittle materials', in *Structures under Shock and Impact IV*, ed. N. Jones, C.A. Brebbia and A.J. Watson, publ. Southampton, Computational Mechanics Publications: pp. 449-458, (1996).
- [20] Espinosa, H.D. and Xu, Y.P. 'Micromechanics of failure waves in glass. 1: Experiments', *J. Amer. Ceram. Soc.* **80**, pp. 2061-2073, (1997).
- [21] Espinosa, H.D., Xu, Y.P. and Brar, N.S. 'Micromechanics of failure waves in glass. 2: Modelling', *J. Amer. Ceram. Soc.* **80**, pp. 2074-2085, (1997).
- [22] He, H.L., Jin, X.G., Jing, F.Q. and Kanel, G.I. 'Dynamic failure of shock-loaded glass', *Chinese Phys. Letts.* **14**, pp. 538-541, (1997).
- [23] Clifton R.J., Mello, M. and Brar, N.S. 'Effect of shear on failure waves in soda-lime glass', in *Shock Compression of Condensed Matter-1997*, ed. S.C. Schmidt, D.P. Dandekar and J.W. Forbes, publ. Woodbury, New York, American Institute of Physics: pp. 521-524, (1998).
- [24] Kanel, G.I., Rasorenov, S.V., Utkin, A.V., He, H.L., Jing, F.Q. and Jin, X.G. 'Influence of the load conditions on the failure wave in glasses', *High Press. Res.* **16**, pp. 27-44, (1998).
- [25] Partom, Y. 'Modeling failure waves in glass', *Int. J. Impact Eng.* **21**, pp. 791-799, (1998).
- [26] Chen, Z. and Xin, X. 'An analytical and numerical study of failure waves', *Int. J. Solids Structures* **36**, pp. 3977-3991, (1999).
- [27] Abeyaratne, R. and Knowles, J.K. 'A phenomenological model for failure waves in glass', *Shock Waves* **10**, pp. 301-305, (2000).
- [28] Brar, N.S. 'Failure waves in glass and ceramics under shock compression', in *Shock Compression of Condensed Matter-1999*, ed. M.D. Furnish, L.C. Chhabildas and R.S. Hixson, publ. Melville, New York, American Institute of Physics: pp. 601-606, (2000).
- [29] Bourne, N.K. and Millett, J.C.F. 'Decay of the elastic precursor in a filled glass', *J. Appl. Phys.* **89**, pp. 5368-5371, (2001).
- [30] Cazamias, J.U., Fiske, P.S. and Bless, S.J. 'Sound speeds of post-failure wave glass', in *Fundamental Issues and Applications of Shock-Wave and High-Strain-Rate Phenomena*, ed. K.P. Staudhammer, L.E. Murr and M.A. Meyers, publ. New York, Elsevier: pp. 173-179, (2001).
- [31] Radford, D.D., Proud, W.G. and Field, J.E. 'The deviatoric response of three dense glasses under shock loading conditions', (to appear in *Shock Compression of Condensed Matter-2001* ed. M.D. Furnish (2002)).

- [32] Orphal, D.L., Kozhushko, A.A. and Sinani, A.B. 'Possible detection of failure wave velocity in SiC using hypervelocity penetration experiments', in *Shock Compression of Condensed Matter-1999*, ed. M.D. Furnish, L.C. Chhabildas and R.S. Hixson, publ. Melville, New York, American Institute of Physics: pp. 577-580, (2000).
- [33] Plekov, O.A., Eremeev, D.N. and Naimark, O.B. 'Failure wave as resonance excitation of collective burst modes of defects in shocked brittle materials', *J. Phys. IV France* **10**, Pr. 9 (DYMAT 2000) pp. 811-816, (2000).
- [34] Staehler, J.M., Predebon, W.W. and Pletka, B.J. 'The response of a high purity alumina to plate impact testing', in *High Pressure Science and Technology 1993* ed. S.C. Schmidt, J.W. Shaner, G.A. Samara and M. Ross, publ. New York, American Institute of Physics: pp. 745-748, (1994).
- [35] Murray, N.H., Millett, J.C.F., Proud, W.G. and Rosenberg, Z. 'Issues surrounding lateral stress measurements in alumina ceramics', in *Shock Compression of Condensed Matter-1999*, ed. M.D. Furnish, L.C. Chhabildas and R.S. Hixson, publ. Melville, New York, American Institute of Physics: pp. 581-584, (2000).
- [36] Murray, N.H. and Proud, W.G. 'Measurement of lateral stress and spall strength in ceramics', in *Fundamental Issues and Applications of Shock-Wave and High-Strain-Rate Phenomena*, ed. K.P. Staudhammer, L.E. Murr and M.A. Meyers, publ. New York, Elsevier: pp. 151-156, (2001).
- [37] Grady, D.E. 'Shock wave compression of brittle solids', *Mech. Mater.* **29**, pp. 181-203, (1998).
- [38] Marom, H., Sherman, D. and Rosenberg, Z. 'Decay of elastic waves in alumina', *J. Appl. Phys.* **88**, pp. 5666-5670, (2000).
- [39] Grady, D.E. 'Dynamic properties of ceramic materials', *Sandia National Laboratory Report, SAND94-3266*, (1995).
- [40] Espinosa, H.D. 'On the dynamic shear resistance of ceramic composites and its dependence on applied multiaxial deformation', *Int. J. Solids Structures* **32**, pp. 3105-3128, (1995).
- [41] Bourne, N.K., Rosenberg, Z., Johnson, D.J., Field, J.E., Timbs, A.E. and Flaxman, R.P. 'Design and construction of the UK Plate impact facility', *Meas. Sci. Technol.* **6**, pp. 1462-1470, (1995).
- [42] Bourne, N.K., Millett, J.C.F. and Pickup, I.M. 'Delayed failure in shocked silicon carbide', *J. Appl. Phys.* **81**, pp. 6019-6023, (1997).
- [43] Rosenberg, Z. and Partom, Y. 'Lateral stress measurement in shock-loaded targets with transverse piezoresistance gauges', *J. Appl. Phys.* **58**, pp. 3072-3076, (1985).
- [44] Bourne, N.K., Millett, J.C.F., Rosenberg, Z. and Murray, N.H. 'On the shock induced failure of brittle solids', *J. Mech. Phys. Solids*, **46**, 10, pp. 1887-1908, (1998).
- [45] Murray, N.H., Bourne, N.K. and Rosenberg, Z. 'Precursor decay in several aluminas', in *Shock Compression of Condensed Matter-1995*, ed. S.C. Schmidt and W.C. Tao, publ. Woodbury, New York, American Institute of Physics: pp. 491-494, (1996).
- [46] Millett, J.C.F. and Bourne, N.K. 'Lateral stress measurements in a shock loaded alumina: Shear strength and delayed failure', *J. Mater. Sci.* **36**, pp. 3409-3414, (2001).
- [47] Murray, N.H. and Field, J.E., 'Plate impact experiments on ceramics: Progress report', *Shock Physics Group, PCS, Madingley Road, Cambridge, CB3 0HE, UK*, Report No. **PCS/SP1053**, (1999).
- [48] Murray, N.H., 'Response of ceramics to plate impact loading', *Shock Physics Group, PCS, Madingley Road, Cambridge, CB3 0HE, UK*, Report No. **PCS/SP1063**, (2000).
- [49] Brar, N.S. and Espinosa, H.D. 'A review of micromechanics of failure waves in silicate glasses', *Chem. Phys. Reports*, **17** (1-2), pp. 317-342, (1998).
- [50] Radford, D.D., Proud, W.G. and Field, J.E. 'Dynamic failure of glasses', *these proceedings*, (2001).

# The Shock and Ballistic Properties of Sand.

W.G. Proud, S. G. Grantham, B.A.M. Vaughan, K. Tsembeles and J.E. Field

*Physics and Chemistry of Solids Group, Cavendish Laboratory, Madingley Road,  
Cambridge, CB3 0HE, Great Britain.*

## ABSTRACT

Granular materials present particular problems for modelling. Generally, a two or more component mixture is further complicated by a particle size distribution in at least one of the phases. Sand is widely distributed throughout the natural environment, used as a commercial building material in mortars and concretes and in bags as a simple ballistic shield. This paper presents techniques and results from plate impact experiments and ballistic trials where quartz sand is subjected to either rapid loading.

## 1. INTRODUCTION

In a blast or high-velocity impact, a material will experience a range of loading conditions. Locations near the stimulus may see conditions which approximate 1-D loading whereas as materials further from this zone will see lower pressures and a 3-D loading. It is important for successful modelling to include both types of response in order to predict the response of large masses of materials to particular scenarios.

Plate impact has been used for many years to load materials at high-strain rates, up to  $10^8 \text{ s}^{-1}$  [1]. By measuring the stress induced by the impact of a carefully aligned plate of a well-characterised material, and using either gauges [2] or velocity interferometry [3] to monitor the target response the longitudinal behaviour of the material can be obtained.

Previous work from this laboratory has defined the Hugoniot and other high-strain rate properties for various materials such as glasses [4], cements [5] and polymers [6]. Recent work has concentrated on glasses where free volumes on the atomic or micron scale allows a ramping response and other phenomena, such as failure waves, to be observed [7].

The use of gauges allows one-dimensional measurements to be made at a single point within a specimen, but if we want to make two-dimensional measurements within the specimen during a dynamic event then we need to use Digital Speckle Radiography (DSR), a technique based on Digital Speckle Photography (DSP). In DSP a random pattern of “speckles” are produced by shining a coherent laser light source upon a specimen’s surface. This random pattern is captured digitally using a CCD camera and a second image captured after some form displacement or distortion to the surface. A cross-correlation algorithm is then employed to correlate the two images to determine where the random pattern has moved. By performing this cross-correlation in a series of sub-images from the main images then a map of local displacements can be calculated. The difference between DSR and DSP is the way in which the random speckle pattern is produced. In DSR the random pattern is produced by introducing a seeded plane of X-ray opaque grains into the sample. An X-ray of this layer produces an image which has the appearance of a speckle pattern. By utilising flash X-rays, images of dynamic events can be taken due to the short nanosecond exposures achievable with flash X-ray systems. The reference and deformed radiographs can then be scanned into a personal computer using a flatbed scanner and the cross-correlation algorithm can be used as in standard DSP. By performing a series of experiments and varying the delay time of the X-rays and by moving the seeded plane within the sample a full three-dimensional flow field can be constructed. The algorithm used for DSR studies was developed by Sjodahl [8] and calculates the correlation function in the Fourier plane to give an accuracy of better than 0.01 pixels.

The technique of DSR was first carried out by Synnergren *et al.*[9], on polyester samples and has since successfully been applied to glass [10], concrete [11] and sand [12]. Sand is ideally suited to these types of measurements as a layer of lead filings can easily be introduced into a sand specimen during manufacture. In this paper an example of the type of measurements DSR can achieve for a ballistic impact in sand is demonstrated.

## 2. EXPERIMENTAL

### (i) Plate Impact Studies

The sand used in the plate impact experiments was a quartz sand with a particle distribution centred between 150 - 212  $\mu\text{m}$  where 82 % by mass of the particles lay. The theoretical maximum density of the material was 2.55  $\text{g cm}^{-3}$  and in the beds used were  $45\pm 3$  % porous.

Experiments were performed using a single stage light gas gun at the Cavendish Laboratory [13]. This has a 5 m long, 50 mm bore barrel and uses air or helium up to 350 atmospheres as the propellant achieving velocities up to 1200  $\text{m s}^{-1}$ . The projectile consists of a plate of copper 10 mm thick mounted on the front of a polycarbonate sabot.

The sample consists of a 3mm bed of sand inside a copper cell. The cell is in four parts as shown in figure 1. A cover plate 2 mm thick fronts the cell, a manganin stress gauge is mounted in epoxy between this plate and the 2-3 mm thick copper plate behind it. The third plate has a 3 mm recess into which the sand is loaded. The recessed plate has a 1 mm thick rear face after which a second stress gauge is located. The rear plate is 10 mm copper.

In these experiments the sample mount was aligned to an accuracy of  $<1 \mu\text{m}$ , an angle of  $<1 \text{ mrad}$ , to the end of the barrel using a dial gauge prior to each experiment thus allowing a highly planar impact. The impact velocity is measured using a sequential array of shorting pins mounted at the end of the barrel to an accuracy of 0.1%.

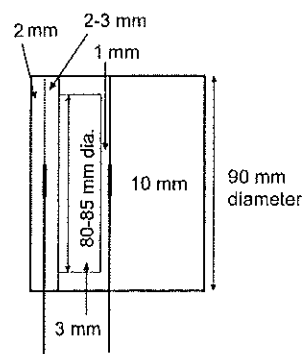


Figure 1. The Cell. All cell components are made from copper (Cu 101).

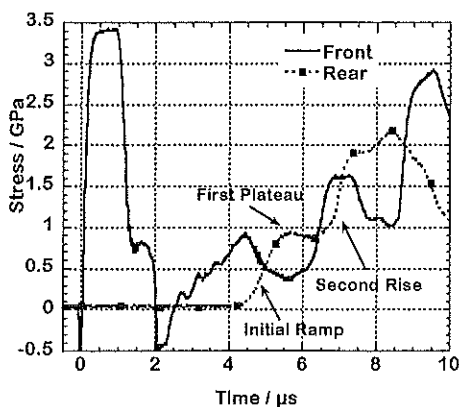
The gauges act in two ways, firstly as time of arrival sensors and secondly by recording the stress history.

### (ii) Digital Speckle Radiography

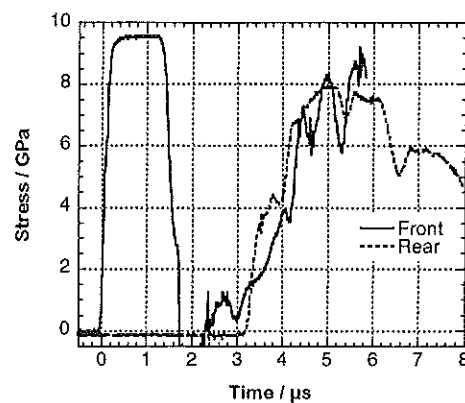
In these experiments, a polymethylmethacrylate (PMMA) container with interior dimensions of  $60 \times 70 \times 30 \text{ mm}^3$  was filled with  $300 - 600 \text{ }\mu\text{m}$  sand and the same sieve cut was used for the lead filings to produce the random pattern. A copper (XM) rod 5 mm in diameter and 50 mm in length was shot at the sand at a velocity of  $100 \text{ m s}^{-1}$  ( $\pm 4 \text{ m s}^{-1}$ ) and experiments were performed using delays of  $60 \text{ }\mu\text{s}$  and  $120 \text{ }\mu\text{s}$  with the lead layer on the impact plane and at  $60 \text{ }\mu\text{s}$  with the lead layer 5 mm and 10 mm from the impact plane.

### 3. RESULTS

Figure 2 shows the data from shots at velocities of 200, 500 and  $969 \text{ m s}^{-1}$  using the plate impact gun with a 10 mm Cu impactor plate. There are similarities between the gauge outputs seen in all experiments. The front gauge shows a rapid rise to a flat-topped pulse. The height of this pulse is defined by the copper Hugoniot as both the impactor and the front plates of the target are copper. The stress level increases with impact velocity and the width of the initial pulse is defined by the thickness of second plate in the target.



(a)



(b)

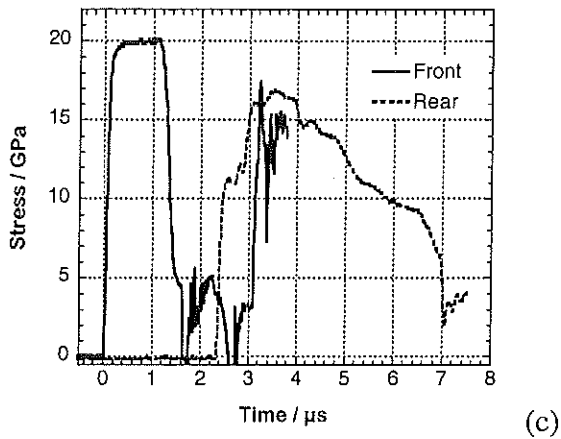


**Figure 2.** The output of the gauges from experiments with impact velocities of (a)  $200 \text{ m s}^{-1}$ , (b)  $505 \text{ m s}^{-1}$  and (c)  $969 \text{ m s}^{-1}$ . The time bases of all experiments are set so the initial rise of the front gauge is at  $0 \text{ } \mu\text{s}$ . The stress measured is that in the copper cell.

In some of the front gauge traces, there is a dip immediately before the steep initial rise. This is due to capacitive linking between the gauge, the epoxy surrounding, which acts as a dielectric, and the copper plates on either side of the gauge [14].

Given the granular nature of sand, a ramp is seen due to the collapse of pores in the system. The rear gauge trace shows this ramping in the first part of its signal (see figure 2 (a)). As the impact velocity increases the pore collapse occurs over a shorter time and the initial rise of the second gauge trace steepens. In all cases a first plateau is reached corresponding to a stress level on the principal Hugoniot of the sand. The second rise on the rear gauge trace is due to stress waves being reflected in the sand-filled cavity due to impedance mismatches between the sand and the copper cell. This second rise gives information on the compressed sand, the analysis of which is not entered upon here. Sand is a statistical material and, therefore, some variation can be expected from sample to sample. However, a repeat experiment at  $500 \text{ m s}^{-1}$  shows excellent reproducibility as illustrated in figure 3.

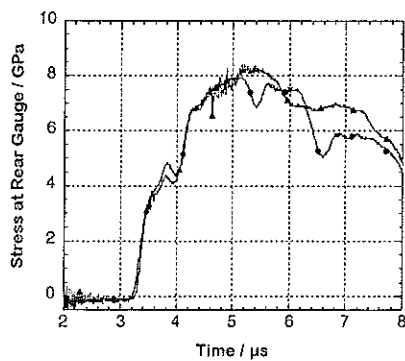


**Figure 3.** Reproducibility of impact at  $500 \text{ m s}^{-1}$ . The rear gauge traces from two separate experiments are shown.

By combining the sound speed of the sand obtained from the gauge traces with the theoretical maximum density of the sand, it is possible to derive a Hugoniot of the material. It should be emphasised that this is an approximation. While it can be argued that the velocity should be multiplied by the initial density of the sand, initial tests using the CAST<sup>TM</sup>/ EDEN Eulerian finite difference hydrocode suggest that using the theoretical maximum density gives predictions which match the stress level of the first plateau. It is clear, however, that a model which takes into account the kinetics of pore collapse is required. The initial approximation to the Hugoniot is shown below, figure 4, together with the variation of shock speed with particle velocity, figure 5 and is in agreement with previously published data on sand [15].

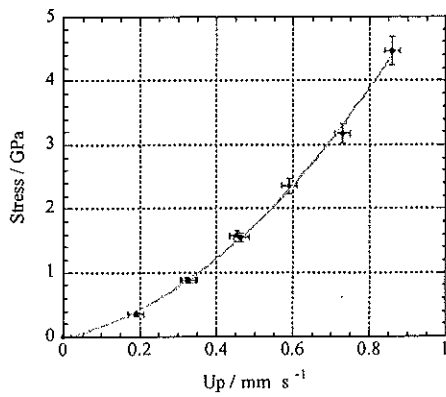


**Figure 4.** Hugoniot of quartz sand in Stress / Particle velocity ( $U_p$ ) space

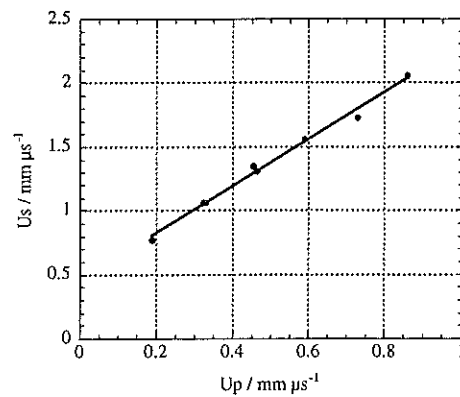


**Figure 5.** Shock velocity as a function of particle velocity.

**(ii) Ballistic Tests**

An example of a measured displacement field can be seen in figure 6 with the displacement vectors scaled up by a factor of 2. In figure 6, the two smaller speckle regions at either side of the image are fiducial markers used to eliminate any rigid body motions introduced by the scanning process. The sand in this figure can clearly be seen flowing away from the projectile tip both forwards and to the sides. This type of behaviour is expected from a granular material which has cavities and pores into which it can flow when subjected to an impact. A more quantitative study can be obtained by plotting the average y-component of displacement ahead of the projectile. A

plot of the displacements 60  $\mu$ s after impact with the seeded plane 0, 5 and 10 mm away from the impact plane is shown in figure 7.

The behaviour of the displacements as the seeded plane moves further away from the impact plane is as expected qualitatively but our research gives quantitative information on displacement. Additionally, the penetration and crater volume is measurable with conventional x-rays. Marked differences have also been seen between dry and water-saturated sand. The displacement reduces away from the tip of the projectile in all three cases but with the gradient reducing as the offset increases. The displacements also decrease with increased offset from the impact plane due to the influence of the projectile reducing.

To see the effect of penetration depth in the sand a plot can also be made of the y-displacements ahead of the projectile for the 60 and 120  $\mu$ s delay cases and is shown in figure 8. The gradients and magnitudes of displacement are very similar for the two cases but offset by the additional penetration in the 120  $\mu$ s case. This suggests that the sand is free to compact and absorb the force of the impact even with the additional penetration depth.

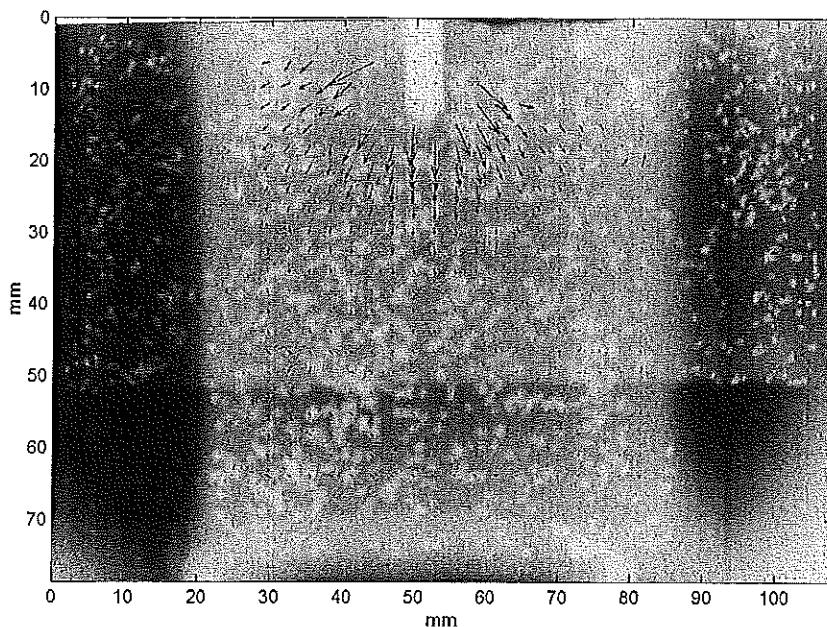


Figure 6. 60  $\mu$ s delay, lead layer on impact plane.

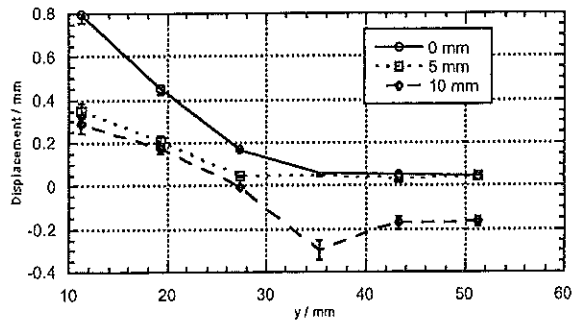


Figure 7. 60  $\mu$ s delay, seeded layer 0, 5 and 10 mm from impact plane.

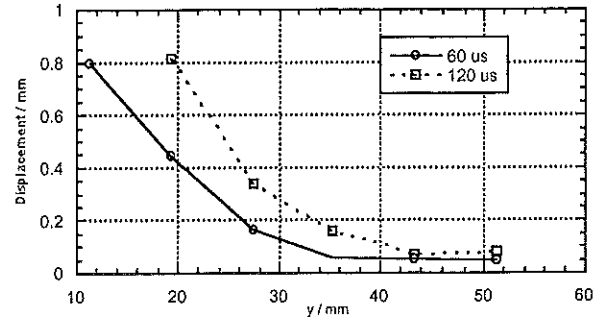


Figure 8. 60 and 120  $\mu$ s delays on impact plane.

#### 4. CONCLUSIONS

Two complimentary studies have been performed to assess the shock and ballistic response of sand. The Hugoniot of the sand has been obtained. This is useful in determining the behaviour of the material under strong blast and immediately in front of a penetrator, a zone crucial with regard to ultimate penetration depth. The Hugoniot data is in agreement with earlier data published by van Thiel [15] but has the advantage of good time resolution of the gauge output to allow the subtleties of the shock pulse to be modelled.

The ballistic study has revealed the movement of sand at lower pressures surrounding the impactor and in the far field

The combination of the detail from these experiments is vital if a full hydrocode model of sand is required.

#### ACKNOWLEDGEMENTS

Daniel Tam and Les Taylor of NSWC, Indian Head, Maryland are acknowledged for their support of this research. Daniel Cross of the PCS Group, Cavendish Laboratory is acknowledged for his technical assistance and support. Benedict Taylor and Alun Davies of the PCS Group are thanked for their help in characterising the sand.

## REFERENCES

- [1] Duvall, G.E. and R.A. Graham, *Phase transitions under shock wave loading*. Rev. Mod. Phys., 1977. **49**: p. 523-579.
- [2] Rosenberg, Z., D. Yaziv, and Y. Partom, *Calibration of foil-like manganin gauges in planar shock wave experiments*. J. Appl. Phys., 1980. **51**: p. 3702-3705.
- [3] Barker, L.M. and R.E. Hollenbach, *Laser interferometer for measuring high velocities of any reflecting surface*. J. Appl. Phys., 1972. **43**: p. 4669-4675.
- [4] Bourne, N.K., Z. Rosenberg, and A. Ginzburg, *The ramping of shock waves in three glasses*. Proc. R. Soc. Lond. A, 1996. **452**: p. 1491-1496.
- [5] Tsembeles, K., et al., *The shock Hugoniot properties of cement paste up to 5 GPa*, in *Shock Compression of Condensed Matter - 1999*, M.D. Furnish, L.C. Chhabildas, and R.S. Hixson, Editors. 2000, American Institute of Physics: Melville, New York. p. 1267-1270.
- [6] Walley, S.M., D. Xing, and F.J. E, *Mechanical properties of three transparent amorphous polymers in compression at a very high rate of strain*, in *Impact and Dynamic Fracture of Polymers and Composites*, J.G. Williams and A. Pavan, Editors. 1995, Mech Eng Publications: London. p. 289-303.
- [7] Radford, D.D., W.G. Proud, and J.E. Field. *The Deviatoric Response of Three Dense Glasses under Shock Loading Conditions*. in *Shock Compression of Condensed Matter*. 2001. Atlanta: American Physical Society
- [8] M.Sjodahl, "Electronic Speckle Photography: Increased Accuracy by Non Integral Pixel Shifting", Applied Optics, **33** (1994), pp 6667-6673.
- [9] P. Synnergren, H.T. Goldrein, W.G. Proud, "Application of Digital Speckle Photography to Flash X-Ray Studies of Internal Deformation Fields in Impact Experiments", Applied Optics, **38** (1999), pp 4030-4036.
- [10] S.G. Grantham, W.G. Proud, "Digital Speckle X-Ray Flash Photography", Proceedings of the 12<sup>th</sup> APS topical meeting on shock compression of condensed matter, 2001 (in press).
- [11] P. Synnergren, H.T. Goldrein, "Dynamic Measurements of Internal Three-Dimensional Displacement Fields with Digital Speckle Photography and Flash X-Rays", Applied Optics, **38** (1999), pp 5956-5961.
- [12] H.T. Goldrein, S.G. Grantham, W.G.Proud, J.E. Field, "The Study of Internal Deformation Fields in Granular Materials Using 3D Digital Speckle X-Ray Flash Photography", Proceedings of the 12<sup>th</sup> APS topical meeting on shock compression of condensed matter, 2001 (in press).
- [13] Bourne, N.K., et al., *Design and construction of the UK plate impact facility*. Meas Sci Technol, 1995. **6**: p. 1462-1470.
- [14] Bourne, N.K. and Z. Rosenberg, *On the ringing observed in shock-loaded piezoresistive stress gauges*. Meas. Sci. Technol., 1997. **8**: p. 570-573
- [15] Thiel, M.v., *Compendium of Shock Wave Data*. Report UCRL-50108, 1966, University of California, Livermore.

# DYNAMIC FRAGMENTATION OF BRITTLE SOLIDS: CONTINUUM VERSUS DISCRETE APPROACHES

François HILD\* and Christophe DENOUAL°

\*LMT-Cachan, ENS de Cachan / CNRS / Université Paris 6  
61 Avenue du Président Wilson, F-94235 Cachan Cedex, France.

°DGA/DCE/CTA, Département Matériaux, Surfaces, Protection  
16 bis Avenue Prieur de la Côte d'Or, F-94114 Arcueil Cedex, France.

## ABSTRACT

Modeling dynamic fragmentation of brittle materials usually implies to choose between a discrete description of the fragments and a continuum approach at the structural level. A damage model that can be used in the whole range of loadings (from quasi-static to dynamic ones) is derived. A scaling strategy leading to characteristic volume, time and stress is used to choose the mesh size relevant to a local approach. The deterministic or probabilistic nature of fragmentation is discussed with respect to those parameters. Qualitative and quantitative validations are given by using a post-mortem analysis of impacted ceramic tiles, a real-time visualization technique for studying the degradation during impact and a moiré technique to measure the strains. A discussion using the single/multiple fragmentation criterion is proposed.

## 1. INTRODUCTION

The single or multiple fragmentation of brittle materials (e.g., engineering ceramics, concrete, glass and rocks) is analyzed herein. Single fragmentation is observed in many brittle materials when the stress rate is low. It follows that a weakest link hypothesis is made [1] and a Weibull model [2] is used to fit experimental data (Fig. 1)

$$P_F = 1 - \exp[-Z_{eff} \lambda_t(\sigma_F)] \text{ with } \lambda_t(\sigma_F) = \lambda_0 \left( \frac{\sigma_F}{S_0} \right)^m \quad (1)$$

where  $P_F$  denotes the failure probability,  $\lambda_t$  is the defect

density,  $m$  the Weibull modulus,  $S_0$  a scale parameter relative to a reference density  $\lambda_0$  and  $Z_{eff}$  the effective volume, surface or length [3]. The constant  $S_0^m / \lambda_0$  is the Weibull scale parameter. In the following, when no special mention is made, the development is valid for any space dimension  $n$  (i.e., 1, 2 or 3). Otherwise, it will be clearly stated for which space dimension the results are valid. It can be noted that the previous formulation (i.e., Eq. (1)) enters the framework of a Poisson point process of intensity  $\lambda_t$  [4,5]. The material microstructure (Fig. 2) is therefore approximated by point defects of density  $\lambda_t$  with random locations.

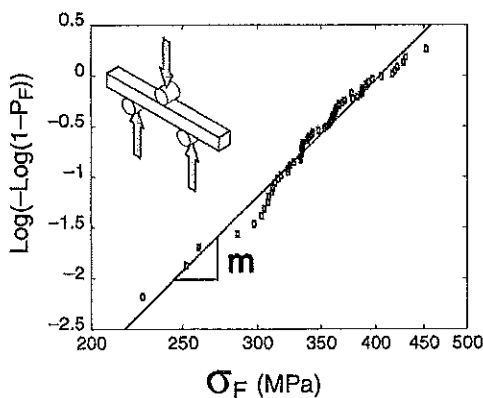


Figure 1. Weibull plot for a silicon carbide ceramic.

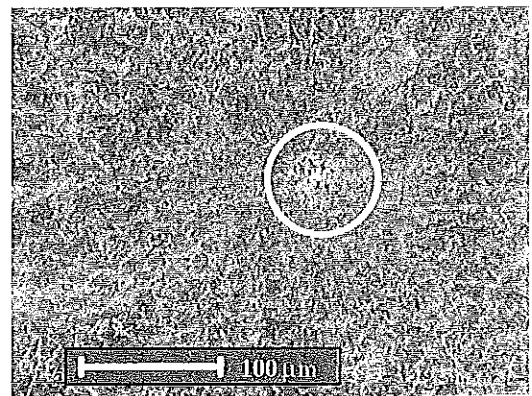


Figure 2. Initial porosity in a silicon carbide ceramic.

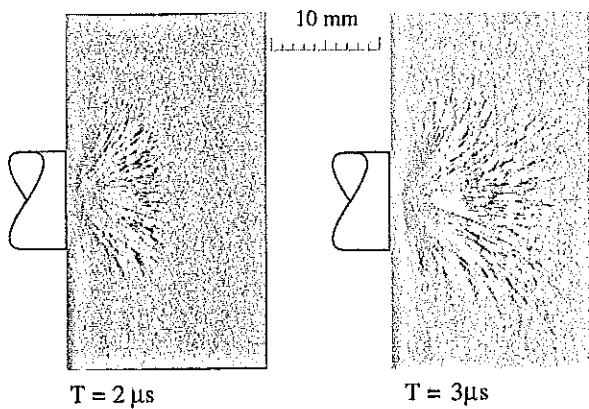


Figure 3. Fragmentation during impact of a steel blunt cylinder on a SiC ceramic (the projectile velocity is 203m/s). Cracks nucleate on defects and propagate at a constant velocity [6].

Multiple fragmentation occurs during impact on brittle materials. In the bulk of the material, damage in tension is observed when the hoop stress induced by the radial motion is sufficiently large to generate fracture in mode I on micro-defects such as porosities or inclusions.

To analyze the degradation mechanisms in SiC ceramics during impact, an edge-on impact configuration is used with a steel blunt cylinder projectile fired at different velocities. The polished surface of the ceramic is recorded each 500 nano-seconds with a high-speed camera that allows one to follow the damage generation and kinetics.

The main damage mechanism is shown to be microcracking in mode I [6] (Fig. 3). One can notice the anisotropic orientation and the high density of small cracks. Crack nucleation and shielding are assumed to be the prevalent mechanisms involved in the tensile degradation. A probabilistic model is proposed and the dimensionless number of nucleated defects is derived. It is found that the number of nucleated defects reaches a maximum value, which is only a function of the Weibull modulus and the space dimension when properly normalized.

Based upon the previous (discrete) fragmentation study, a damage description and a kinetic law can be derived within a Continuum Damage Mechanics framework [7]. The kinetic law is written in an incremental form in order to be implemented in a (commercial) finite element code. A so-called multi-scale model is introduced to yield probabilistic simulations instead of classical deterministic computations. A comparison between experimental measurements and numerical simulations is then carried out.

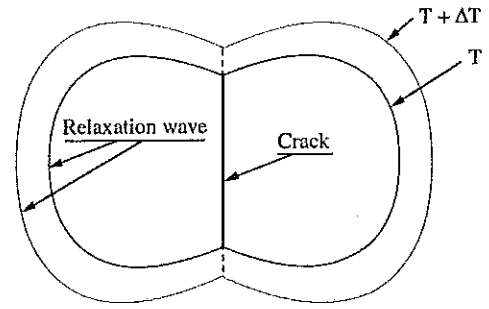


Figure 4. Relaxation around a propagating crack at time  $T$  and  $T + \Delta T$ .

## 2. FRAGMENTATION ANALYSIS

When a fracture is initiated in mode I, the local stress state is modified around the crack by a stress relief wave which is a complex function of time, crack velocity and stress wave celerity (Fig. 4). To understand why a crack nucleates, one has to model the interaction of the zone (i.e., volume, surface or length) affected by the stress relief and other defects that would nucleate. The behavior of a flaw around a nucleated one can be described by two different cases:

- the flaw is far from the nucleated one and the microscopic stress state is not affected,
- the flaw is in the interaction zone and the microscopic tensile stress is decreasing, i.e., no cracks are emanating from this potential initiation site.

A third case may occur in which the flaw is in the affected zone but the local tensile stress increases, i.e., initiation may occur. It is assumed that this case is insignificant in this problem.

The direction of the microscopic maximum principal stress is assumed to be constant, which allows one to use  $\sigma = \max[\sigma_1, \sigma_2, \sigma_3]$  instead of the stress tensor as an equivalent failure stress. The flaw nucleation can be represented on a space-time graph (Fig. 5). The space location of the defects is represented in a simple abscissa (instead of a three-, two- or one-dimensional representation) of an x-y graph where the y-axis represents the time (or stress) to failure of a given defect. The first crack nucleation occurs at time  $T_1$  (corresponding to a stress  $\sigma[T_1]$ ) at the space location  $M_1$  and produces an 'obscured zone'  $Z_0(T-T_1)$  increasing with time. At time  $T_2$  (corresponding to a stress  $\sigma[T_2] > \sigma[T_1]$ ) a second defect nucleates in a non-affected zone and produces its own obscured zone. The third and fourth defects do not nucleate because they are obscured by the first and both first and second defect, respectively. It is worth noting that the stress levels in overlapping obscured zones cannot be greater than the highest initiation stress associated to the considered obscured zones. The space-time graph is composed of the *union* of obscured zones in which no flaws can initiate and the complementary zone in which

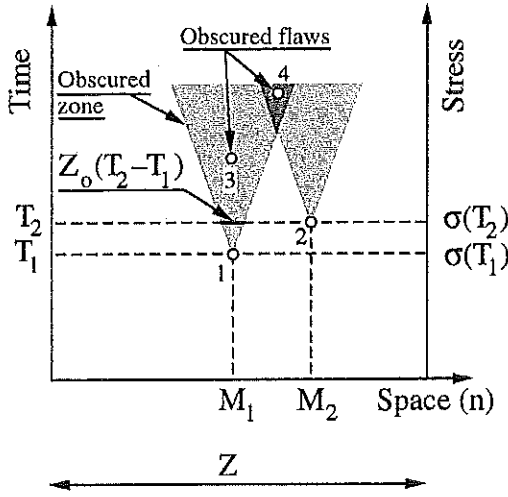


Figure 5. Fragmentation and obscuration phenomena.

defects can nucleate. Because different obscured zones may overlap (i.e., a flaw can be obscured by one or more other cracks), it is preferable to define the conditions of non-obscuration for a given defect by examining the *inverse* problem. It consists in considering the past history of a defect that would break at a time  $T$ . The defect will break if no defects exist in its *horizon*. For a given flaw  $D$  its horizon is defined as a space-time zone in which a defect will always obscure  $D$  (Fig. 6). Outside the horizon, a defect will never obscure  $D$ .

The flaw distribution can be split into two parts and the average density of broken flaws can be written as

$$\lambda_b(\sigma) = \lambda_t(\sigma) - \lambda_{obs}(\sigma) \quad (2)$$

where  $Z\lambda_b(\sigma)$  denotes the mean number of flaws that may break in a zone of measure  $Z$  (i.e., volume ( $n=3$ ), surface ( $n=2$ ) or length ( $n=1$ )) for a stress less than or equal to  $\sigma$ . The subscripts indicate the effectively broken flaws (b), the obscured flaws (obs), and the total number of flaws able to break (t).

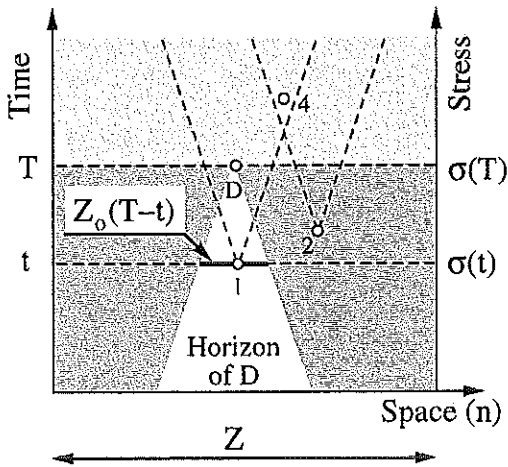


Figure 6. Schematic of the horizon of a defect  $D$ .

Furthermore, we assume that the distribution of total flaws is modeled by a Poisson point process of intensity  $\lambda_t$ . New cracks will initiate only if the defect exists in the considered zone and if no defects exist in its horizon so that

$$\frac{d\lambda_b}{dt}(T) = \frac{d\lambda_t}{dt}(T)[1 - P_o(T)] \text{ with } \lambda_b(0) = 0 \quad (3)$$

where  $1 - P_o$  is the probability that no defects exist in the horizon. The variable  $1 - P_o$  can be split into an infinity of events defined by the probability of finding at  $t$  a new defect during a time step  $dt$  in an obscuration zone  $\Omega_o(T-t)$ . This probability increment is written by using a Poisson point process of intensity  $d\lambda_t/dt$ . Those *independent events* can be used to provide an expression for  $P_o$

$$P_o(T) = 1 - \exp\left[-\int_0^T \frac{d\lambda_t}{dt}(t)Z_o(T-t)dt\right] \quad (4)$$

where  $Z_o(T-t)$  is the measure of the obscuration zone at  $T$  for a defect that would break at  $t$ . At the beginning of loading, no interactions occur and  $\lambda_b(T) \approx \lambda_t(T)$  and as more and more defects nucleate  $\lambda_b(T) \ll \lambda_t(T)$ . It is expected that the density of broken flaws saturates when  $T \rightarrow +\infty$  even though the total density of flaws able to break may approach infinity. Equation (4) can be derived by using results of mathematical morphology [8]. The probability of being in a non-obscured zone ( $1 - P_o$ ) is then expressed through the measure of the mean obscuration zone  $M(T)$ . The latter is calculated by averaging at time  $T$  the measure of the obscured zones  $Z_o(T-t)$  for a nucleation at time  $t$  and with density  $1/\lambda_t \times [d\lambda_t/dt]$ . The mean obscuration zone can then be expressed as

$$\lambda_t(T)M(T) = \int_0^T \frac{d\lambda_t}{dt}(t)Z_o(T-t)dt \quad (5)$$

so that

$$P_o(T) = 1 - \exp[-\lambda_t(T)M(T)] \quad (6)$$

Equation (6) is the result obtained for the *Boolean islands* model within the framework of the Boolean random functions [8,9] and is an extension of a Weibull law (Eq. (1)) that can be recovered for very low stress rates.

Usually, the obscuration zone cannot be assumed as a time-constant variable and since no analytical expressions are available for  $Z_o(T-t)$ , an approximation will be proposed. The shape of the interaction zone is supposed to be constant, i.e., all the interaction zones are self-similar [10,11] and  $Z_o(T-t)$  can be written as

$$Z_o(T-t) = S[kC(T-t)]^p \quad (7)$$

where  $S$  is a shape parameter,  $k \in ]0,1[$  is a constant,  $C$  the longitudinal stress wave velocity so that  $kC(T-t)$  is a representative length of the relaxation around a broken flaw.

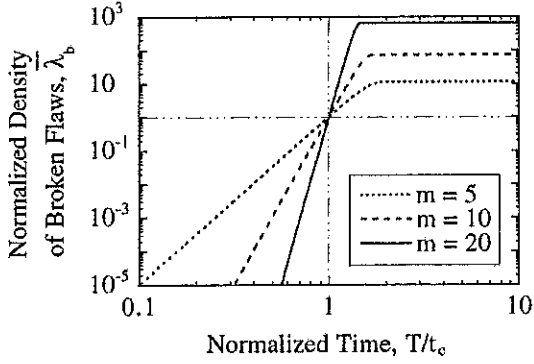


Figure 7. Normalized density of broken flaws vs. normalized time for three different Weibull moduli  $m$ .

When dynamic loadings are considered with a constant stress rate  $\dot{\sigma}$  one can define a dimensionless flaw density ( $\lambda = \lambda / \lambda_c$ ), time ( $\bar{T} = T / t_c$ ), space measure ( $\bar{Z} = Z / Z_c$ ) and stress ( $\bar{\sigma} = \sigma / \sigma_c$ ) from the condition

$$\lambda_c Z_c = 1 \text{ with } \lambda_c = \lambda_c(t_c) \text{ and } Z_c = Z_o(t_c) \quad (8)$$

$$t_c = \left[ \frac{S_0^m}{\lambda_0 \dot{\sigma}^m S(kC)^n} \right]^{1/m+n}, Z_c = \left[ \frac{S_0(kC) S^{1/n}}{\lambda_0^{1/m} \dot{\sigma}} \right]^{mm/m+n}$$

where the subscript  $c$  denotes characteristic quantities. A characteristic stress can be defined by  $\sigma_c = \dot{\sigma} t_c$ . Equation (8) expresses the fact that the characteristic zone of measure  $Z_c$  contains a unique flaw that may break at the characteristic time  $t_c$ .

By using Eqs. (1), (4) and (7) an analytical solution is given for the differential equation (3) in the case of a constant stress rate  $\dot{\sigma}$

$$\bar{\lambda}_b(\bar{T}) = \frac{m}{m+n} \frac{(m+n)!}{m!n!} \gamma \left[ \frac{m}{m+n}, \frac{m!n!\bar{T}^{m+n}}{(m+n)!} \right] \quad (9)$$

where  $\gamma$  is the incomplete gamma function. Figure 7 shows the saturation phenomenon as the considered time becomes greater than the characteristic time. The density of broken flaws at saturation  $\lambda_b(\infty)$  can be derived from Eq. (9) and is only dependent on the Weibull modulus  $m$  and the space dimension  $n$  when normalized by  $\lambda_c$ .

Figure 8 shows an increase of the number of broken flaws at saturation with the Weibull modulus  $m$ . An explanation to this phenomenon can be proposed by using Eq. (3). With a high Weibull modulus  $m$ , the density of defects will increase sharply in a small time step when the time  $T$  becomes greater than  $t_c$ . Because of the time dependence of the saturation mechanism, many defects nucleate before any significant saturation and the material will be fully fragmented. If  $m$  is small, there is much more time between two crack initiations.

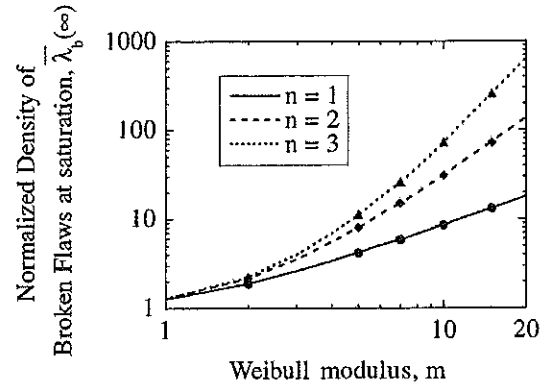


Figure 8. Normalized density of broken flaws at saturation vs. Weibull modulus for different values of the space dimension  $n$ . The solid symbols show results obtained by Monte-Carlo simulations.

The first nucleated defects can then obscure others before their own nucleation and only few defects eventually nucleate. Lastly, the error between Monte-Carlo simulations (500 realizations per computation) for a zone of measure  $\bar{Z} = 100$  and the solution at saturation given in Eq. (9) is less than 0.5% (Fig. 8). It can be noted that for each numerical simulation the set of random numbers is characterized by an integer called the 'seed' of the random generator [12]. A given probabilistic simulation is then defined by this integer and can always be reproduced by using the same 'seed'.

### 3. DAMAGE KINETIC LAW

The variable  $P_o$  can be used to define a damage variable in the framework of Continuum Damage Mechanics, even if  $P_o$  describes a non-homogeneous stress-field due to the randomness of fragmentation. By averaging over a representative zone (to be specified later on),  $P_o$  is equal to the damage variable  $D$ , with  $D = 0$  for the virgin material and  $D = 1$  for the fully broken one. It is interesting to notice that the first order approximation of Eq. (4) leads to the differential equation proposed by Grady and Kipp [13] to describe the evolution of a damage variable. By using Eqs. (4) and (7), the kinetic law of the damage variable  $D$  can be written as

$$\frac{d^{n-1}}{dt^{n-1}} \left( \frac{1}{1-D} \frac{dD}{dt} \right) = \lambda_t [\sigma(t)] n! S(kC)^n \quad (10)$$

An expression for the damage parameter  $D$  can be derived by integrating Eq. (10) for a constant stress rate  $\dot{\sigma}$

$$D = 1 - \exp \left[ - \frac{m!n!\bar{T}^{m+n}}{(m+n)!} \right] \quad (11)$$

Equation (11) shows that  $D(\bar{T} = 1) \approx 0$  and  $D(\bar{T} = 2) \approx 1$  (i.e., most of the damage evolution occurs during a time interval equal to the characteristic time  $t_c$ . During  $t_c$ , the measure of the horizon is limited by  $Z_c$  so that the *minimum*

measure of the representative zone is  $Z_c$ . By noting that the applied stress  $\Sigma$  is related to the local (or effective) stress  $\sigma$  by  $\sigma = \Sigma/(1-D)$ , the ultimate strength ( $d\Sigma/d\sigma = 0$ ) is denoted by  $\Sigma_{\max}$  and is expressed as

$$\frac{\Sigma_{\max}}{\sigma_c} = \left[ \frac{(m+n-1)!}{e m! n!} \right]^{1/m+n} \quad (12)$$

It is worth noting that the normalized ultimate strength only depends upon the Weibull parameter  $m$  and the space dimension  $n$ . The ultimate strength  $\Sigma_{\max}$  is then proportional to  $\sigma^{n/(m+n)}$ .

#### 4. FRAGMENTATION TRANSITION

In the previous sections, different failure regimes were observed. Under quasi-static loading conditions, a weakest link hypothesis is made. It follows that the first fracture event leads to the complete failure of a structure made of brittle materials. Conversely, under dynamic loading conditions, multiple fragmentation is observed and a damage model can be derived. The aim of the present section is to exhibit the conditions of applications of the previous results.

Figure 9 shows the change of the ultimate tensile strength with the stress rate for a volume  $V$  equal to  $V_{\text{eff}}$  ( $n=3$ ). The lines represent analytical solutions while the dots and error bars are Monte-Carlo simulations (500 realizations per point). For a stress rate within  $[0, 5 \cdot 10^{14} \text{ Pa/s}]$ , the ultimate strength is not modified by the loading rate and follows a classical Weibull model

$$\sigma_W = S_0 (V_{\text{eff}} \lambda_0)^{-1/m} \Gamma \left( \frac{m+1}{m} \right) \quad (13)$$

$$\sigma_{sd}^2 = S_0^2 (V_{\text{eff}} \lambda_0)^{-2/m} \Gamma \left( \frac{m+2}{m} \right) - \sigma_W^2$$

where  $\sigma_W$  denotes the average failure stress,  $\sigma_{sd}$  the corresponding standard deviation and  $\Gamma$  the Euler (gamma) function of the second kind.

When  $\dot{\sigma}$  increases by approximately one order of magnitude, the ultimate strength follows the analytical solution (12). During the transition, the difference between the solid lines given by Eqs. (12) and (13) and simulations does not exceed 10%. The standard deviation significantly decreases in the multiple fragmentation regime. Even if the ultimate strength has to be defined for static and dynamic loadings by a mean and a standard deviation, one can see that dynamic loadings lead to a more 'deterministic' behavior. For a SiC ceramic, a stress rate up to  $10^{13} \text{ Pa/s}$  has shown no stress effect on the mean failure stress [14]. This observation is in good agreement with the result shown in Fig. 9.

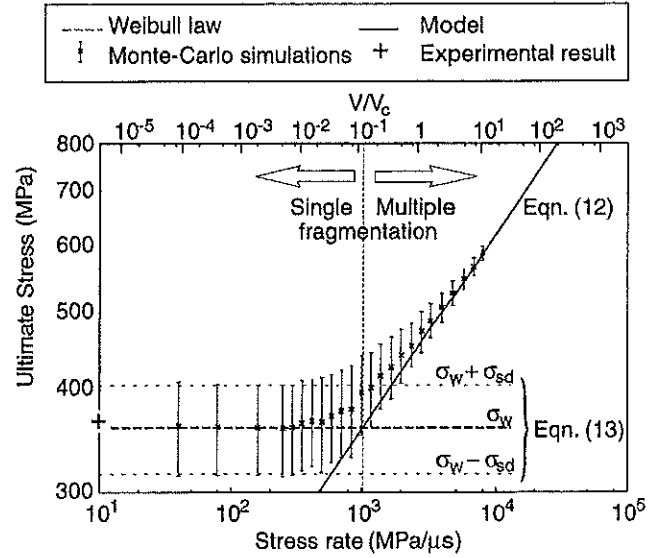


Figure 9. Ultimate tensile strength vs. stress rate for a SiC ceramic. Cross (average) and bars (standard deviates) are given by the Monte-Carlo simulations (500 realizations for each points). The considered volume ( $n=3$ ) is  $V=V_{\text{eff}}$ .

The transition between single and multiple fragmentation can be estimated by the following condition

$$\sigma_W = \Sigma_{\max}(\dot{\sigma}) \quad (14)$$

The transition between quasi-static and dynamic descriptions defined by Eq. (14) leads to the following inequalities

$$\begin{cases} \dot{\sigma} Z^{m+n/mn} < f & \text{single fragmentation} \\ \dot{\sigma} Z^{m+n/mn} \geq f & \text{multiple fragmentation} \end{cases} \quad (15)$$

with

$$f = \lambda_0^{-1/m} S_0 S^{1/n} kC \left[ \frac{e n! m!}{(m+n-1)!} \Gamma \left( \frac{m+1}{m} \right)^{m+n} \right]^{1/n} \quad (16)$$

This transition does not only depend on material parameters but also involves the measure  $Z$  of the considered element. The response of a large structure can be considered as 'dynamic' for low stress rates even if the material follows a weakest link hypothesis for the same loading applied on a smaller volume. There is therefore no relationship between material parameters and characteristic scales to describe the degradation of brittle materials.

This transition can also be expressed by using the characteristic measure  $Z_c(\dot{\sigma})$

$$\begin{cases} Z/Z_c < g(m) & \text{single fragmentation} \\ Z/Z_c \geq g(m) & \text{multiple fragmentation} \end{cases} \quad (17)$$

with

$$g(m) = \left[ e \frac{n! m!}{(m+n-1)!} \right]^{m/m+n} \Gamma \left( \frac{m+1}{m} \right)^m \quad (18)$$

The characteristic space measure  $Z_c(\dot{\sigma})$  can therefore be considered as the characteristic scale for which a single/multiple fragmentation occurs. Furthermore, Fig. 9 shows that for  $Z/Z_c(\dot{\sigma}) \geq 1$ , the ultimate strength scatter is very small. This characteristic volume can be used in FE computations in which the mesh size has to be greater than  $Z_c(\dot{\sigma})$  to use a continuum description of damage.

### 5. MULTI-SCALE DAMAGE MODEL

For each principle stress direction  $d_i$ , a anisotropic damage variable  $D_i$  is defined [7] so that the principle strains  $\varepsilon_i$  are related to the principal stresses  $\sigma_i$  by:

$$\varepsilon_i = \mathbf{K}_{ij}(D_1, D_2, D_3) \sigma_j \quad (19)$$

where the usual index summation is used. The compliance tensor  $\mathbf{K}$  is defined by

$$\mathbf{K} = \frac{1}{E} \begin{bmatrix} \frac{1}{1-D_1} & -\nu & -\nu \\ -\nu & \frac{1}{1-D_2} & -\nu \\ -\nu & -\nu & \frac{1}{1-D_3} \end{bmatrix} \quad (20)$$

where  $E$  is the Young's modulus and  $\nu$  the Poisson's ratio of the undamaged material.

In 3D configurations, the kinetic law for  $D_i$  is expressed in a differential form (see Eq. (10))

$$\frac{d^2}{dt^2} \left( \frac{1}{1-D_i} \frac{dD_i}{dt} \right) = 6\tilde{\lambda}_i(\sigma_i) S(kC)^3 \quad (21)$$

when  $\sigma_i > 0$  and  $\dot{\sigma}_i > 0$ . The defect density  $\tilde{\lambda}_i$  associated with the Weibull model is defined such that the damage model is used only if at least one defect is broken in the considered finite element  $\Omega_{FE}$  of volume  $V_{FE}$

$$V_{FE} \tilde{\lambda}_i(\sigma_i) = \begin{cases} 0 & \text{if } \sigma_i < \sigma_k \\ \max \left[ V_{FE} \lambda_0 \left( \frac{\sigma_i}{\sigma_0} \right)^m, 1 \right] & \text{otherwise} \end{cases} \quad (22)$$

where  $\sigma_k$  a random failure stress obeying the Weibull law (1). For low stress rates, the first defect breaks and relaxes the stresses in  $\Omega_{FE}$ . It follows that the quasi-static Weibull properties (Eq. (13)) are recovered. For a high (tensile) stress rate, the zone relaxed by the first defect to break has a weak influence and a deterministic (damage) approach applies.

The behavior of a FE cell is therefore not deterministic and numerous calculations have to be performed when average values are awaited (e.g., average macroscopic ultimate stress  $\Sigma_{\max}(\dot{\sigma})$ ). Such calculations are shown in Fig. 10 for a volume where the macroscopic ultimate stress

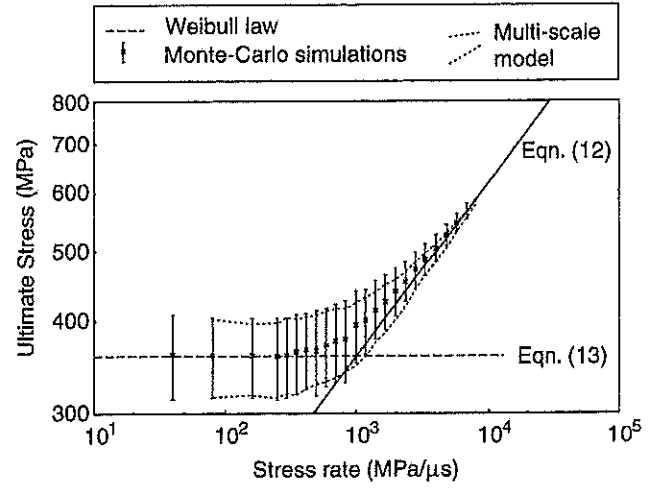


Figure 10. Ultimate macroscopic stress vs. stress rate for the multi-scale model and the Monte-Carlo simulations (500 realizations for each points) for a SiC ceramic.

vs. stress rate is plotted. The results obtained with the multi-scale model is comparable (in terms of mean and standard deviation) to those given by the Monte-Carlo simulations with a CPU time divided by 3000.

Once the elastic properties and the Weibull parameters are known, the model discussed herein has no other parameters to tune. In the following, a special emphasis will be put on silicon carbide ceramics.

### 6. COMPARISON WITH EXPERIMENTS

Tensile cracking, one of the major degradation mechanisms during interaction, can be observed during impact by using so-called Edge-On Impact (EOI) configurations instead of a real configuration where the degradation is 'hidden' in the bulk of the ceramic (Fig. 11). These configurations are developed by the Ernst-Mach-Institut (EMI) in Germany [15,16] and more recently by the Centre Technique d'Arcueil (CTA) in France [6]. It can be

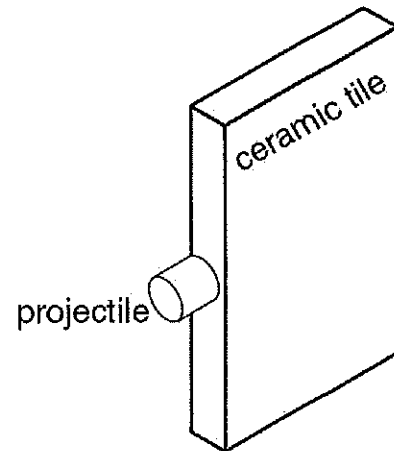


Figure 11. Schematic of an edge-on impact configuration.

shown that the same damage mechanism (i.e., damage in tension) is observed in EOI and in real impact configurations [17]. The EOI configuration can therefore be used to validate the damage description and kinetic law for numerical simulations of the behavior of light armors made of ceramics (front plate) and steels (backing).

### 6.1. Continuum vs. discrete approaches

The characteristic quantities, utilized to determine whether continuum or discrete approaches apply, can be used only when the remote strains are uniform over the considered volume element. The probabilistic nature of damage implies that conventional approaches [7] may not be applicable for impacted volumes where the strain rate can strongly vary over the structure due to dilution (i.e., divergent stress wave), reflection (e.g., spalling). The validity of the numerical simulations can be checked by plotting for each integration point the maximum stress rate. Figure 12-a (top) shows the stress rate  $4\mu\text{s}$  after impact with corresponding damaged zone (bottom). When damage is generated, the stress rate is about  $10^3\text{MPa}/\mu\text{s}$ . One can see in Fig. 12 that this loading cannot be modeled accurately by using either continuum or discrete approaches, i.e., more than one defect breaks but the material cannot be considered as continuum in a FE cell. The criterion proposed in Eq. (17) also confirms that the FE cell is too small for a continuum model but not large enough for a discrete approach ( $V_{FE}/V_c(\dot{\sigma}) \approx g(m)$  for  $V_{FE} = 1\text{mm}^3$ ).

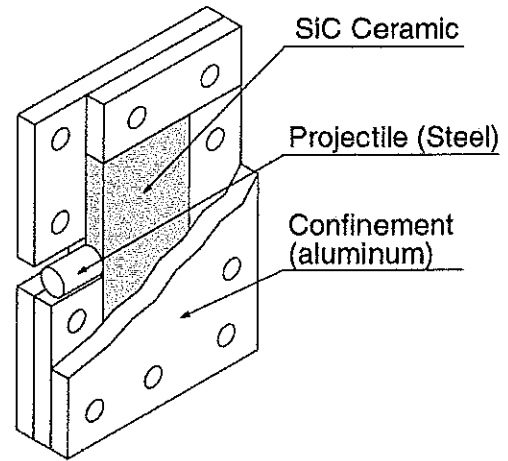


Figure 13. Schematic of the 'sarcophagus' configuration. The tile is confined between two 10mm thick aluminum plates. The edge confinement is obtained by aluminum tiles screwed on the plates.

In the following, the capability of the multi-scale model is evaluated to reproduce observed degradation patterns.

### 6.2. Sarcophagus

A configuration dedicated to post-mortem analyses (called sarcophagus) is shown in Fig. 13. In this configuration, a blunt projectile (11mm in diameter and 20mm in length) impacts at 330m/s a ceramic tile of size  $100 \times 50 \times 10\text{mm}^3$ . After impact, the tile is coated in an epoxy resin and polished for macroscopic and microscopic analyses.

The post-mortem crack pattern is shown in Fig. 14. Different zones can be separated with respect to crack density and orientation. In front of the projectile, a small zone exhibits a randomly oriented crack pattern. In the bulk of the ceramic, one can observe long radial cracks with a second circumferential crack pattern superimposed on the first one. In this last region, some radial cracks seem to kink in the circumferential direction, kink one more time and propagate in the radial direction. The kinked fractures are made of two small cracks linked by a small circumferential crack. This complex crack pattern is then opened by the radial motion of the ceramic, widens and becomes a long macroscopic 'kinked' fracture. This phenomenon shows that the radial cracks appear prior to the circumferential ones, since the latter do not cross the former. Near the tile rear face, a third zone exhibits a high density of cracks. This thin strip remains at a constant distance from the rear surface, like a spalling zone. It is worth mentioning that the cracks remain in the radial and circumferential directions even though this zone is parallel to the rear surface. A numerical prediction is given in Fig. 14. The cracking mechanism can be described as the superposition of a radially and a circumferentially oriented crack patterns, the former with a higher density than the latter. The radially oriented crack pattern is generated during the first microseconds of impact. It is followed by the circumferential ones due to the relaxation wave emanating from the projectile and the rear

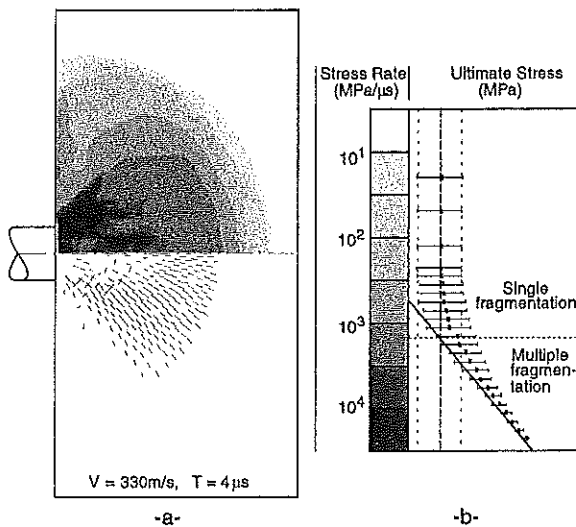


Figure 12. Requirements to be fulfilled to use a continuum description can be checked by using a maximum stress rate map.

a-Example of maximum stress rate for the first (tensile) eigen stress  $4\mu\text{s}$  after impact (top) and the corresponding damaged zone (bottom).

b-The stress rate associated to locations where damage is generated leads to a complex behavior, neither discrete nor continuum.

face of the ceramic tile. This result is in good agreement with the experimental observations. The zone in front of the projectile in which only few radial cracks seem to have nucleated is well reproduced. Finally, the high density crack zone looking like a spalling region is also well described, with a crack direction approximately in the radial and circumferential direction, as observed in the sarcophagus configuration.

### 6.3. Real Time Visualizations

Real time visualizations of damage have been performed by using the Edge-on Impact configuration developed by the EMI [15]. The velocity of a single crack has been measured [6] and is about 4800m/s. The value of the parameter  $k$  is thus equal to 0.4, and is in accordance with classical results for crack propagation [18,19]. A remark can be drawn on the shape of the damaged zone with respect to the impact velocity. With a high impact velocity, the damage is homogeneous in a circular zone in front of the projectile (see Fig. 15-b). Below a critical value depending on the material properties, damage is localized in thinner and thinner corridors when the velocity decreases (Fig. 15-a). Even though this localization leads to larger fragments, it has been demonstrated [20] that the transition between corridors and circular shapes of damage is not related to the single/multiple fragmentation transition described in Section 4.

The simulation is performed on the EOI configuration with an impact velocity of 185m/s and 513m/s on a SiC ceramic. The random stress to failure is computed by using Eqs. (1) and (22) for a FE volume of  $1\text{mm}^3$ . For high stress rates (i.e., in front of the projectile and in the Hertz-like cone crack), many defects nucleate in a FE cell. For a velocity of 185m/s, failure of an element set, which can be compared to macroscopic cracks, can be observed in addition to the continuum degradation generated at the edge of the projectile. However, there are some difficulties in handling macroscopic cracks. The failure of a FE cell is not always followed by a crack generation and propagation, and when such a crack is created, there is a tendency to follow the direction of the FE mesh. This result may be improved by refining the mesh and the model.

The numerical simulations are in good agreement with the general shape of the damaged zone experimentally observed. In Fig. 15-a the damaged zone in front of the projectile that widens and progressively localizes in corridors is well reproduced by the simulation. The zone generated on the projectile edges that can roughly be compared to a Hertz cone crack is also found in the numerical results. This damage localization vanishes for impact velocity greater than about 350m/s [16], as one can observe in Fig. 15-b.

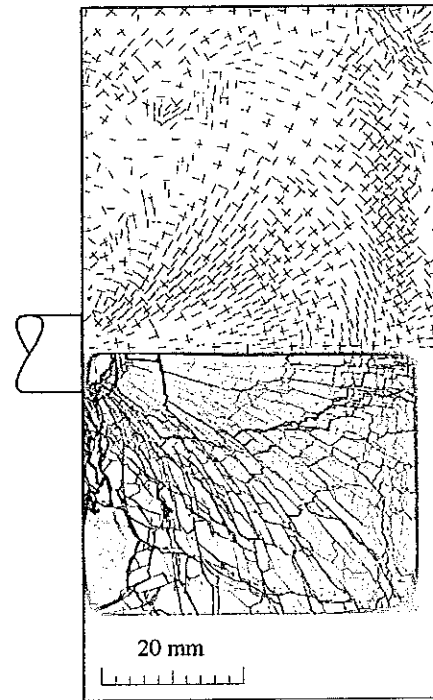


Figure 14. Damage evolution during an impact on a SiC Ceramic. The projectile velocity is 330m/s. Numerical results are given in the tile upper part where the line density is a function of broken flaws density and the line direction is that of cracking. The tile's lower part corresponds to the post-mortem crack pattern.

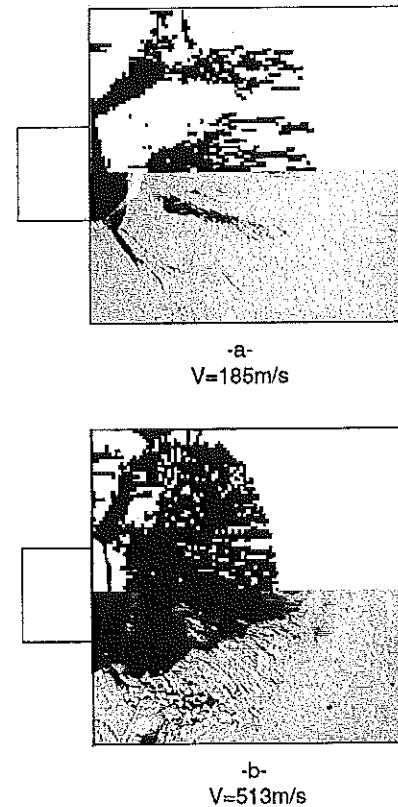


Figure 15. Numerical simulations of a SiC ceramic in an EOI configuration. Tile upper part: simulation), tile lower part: experiments. Damaged zones ( $D_1 > 0.5$  in the dark zones) for two impact velocities.

## 6.4. Moiré technique

A third EOI configuration provides quantitative strain measurements over a field of  $32 \times 32 \text{mm}^2$  during impact. Details on the moiré photography set-up can be found in Ref. [21]. The advantage of the moiré measurement is that a *quantitative* rather than qualitative analysis can be performed between experiments and simulations. The method used to analyze the fringes cannot give reliable data when they are blurred. To overcome this problem, the artifacts generated during the fringe pattern analysis are automatically reset. Figure 16-a is the fringe pattern approximately  $2 \mu\text{s}$  after impact. The comparison of numerical and experimental strains is given in Fig. 16-b. The strain diagram is plotted for a point M at a distance of 13mm from the surface hit by the projectile (circular mark in Fig. 16-a). It can be noted that the radial strain reaches an important value (of the order of 0.8%) before any significant evolution of the hoop strain. This is consistent with a cylindrical stress wave in which the tensile strain is induced by the radial motion of the material.

The multi-scale model is used to yield probabilistic results. Therefore, numerous simulations have to be performed when the *average* behavior is analyzed. Five hundred realizations of the simulation are now presented. A CPU time of 4 minutes per realization is needed on an HP 715 workstation with the finite element package PamShock [22]. The average and the standard deviate of the hoop and radial strains are plotted in Fig. 16-b. There is a good agreement between the measured and predicted average strains. All the experimental measurements fall in the grey shaded zone, i.e., the experiment may be compared to *one* realization of the 500 numerical simulations.

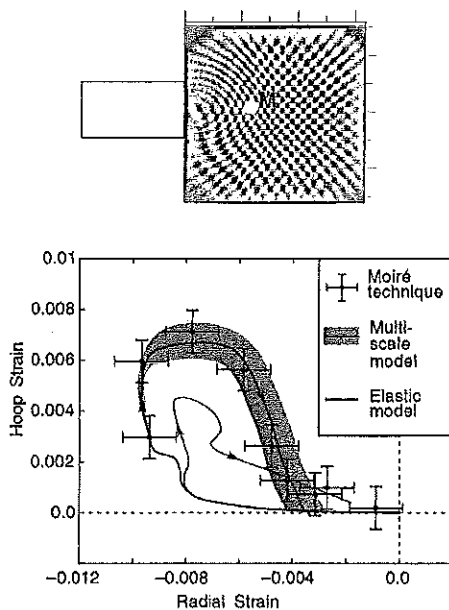


Figure 16. a-Typical example of moiré fringes.  
b-Strain evolution given by a moiré technique (dots) and by the multi-scale model (plain curve: average, grey bandwidth:  $\pm$  standard deviate).

## 7. CONCLUSIONS

A fragmentation model based on a mechanism of nucleation of flaws and stress relaxation is proposed. When a constant stress rate is applied, a closed-form solution for the number of nucleated defects is given. The characteristic time and space scales are defined and are useful for checking the relevance of FE simulations. A Monte-Carlo simulation is used to analyze the transition between single and multiple fragmentation. This transition does not coincide with that between quasi-static and dynamic loading (e.g., one may have a single crack during a dynamic loading if the considered volume is sufficiently small). This transition condition is expressed as a function of the Weibull modulus and a characteristic volume, surface or length.

A damage kinetic law is derived from the fragmentation model, which is probabilistic by construction. The analysis of stress relaxation around the propagating cracks leads naturally to an anisotropic description of damage. A differential form is derived for the kinetics of damage variables in order to be implemented in a FE code. A multi-scale model is defined by describing the broken flaws by a continuum density in addition to the first defect able to break. The probabilistic nature of this model helps in understanding the probabilistic behavior of structures made of brittle materials and submitted to a wide range of loadings (from quasi-static to dynamic ones). This model is therefore different from a continuum and deterministic description of damage that is usually used [7].

A good approximation of the kinetics of the damaged zones in EOI configurations are given by the model in terms of degradation patterns (e.g., sarcophagus configuration) or strain evolution (e.g., comparison with the moiré measurements). Since all the parameters are determined by analytical analyses or identified through quasi-static (independent) tests, the multi-scale model can be considered as fully *predictive*. The strain evolution during impact is also predicted, in particular when the material seems to be intensively damaged.

The multi-scale model may be used to understand whether the probabilistic nature of the ceramic behavior can modify that of the structure. It has been demonstrated that the model is able to reproduce the behavior of a unit volume, from quasi-static loadings where the failure is due to a single defect to dynamic loadings where many flaws nucleate. For low impact velocities, the degradation pattern is well reproduced by the multi-scale model and both diffuse damage and isolated cracks are generated. One can observe that the mechanism of crack propagation at the macroscopic level may not be exact because of the coarse description of the stress field at the macrocrack tip. Refining the mesh may improve the simulation of isolated cracks.

The transition zone for which the number of nucleated flaws is greater but nevertheless close to one in a FE cell is well reproduced by the multi-scale model. The corresponding

behavior, neither continuum nor discrete is one of the major features of this model. Lastly, it is expected that the model is applicable to other brittle materials (such as rock, glass or concrete). Since the numbers of parameters to identify is very limited and can be carried out under quasi-static loading conditions, the model can be tested on a wide class of brittle materials.

## 8. ACKNOWLEDGMENTS

This work was funded by DGA-DRET-STRDT and supervised by Dr. C.E. Cottenot at CTA. The authors wish to thank Dr. E. Strassburger and Dr. H. Senf for providing the experimental data of Fig. 15. The authors wish also to thank A. Trameçon from ESI for his valuable help in implementing the model in PamShock.

## 9. REFERENCES

1. A. M. Freudenthal, in H. Liebowitz (ed.), *Statistical Approach to Brittle Fracture*, vol. 2, Academic Press, New York, NY (USA), pp. 591-619, 1968.
2. W. Weibull, *A Statistical Theory of the Strength of Materials*, 151, Roy. Swed. Inst. Eng. Res., 1939.
3. D. G. S. Davies, *The Statistical Approach to Engineering Design in Ceramics*, *Proc. Brit. Ceram. Soc.*, vol. 22, pp. 429-452, 1973.
4. R. Gulino and S. L. Phoenix, Weibull Strength Statistics for Graphite Fibres Measured from the Break Progression in a Model Graphite/Glass/Epoxy Microcomposite, *J. Mater. Sci.*, vol. 26, pp. 3107-3118, 1991.
5. D. Jeulin, *Modèles morphologiques de structures aléatoires et changement d'échelle*, thèse d'État, University of Caen, 1991 (in French).
6. P. Riou, C. Denoual and C. E. Cottenot, Visualization of the Damage Evolution in Impacted Ceramic Carbide Ceramics, *Int. J. Impact Eng.*, vol. 21, pp. 225-235, 1998.
7. J. Lemaitre, *A Course on Damage Mechanics*, Springer, Berlin (Germany). See also J. Lemaitre and J.-L. Chaboche, *Mechanics of Solid Materials*, Cambridge University Press, Cambridge (UK).
8. D. Jeulin and P. Jeulin, *Proc. 3rd European Symposium of Stereology*, pp. 239-246, 1981.
9. J. Serra, *Image Analysis and Mathematical Morphology*, Academic Press, London (UK), 1982.
10. J. I. Bluhm, in H. Liebowitz (ed.), *Fracture Arrest*, vol. 5, Academic Press, New York, NY (USA), pp. 1-63, 1968.
11. L. B. Freund, Crack Propagation in an Elastic Solid Subjected to General Loading - Constant Rate of Extension, *J. Mech. Phys. Solids*, vol. 20, pp. 129-140, 1972.
12. W. H. Press, S. A. Teukolsky, W. T. Vetterling and B. P. Flannery, *Numerical Recipes in Fortran*, Cambridge University Press, Cambridge (USA), 1992.
13. D. E. Grady and M. E. Kipp, Continuum Modeling of Explosive Fracture in Oil Shale, *Int. J. Rock Min. Sci. Geomech.*, vol. 17, pp. 147-157, 1980.
14. C. Denoual and P. Riou, *Comportement à l'impact de céramiques techniques pour blindages légers*, 95 R 005, CREA, 1995 (in French).
15. E. Strassburger, H. Senf and H. Rothenhausler, Fracture Propagation during Impact in Three Types of Ceramics, *J. Physique IV*, vol. C8, pp. 653-658, 1994.
16. E. Strassburger and H. Senf, Experimental Investigations of Wave and Fracture Phenomena in Impacted Ceramics and Glasses, ARL-CR-214, ARL, 1995.
17. C. Denoual, C. E. Cottenot and F. Hild, *Proc. 16th International Conference on BALLISTICS*, APDS, Arlington, VA (USA), pp. 541-550, 1996.
18. M. F. Kanninen and C. H. Popelar, *Advanced Fracture Mechanics*, Oxford University Press, New York, NY (USA), 1985.
19. L. B. Freund, *Dynamic Fracture Mechanics*, Cambridge University Press, Cambridge (UK), 1990.
20. C. Denoual and F. Hild, On the Characteristic Scales involved in a Fragmentation Process, *J. Phys.*, vol. IV, pp. 119-126, 1998. See also C. Denoual and F. Hild, A Damage Model for the Dynamic Fragmentation of Brittle Solids, *Comp. Meth. Appl. Mech. Engrg.*, vol. 183, pp. 247-258, 2000.
21. T. Bertin-Mouro, C. Denoual, G. Dehors, P.-F. Louvigné and T. Thomas, High Speed Photography of Moiré Fringes - Application to Ceramics under Impact, *J. Physique IV*, vol. C3, pp. 311-316, 1997.
22. PamShock, User's Manual, ESI, 1996.

# Behavior and fracture of Mg based composite materials undergoing a compressive loading

*Lichtenberger A., Lach E., Bohmann A., Scharf M.*

ISL, French-German Research Institute of Saint-Louis, F-68301 SAINT-LOUIS

## Abstract:

The aim of this work is to study the behavior of short-fiber and particle-reinforced magnesium alloys under quasi-static and dynamic loading (Hopkinson bar). Particularly magnesium alloys, QE22 and AZ91 were used as matrix materials. Reinforcing materials were 20% short-fiber- $\text{Al}_2\text{O}_3$  (Saffil<sup>®</sup>) and 15% SiC-particles combined with 7.5% Saffil<sup>®</sup> (mixed). Composites were produced by squeeze casting.

Static tension tests show that the reinforcement of the magnesium alloy leads to a very brittle behavior without any improvement in the mechanical resistance of the material. Tension and compression tests reveal a fully different behavior resulting in a high value of yield stresses and strain to rupture.

A solution annealing treatment on the QE22 based materials do not change the mean properties of dynamic compression, but reduces significantly the scattering of the results. In compression the reinforcement of the magnesium alloy increases the yield stress about 50% with a more rapid failure.

The influence of the geometry of the compression specimens on the stress-strain curves and on the maximal strain to rupture was investigated.

Fractures were investigated by means of a scanning electron microscope and confirm the brittle behavior of the composite. A metallographic study of microstructure was also performed.

## **1.Introduction**

Light materials with good mechanical properties are today widely studied and are a new challenge for applications in various fields. The aerospace, motor and military industries have a big interest in the development of new materials such as metal matrix composites. Due to the promising results reported during the development of these alloys, research has been concentrated on reinforcing the light metal magnesium and its alloys with alumina fibers. Magnesium and its alloys are the engineering materials with the lowest density. The strengthening of magnesium alloys is undertaken to improve critical properties such as elastic modulus, high-temperature strength, wear resistance and thermal expansion.

Considerations about the use of magnesium alloys for body parts show that it is necessary to get information on the deformation behavior under static and dynamic loading. The requirement to absorb energy in a crash situation or in the penetration of a projectile needs some ductility.

The low-rate mechanical properties and failure mechanisms of reinforced Mg-alloys have been well-characterized [1]. The influence of particle volume fraction and shape on the behavior of metal-matrix composites at high strain rates was studied in [2]. The impact behavior of magnesium matrix composites have been presented in [3]

This work concerns mainly with the study of the strain to failure of Mg-based composites in dynamic compression tests by different specimens geometry and the influence of a heat treatment on the dynamic compression behavior of the QE22 based materials.

Dynamic compression tests were performed on a split-Hopkinson-pressure-bar. The diameter and the length of the bars were 20 mm and 1200 mm, respectively. The bars are made on high strength steel and a stop ring has usually been used in order to allow some post observations on the damage and rupture of the specimens. The specimens were machined in the perpendicular direction of the plates with 8 to 16 mm diameters and 4 to 16 mm lengths.

## 2. Materials

Two magnesium alloys, AZ91, and QE22, have been chosen as matrix materials. Table 1 shows their chemical compositions. WE54 and QE22 are high-temperature alloys. The mechanical properties obtained by tensile test can be seen in table 2.

**Table 1:** Chemical composition of Mg-alloys in %

	Al	Zn	Mn	Zr	Ag	Nd rich R.E.	Balance
AZ91	9	0.7	0.2	0	0	0	Mg
QE22	0	0	0	0.6	2.5	2	Mg

**Table 2:** Mechanical properties of unreinforced Mg-alloys obtained by tensile test

	R <sub>p0.2</sub> (Mpa)	R <sub>m</sub> (Mpa)	A (%)	E (Gpa)	ρ (g/cm <sup>3</sup> )
AZ91	170	270	4.4	43	1.8
QE22	205	266	4	45	1.82

The strengthening of Magnesium alloys with fiber leads to an improvement in the properties. The preferred fiber material is Saffil<sup>®</sup> from ICI as, in addition to having the required properties, it is relatively cheap. Saffil consists of δ-Al<sub>2</sub>O<sub>3</sub> and has a tensile strength of 2000 MPa, a Young's modulus of 300 GPa, a Mohs hardness of 7 and has a diameter of 3 μm x 60 μm [4].

SiC particles have been mixed to the saffil to realize the Mg based composite. The diameter of SiC-particles (Mohs hardness 9.7) was 6.2 μm.

A preform for the mixed Mg-composite consists of 7.5% Saffil and 15% SiC-particles. The fibers are randomly oriented in a plane.

With this hybrid technique it is possible to produce isotropic particle-reinforced magnesium composites [6].

### 3. Behavior of reinforced QE22 in static tension tests

Static tension tests have been conducted on the reinforced magnesium alloy QE22. Results are shown in the figure 1. The 0.2% offset stress and the ultimate tensile strength ( $R_{0.2}$  and  $R_m$ ) are very similar to those of the unreinforced alloy (see Table 2). No necking can be seen and the elongation to failure do not exceed 1%.

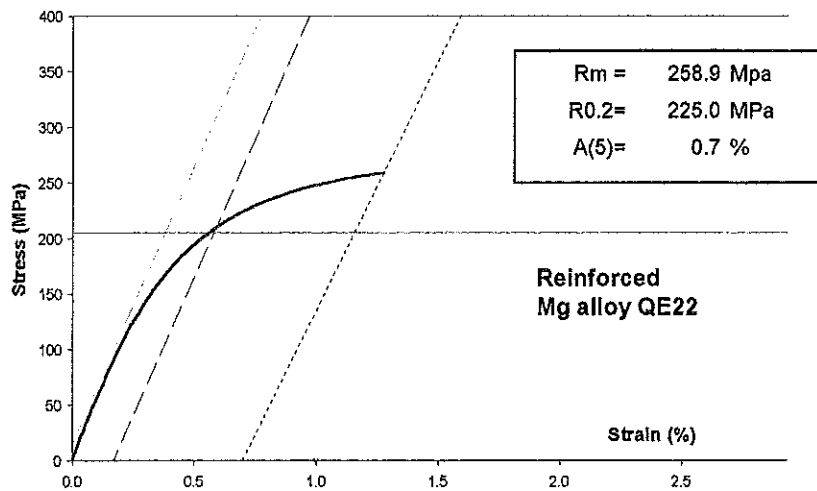


Fig.1 : Static tension test on reinforced QE22 Mg alloy

This behavior is typical for a brittle material. However, the properties under compressive loading are fully different as will be shown by the following results.

### 4. Influence of the solution annealing of the QE22 based materials on the dynamic behavior in compression

A heat treatment has been performed on the unreinforced and reinforced QE22 Mg alloy.

This treatment consists of a solution annealing at 412 °C for 8 hours. It allows a better homogenization of the materials. The effect of this treatment on the dynamical compressive behavior of the materials was examined.

Results of the SHPB compression tests are shown in the figures 2 and 3. The annealing do not influence both, the yield stress and strain to

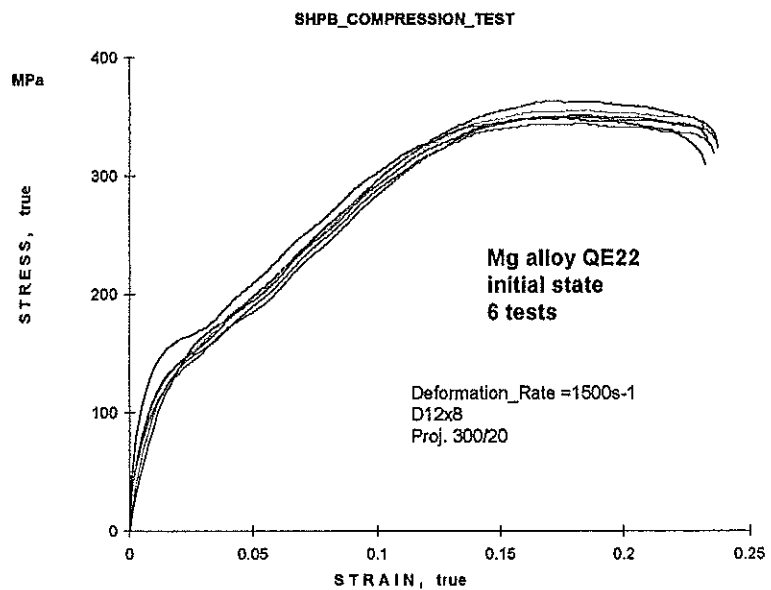


Fig.2 : Dynamic compression on QE22 without annealing

failure. The compressive stress-strain curves in figures 2 and 3 are similar and independent of the annealing treatment.

The heat treatment reduces the scattering of the compressive flow curves, which is much more important for the material in the initial state. The heat treatment leads to a better homogenization of the microstructure with the solution of some alloying elements and compounds.

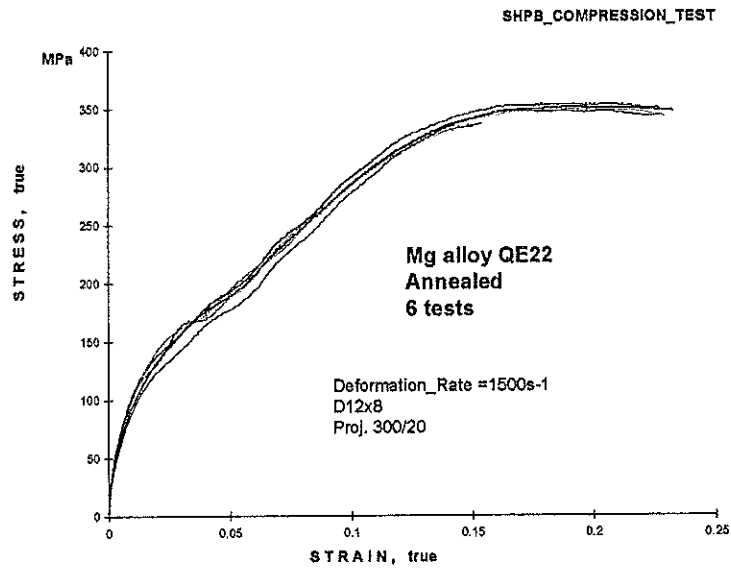


Fig.3 : Dynamic compression on QE22 annealed

Similar results can be seen in figures 4 and 5 for the reinforced QE22 magnesium alloy.

In summary, scattering is important for non annealed alloys, independent of a reinforcement. This is due to inhomogeneities in the repartition of the SiC particles and Al<sub>2</sub>O<sub>3</sub> fibers. An annealing treatment reduces significantly the scattering of the results. This is also due to the homogenization of the matrix material and probably also to a better binding with the reinforcement, particles and whiskers.

The influence of the reinforcement on the behavior of the material is important. The compression strength increases from 350 to 530 Mpa (50%) while the strain to failure is reduced from 20 to about 10% (for specimens D12x8mm). However, this is an important improvement under compressive loading compared to tensile tests.

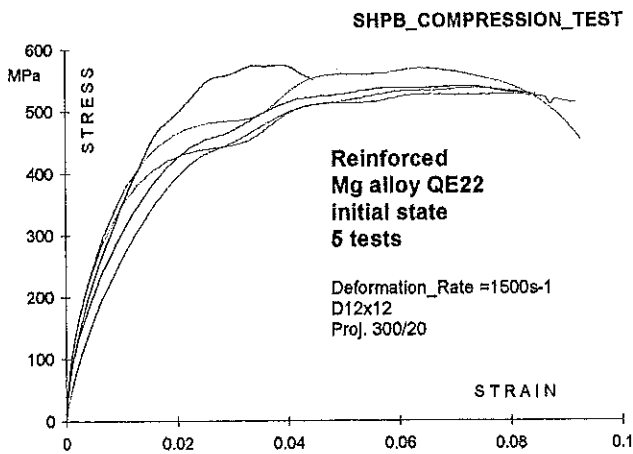


Fig.4 : Dynamic compression on reinforced QE22 without annealing

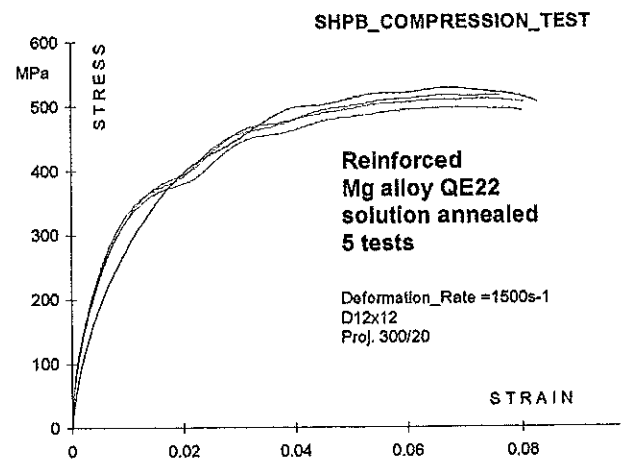


Fig.5 : Dynamic compression on reinforced QE22 annealed

## 5. Behavior of reinforced AZ91 in static and dynamic compression tests

Quasi-static and dynamic tests (at strain rates of 0.001/s and 2000/s) have been performed under compressive loading on the AZ91 composite. The diameter of the specimens was 8 mm and the length was 4 and 12 mm respectively.

Figure 6 shows the influence of the strain rate on the behavior of this material. At 3% strain, the yield stress amounts to 485 Mpa under static conditions and increased to 540 Mpa under dynamic conditions.

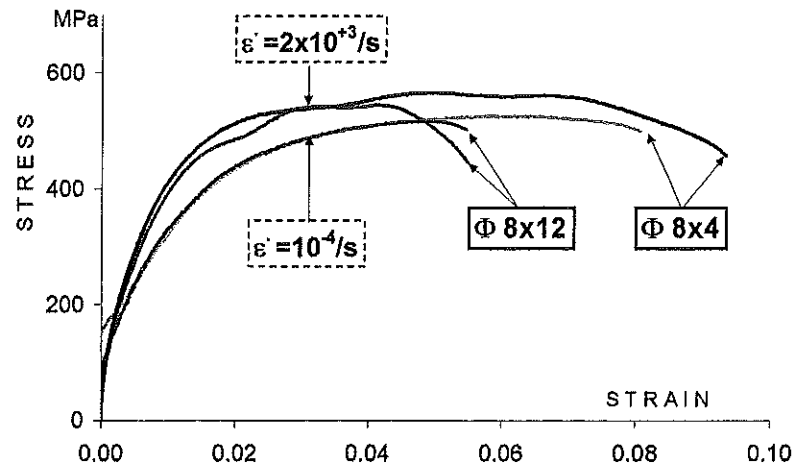


Fig.6 : Static and dynamic compression on reinforced AZ91 annealed

The strains to failure in static or dynamic conditions are very similar and depend mainly on the geometry of the specimens. About 9% strain to failure are achieved with a length to diameter ratio of 0.5 but 6% only with a ratio of 1.5.

## 6. Influence of the geometry of specimens in dynamic compression tests

Additionally dynamic compression tests have been conducted on the QE22 Mg-composite in order to confirm these results.

Specimens with 8 mm diameter and 4, 8 and 12 mm length were machined and tested in the SHPB facility. The slenderness was limited between 0.5 and 1.5, because of friction effects which could appear for smaller value and larger transient time for longer specimens, which do not allows achieving the homogeneity on both side of the specimens for small strains.

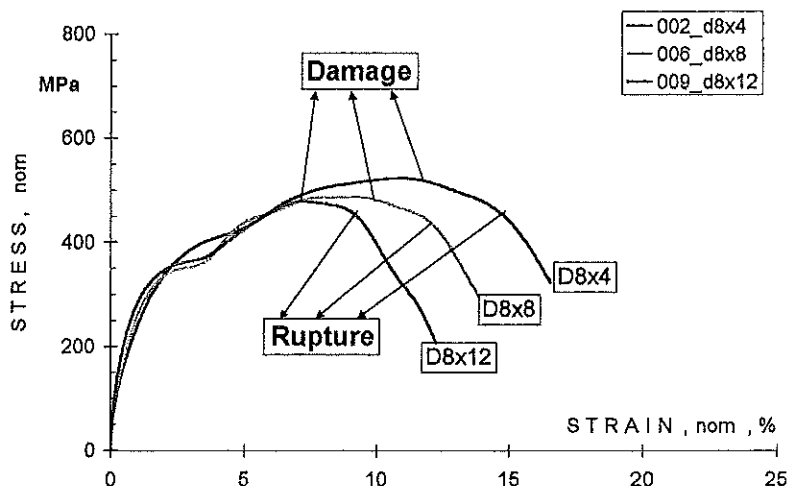


Fig.7 : Static and dynamic compression on reinforced AZ91

Figure 7 shows that the maximal strains at rupture are markedly influenced by the slenderness of the specimens. This is due to the stress concentration in the 45° directions leading to shear stresses and early failure for longer specimens, and also to the difference in the hydrostatic pressure component. The field of damage and rupture are clearly visible on the stress-strain curves. The maximal stresses just before damage are slightly increasing for smaller specimen length; this can be due to some friction effects at higher strains.

## 7. Metallographic observations

Optical micrographs (figure 8) have been made on the mixed Saffil-SiC<sub>p</sub>- QE22 composite. As a result of the manufacturing process, the fibers are randomly oriented in a plane. Infiltration of preforms is carried out predominantly perpendicular to the fibers. The microstructure of the composite is influenced by the solidification behavior of the matrix alloy. Generally, the fiber addition results in a refinement of the microstructure.

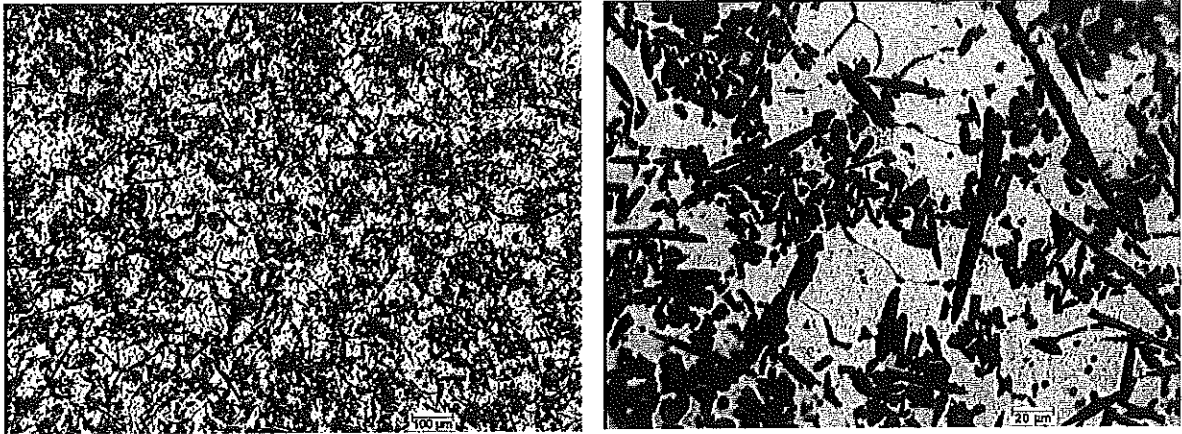


Fig. 8: Micrographs of the transverse cut in a reinforced QE22 composite

A macroscopic view of the specimen after test (figure 9) shows the difference in the fracture mode between a short and a long specimen. Short specimens give generally a unique shearing fracture in a 45° plane, whereas longer specimens leads to multiple fragments. They arise from 2 shearing planes at 45° from the edge of the specimen at the opposite side connected by a fracture plane that tends towards the axis and is subjected to a more tensile loading. Due to a higher roughness, the surface is less bright than in the pure shear plane.

These observations are in accordance with the stress-strain curves obtained in figure 7, where the damage is increasing with the length of the specimen.

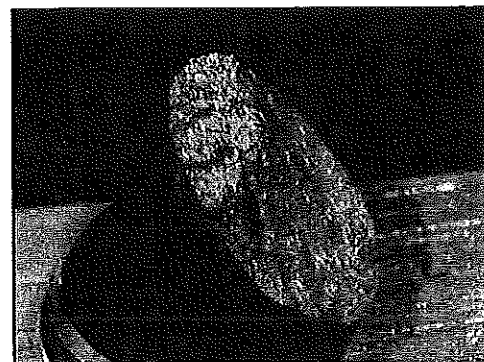
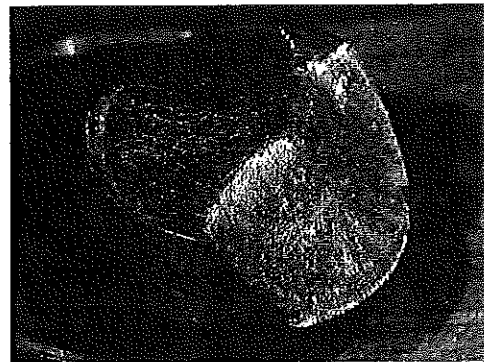


Fig. 9: Rupture surfaces of short and long specimens

The rupture surface has been investigated with Scanning Electron Microscopy. The fracture is mainly concentrated along the fibers and sometimes across them or more rarely through SiC particles. QE22 composites seem to be a little less brittle than AZ91, the matrix showing more ductility (figure 10).

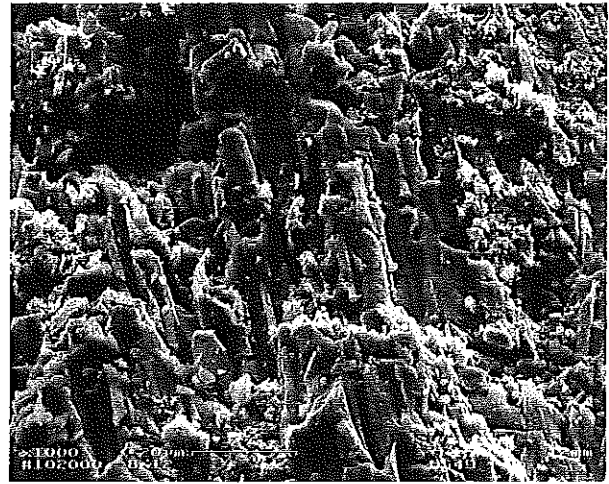
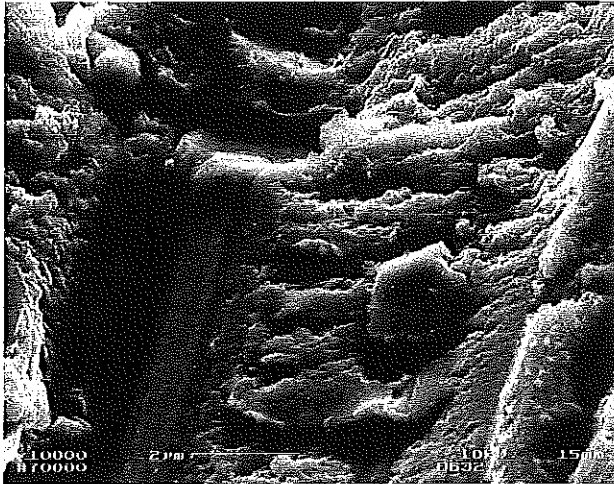


Fig. 10: Fracture surface of QE22 composite and AZ91 composite

Figure 11 shows a region of the QE22 composite which has been subjected to some tensile or flexure stresses in a ballistic target. The transverse breaking of the fibers can be observed. Tensile stress is induced in fibers by shear stress at the fiber/matrix interface during the plastic deformation of a ductile matrix. Due to this micromechanism, the high tensile strength of Saffil fibers can be used. This micromechanism mainly affects the macroscopic compression strength. Short fibers serve also as obstacles to dislocations.

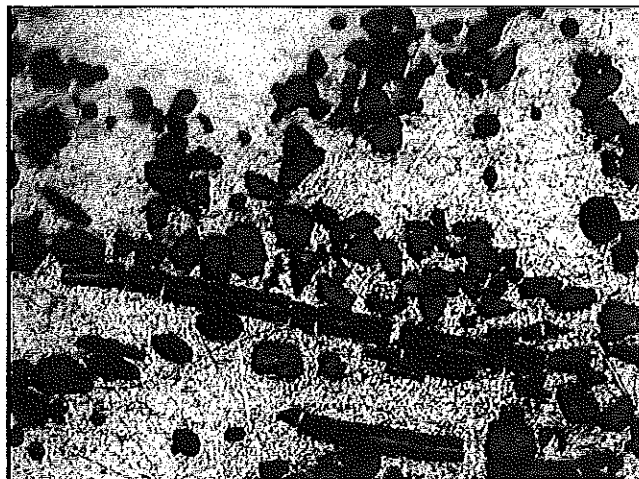


Fig. 11: Transverse breakup of a Al<sub>2</sub>O<sub>3</sub> fiber by flexure stresses.

## 8. Conclusion

Mixed Saffil-SiC<sub>p</sub>- magnesium composites are quite brittle in tension tests (<1% strain to failure), but appear much less brittle in compression.

Heat-treated QE22 magnesium alloy and the reinforced composite have identical behavior as the materials in the initial state but show significantly less scattering in the compressive flow curves. This is due to the homogenization of the matrix alloy.

In compression tests, the strain rate influences the yield stress of the QE22 composite, but not the strain to failure.

A maximal strain to failure from 5 to 18% depending on the geometry of the specimens was obtained under compression. The field of damage and the maximal strain to failure are decreasing with the slenderness of the specimens.

It can be concluded that for brittle materials tested in dynamic compression with SHPB, specimens with a small slenderness have to be preferred.

Different mode of rupture have been observed on the surface of rupture. Reinforced QE22 is more ductile than reinforced AZ91 if it is squeeze-cast. This MMC material can be an interesting candidate for components, which are exposed to a dynamic compression load as for instance in ballistic protection or projectiles sabots.

## References

1. **Kainer K. U.**, *Isotropic Properties of Mixed Saffil-SiC<sub>p</sub>-Magnesium Composites* Advanced Composites 93, Eds.: Chandra T., Dhingra A. K., The Minerals, Metals & Materials Society, **1993**, pp. 1,213-1, 219
2. **Li Y., Ramesh K. T.**, *Influence of Particle Volume Fraction, Shape, and Aspect Ratio on the Behavior of Particle-Reinforced Metal-Matrix Composites at High Rates of Strain*, Acta mater., 46 (1998), pp. 5633-5646
3. **Lach E., Kainer K.U., Wellige B., Bohmann A., Scharf M.** *Impact behavior of magnesium matrix composites* 12<sup>th</sup>. Dymat Technical Meeting, Coimbra Portugal, p. 57, Oct. **1999**
4. **Kainer K. U., Mordike B. L.**, *Magnesium-Alumina Composites-Production and Properties*, Proceedings Verbundwerk '90, S. 17.1 - 17.15, Ed.: Schnabel S., FNW Forschungsinstitut Neue Werkstoffe, Frankfurt, BRD, **1990**
5. **Kainer K. U., Böhm E.**, *Squeeze-Casting of Magnesium Alloys* VDI Reports No1235, **1995**, pp. 117-125
6. **Kainer K. U.** *Isotropic properties of mixed Saffil-SiC<sub>p</sub>-Mg* Advanced Composites '93; Internat. Conf. ; the Minerals, Metals & Materials Society, **1993**

# Constitutive law of a brittle material

P. Bailly

E.N.S.I.B. , *Laboratoire Energétique, Explosions, Structures*  
10 boulevard Labitolle -18 020 Bourges cedex, France  
*patrice.bailly@ensi-bourges.fr, Tel: 02 48 48 40 02 , Fax: 02 48 48 40 50*

## 1 Introduction

Scientists name quasi brittle or imperfectly brittle materials like the concrete, the rocks or ceramics. These materials are marked by a constitutive heterogeneity and the damage, brittle on a microscopic scale, generates structural mechanisms (friction...) which give, on a macroscopic scale, a behaviour called quasi brittle. The traditional mechanic of cracking is not always able to describe the breaking process. Significant projections were made in the approach of modelling of these materials, in particular by Z.P. Bazant (energy of rupture, characteristic length, scale effect). The dynamic behaviour remains however still surrounded by many mysteries (change of order of magnitude of apparent resistance, multi cracking, diffused damage...). Beyond phenomenological models, the search of the most relevant description of the mechanisms of rupture remains a current subject of study. The mechanics of the continuous mediums provides a tested framework, any characteristics (discontinuities, fractional aspect , medium with two or three phases, random structure...) can encourage with enrichments, or different concepts (of discrete type). The knowledge of physics related to the degradation of material and its translation in a constitutive model, are for materials quasi-brittle in a "state of the art" clearly under what exists for metallic materials.

## 2 The phenomenology

### 2.1 The apparent strength increase with strain rate

It is usual to observe on compressive dynamic tests that the strength depends on the strain rate (fig.1) [1] [2]. The simulations of the dynamic compressive tests show that the strain field is not homogeneous in the specimen and it is not correct to deduce a realistic behaviour, assuming a quasi-static state. So, a doubt is checked on the discussion and conclusion about the strength increase and the rate sensitivity of concrete, when they are argued with results assuming (implicitly) the homogeneity of strain and stress in the specimen. A comprehension of the apparent strength increase may be submitted. When the plastic flow begins, the dilatancy induces a radial expansion. There is an inertial force acting on a part of the specimen, in respect with the radial movement [3]. The consequence is that, in the centre of the specimen, the pressure increases. The inertial forces create an « inertial confinement ». The yield limit of the concrete depends on the pressure. So it is possible that the compressive stress in the middle of the cylinder grows higher than the static strength (without confinement). This can be the principal explanation of the phenomenon but perhaps not the only one [4] [5]. Much carefulness is necessary about conclusion rate sensitivity for any loading paths, because the failure of concrete is an intricate problem. In particular, new experimental results on the dynamic tension strength exhibit a rate sensitivity which cannot be explain by a simple structural effect [6].

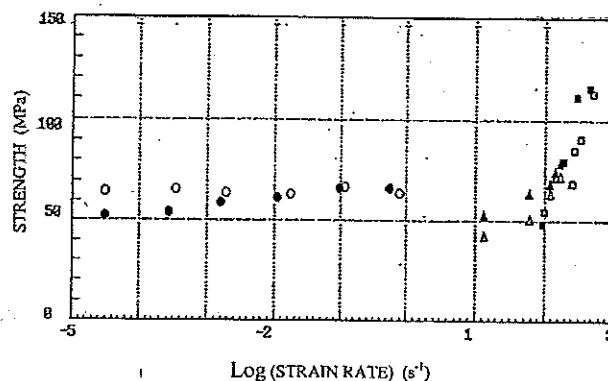


Figure 1 : strength observed in dynamic compressive tests [1].

## 2.2 The effect of high pressure

Under high pressure, the porous structure of the cementing matrix breaks down, porosity is closed again while a reduction in volume is observed. For the static case experimentation is worked out with the hydrostatic loading path. For the dynamic case the one dimension strain loading path is used. The results of these two tests are not very different and any may consider the compacting independent of the strain rate. In fact, if both the dynamic and the static compressive tests are worked out with the same loading path, the rate dependence is significant (fig. 2). The importance of the loading path on the compacting is shown in fig.3. [7]

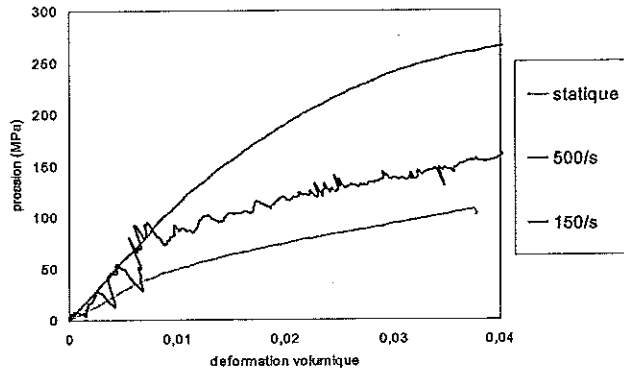


Figure 2 : dynamic oedometric compressive tests at several strain rate.

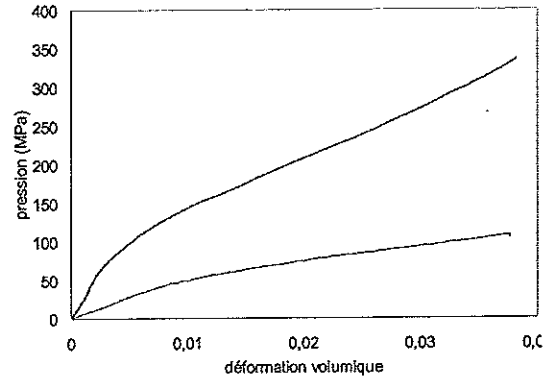


Figure 3 : compacting curves in an hydrostatic test (up) and an oedometric test (down).

## 3 Modeling of the behavior

### 3.1 Damage, shearing and compacting

Many models exist for concrete [8-18]. Some are convenient for static loading and low pressure. Some are deduced from metal modelling. Many of them are defined with a great number of parameters.

Damage, shearing and compacting are the three phenomena considered in the present modelling. The model is worked out using the classical theories of the damage, the plasticity and the visco-plasticity. This theory of the multi mechanism is used in order to couple criteria of rupture. Also, it makes it possible to represent the behaviour of a material subjected to various ways of loading, by the introduction of various sources of plasticity. By taking into account all the activated plastic potentials, the formula spreads in the following way (with the usual convention):

$$\underline{\dot{\sigma}} = \underline{\underline{A}} : \left( \underline{\dot{\epsilon}} - \sum_{i=1}^n \lambda_i \frac{\underline{\underline{Y}}_i}{\underline{\underline{Y}}} \right)$$

When the plastic multiplier  $\lambda_i$  is positive, it is said that mechanism  $i$  is active. In the present model the two mechanisms are characterised by a criterion (surface) :

- 1 for the criterion representing the phenomenon of shearing.
- 2 for the criterion representing the phenomenon of compacting.

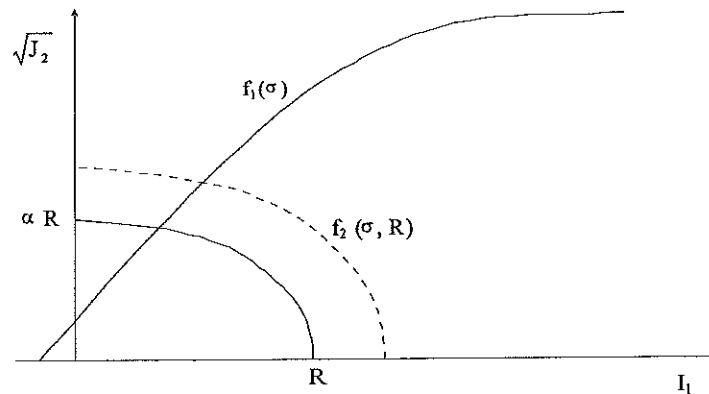


Figure 4 : The two criteria in the two invariant plan

### 3.2 The elasto-viscoplastic model of the shearing

The concrete shows a sensitivity of the mean stress, so the plasticity criteria is of the Drucker-Prager type . It is written as the following expression :

$$f_1(\underline{\sigma}, Y_H) = \sqrt{J_2} + \alpha I_1 - Y_H$$

where:  $\alpha$  and  $Y_H$  are two parameters depending on the material and determined from static tests.

The softening is characterised by the loss of material cohesion and varies linearly according to the cumulated plastic strain.

$$Y_H = \langle Y_0 - \beta E p_c \rangle$$

where:  $Y_0$  = initial cohesion,  $E p_c$  = accumulated plastic strain.

The viscoplasticity is of Perzyna's type [19]. It has the following expression :

$$\dot{\underline{\epsilon}}^p = \frac{1}{\eta_1} \langle f_1(\underline{\sigma}, Y_H) \rangle \frac{\partial g_1}{\partial \underline{\sigma}}$$

where:  $\eta_1$  = viscosity coefficient.

This coefficient is in relation with a characteristic length through the relation :

$$\ell_c = \frac{2\eta_1}{\sqrt{E\rho}}$$

In the case of geomaterials, an associated model shows an over-important expansion behaviour. This model is non-associated and function  $g$  is written as following :

$$g_1 = \sqrt{3} J_2 + \gamma I_1$$

The term  $\gamma$  represents the expansion phenomenon.

The elastic strain is obtained by partition of the deformations

$$\dot{\underline{\epsilon}} = \dot{\underline{\epsilon}}^e - \dot{\underline{\epsilon}}^{vp}$$

### 3.3 The damage model

Damage models are generally used to show a degradation of the material due to a microcracking characterised by a loss of rigidity [20]. These models are formulated using the laws of irreversible processes of thermodynamics. The model used here is a damage model with velocity effect. [21] In order to respect the second law of thermodynamics, the variable which represents the damage evolution must always be defined as positive or equal to zero.

The evolution of damage is defined as follows:

$$\dot{D} = \mathfrak{R}(\tilde{\underline{\epsilon}}) \quad \text{with} \quad \tilde{\underline{\epsilon}} = \sqrt{\sum \langle \underline{\epsilon}^+ \rangle^2}$$

The equivalent strain  $\tilde{\underline{\epsilon}}$  is equal to the sum of the main positive strains [23].

Using a damage threshold function  $F$ , the damage evolution will be defined as follows :

$$\dot{D} = \left( \frac{\langle F \rangle}{m} \right)^n \quad \text{with} \quad F = (1-D)[\tilde{\underline{\epsilon}} - \epsilon_{d0} / (1-D)]$$

$\epsilon_{d0}$  = damage threshold, and  $D$  = damage variable.

Through the expression of this function, the second thermodynamic law is verified. The damage evolution is always defined as positive and the damage cannot be greater than 1. The stress is obtained by the following expression :

$$\underline{\underline{\sigma}} = (1-D) \underline{\underline{A}} : \underline{\underline{\epsilon}}^e$$

$\underline{\underline{A}}$  is the fourth order elasticity tensor

### 3.4 Modelling of compacting

In order to represent the behaviour of the concrete under strong requests, a criterion of rupture is coupled with the criterion of shearing. This criterion of compacting has a rough surface which is closed again on the hydrostatic axis. Being given the scarcity of the experimental data relating to this rough surface, its precise form is not easily identifiable. Also, a circular surface was selected. This surface depends on the first two invariant stress ( $I_1$  and  $J_2$ ), contrary to certain surfaces "Cape" represented by an equation of the  $I_1 = \text{constante}$  type, and has a formulation simpler than a surface of the type Gurson. Two surfaces are interdependent, i.e. that an activation of one mechanism of plasticity has consequences for other surface. This rough surface  $f_2$  has as an equation:

$$f_2(\sigma) = \sqrt{(J_2 + I_1^2 - R^2)}$$

The variable R is the parameter of the hardening. This hardening is expressed in the following way:

$$R = \frac{R_0}{1 + \frac{DVP}{pr}}$$

with DVP which represents the plastic volumetric deformation, Pr porosity and R<sub>0</sub> the value threshold of compacting. The plastic strain rate is given by the law of Perzyna :

$$\underline{\underline{\dot{\varepsilon}}}_2^P = \frac{1}{\eta_2} \frac{\langle f_2(\underline{\underline{\sigma}}, Y_H) \rangle}{f_2(\underline{\underline{\sigma}}, Y_H)} \frac{\partial f_2}{\partial \underline{\underline{\sigma}}}$$

with  $\eta_2$  = viscosity

It is an associated plastic flow. When the two criteria are activated the hardening parameters as follows.

$$f_1(\sigma) > 0 \text{ et } f_2(\sigma) > 0; Y_H = \min\{Y_0 - \beta_1 E_{p1}; \beta_2 E_{p2}; Y_0\}$$

$$f_1(\sigma) > 0 \text{ et } f_2(\sigma) > 0; R = \frac{R_0}{1 + \frac{DVP}{pr}}; DVP = \text{trace}(\underline{\underline{\varepsilon}}_1^P) + \text{trace}(\underline{\underline{\varepsilon}}_2^P)$$

$$\text{with : } E_{p1} = \int_0^t \sqrt{\underline{\underline{\dot{\varepsilon}}}_1^P : \underline{\underline{\dot{\varepsilon}}}_1^P} \quad \text{et} \quad E_{p2} = \int_0^t \sqrt{\underline{\underline{\dot{\varepsilon}}}_2^P : \underline{\underline{\dot{\varepsilon}}}_2^P}$$

If there is compacting, the cohesion can grow, and the damage parameter is assumed to decrease to zero.

$$f_2(\sigma) > 0 \Rightarrow \underline{\underline{\sigma}} = \underline{\underline{A}} : \underline{\underline{\varepsilon}}^e \quad \text{the elastic strain is } \underline{\underline{d\varepsilon}}^e = \underline{\underline{d\varepsilon}} - \underline{\underline{d\varepsilon}}_1^P - \underline{\underline{d\varepsilon}}_2^P$$

The damage is calculated independently of the criteria of shearing and of compacting and is taken into account only when the criterion of compacting is inactive. When the  $f_2$  criterion becomes active, the variable of damage is brutally brought back to zero. That induces a negative term of dissipation. This is however acceptable because there exists at the same moment a strong positive dissipation due to the plastic flow, total dissipation having to remain positive. The thermodynamic processes are supposed to be isothermal and the variables used are classified in variables of state and variables associated [22]. The inequality of Clausius-Duheim, which precise that the intrinsic dissipation must be positive, is satisfied. If these two potentials are not expressed, which is the case in this model, being given variables of work hardening chosen, it should be checked that intrinsic dissipation is positive. Within the framework of this model, this expression is as follows:

$$\underline{\underline{\sigma}} : \underline{\underline{\dot{\varepsilon}}}_1^P + \underline{\underline{\sigma}} : \underline{\underline{\dot{\varepsilon}}}_2^P + Y_H \dot{E}_{p1} + \frac{1}{2} \left( \underline{\underline{\varepsilon}}^e : \underline{\underline{A}} \underline{\underline{\varepsilon}}^e \right) \dot{D} + R \dot{DVP} \geq 0$$

This last inequality must be checked so that the laws of thermodynamics are satisfied, in particular when D decreases when the  $f_2$  criterion is reached.

## 4 Simulation of the concrete behaviour

### 4.1 Identification of the parameters

The angle of friction and the initial cohesion of material are given starting from triaxial compression tests. The concrete used to carry out the tests of dynamic compacting is the microconcrete named "MB50" [7]. The parameters of the criterion of shearing are given starting from the triaxial compression tests carried out without confining pressure and low confining pressure [23]. The figure below represents the evolution of the second invariant according to the pressure for a test unconfined compression and two triaxial compression tests. These three tests make it possible to determine the initial cohesion of the material (Y<sub>0</sub>) and "the angle of friction" of the criterion of shearing. This criterion is represented on figure 5. Indeed, according to the experimental results it is possible to take a criterion with a slope slightly weaker or stronger.

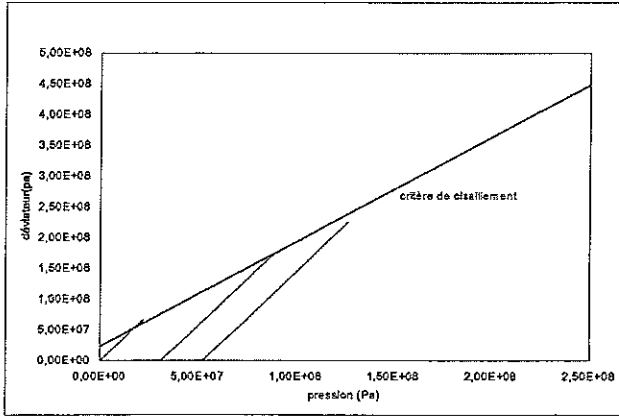


Figure 5 : Identification of the shear criterion

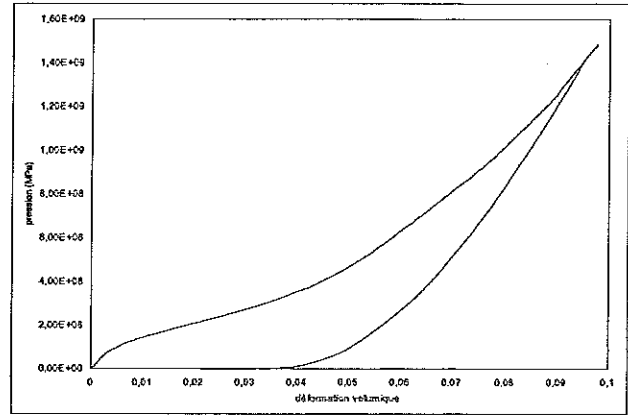


Figure 6 : hydrostatic test – pressure versus volumetric strain [12]

The threshold of compacting is given starting from a hydrostatic test (fig.6).  
Table above provides the values of the parameters used to carry out various simulations.

Parameters	Test	Value	Scale of possible values
Young's Modulus (Pa)	Compressive test	$23 \cdot E^{+9}$	$20 \cdot E^{+9} < E < 40 \cdot E^{+9}$
Specific mass (kg/m <sup>3</sup> )		2300	$2000 < \rho < 2500$
Poisson's ratio		0.17	$0.16 < \nu < 0.2$
Shear threshold (Pa)		$19 \cdot E^{+06}$	$4 \cdot E^{+6} < Y_H < 130 \cdot E^{+6}$
Frictional angle		0.46	$0.4 < \alpha < 0.8$
Compacting threshold (Pa)	Hydrostatic test	$80 \cdot E^{+6}$	$70 \cdot E^{+6} < R_0 < 100 \cdot E^{+6}$
Porosity		0.10	$0.05 < pr < 0.15$
Viscosity $\eta_1$ (Pa/s)	size of granular	$2 \cdot 0 \cdot E^{+4}$	$1 \cdot 0 \cdot E^{+4} < \eta_1 < 6 \cdot 0 \cdot E^{+4}$
Viscosity $\eta_2$ (Pa/s)	Dynamique compressive test	$2 \cdot 0 \cdot E^{+8}$	$1 \cdot 0 \cdot E^{+8} < \eta_2 < 5 \cdot 0 \cdot E^{+8}$
Hardening $\beta_1$ (Pa)	Triaxial test	$4 \cdot 0 \cdot E^{+08}$	$1 \cdot 0 \cdot E^{+8} < \beta_1 < 1 \cdot 0 \cdot E^{+9}$
Hardening $\beta_2$ (Pa)	Arbitrary	$1 \cdot 0 \cdot E^{+11}$	$8 \cdot 0 \cdot E^{+10} < \beta_2 < 3 \cdot 0 \cdot E^{+11}$
Expansion	Compressive test	0.4	$0 \leq \gamma \leq \alpha$
m	Arbitrary	$1 \cdot 9 \cdot E^{-3}$	$4 \cdot 0 \cdot E^{-04} < m < 3 \cdot 5 \cdot E^{-03}$
n		5	$2 < n < 9$
$\epsilon_{d0}$	Tensile test	$1 \cdot 0 \cdot E^{-04}$	$0 \cdot 5 \cdot E^{-04} < \epsilon_{d0} < 1 \cdot 5 \cdot E^{-04}$

One notices a great difference between the value of viscosity intervening in the criterion of shearing and that intervening in the criterion of compacting. That which intervenes in the criterion of shearing is related to a characteristic length, contrary to that intervening in the criterion of compacting. This last as a great influence during simulations.

## 4.2 Static compacting tests

These static tests of compacting were carried out with a cell of containment out of steel. Figure 7 presents, a comparison between the experimental results and those obtained by simulation, for a porosity of 0.10.

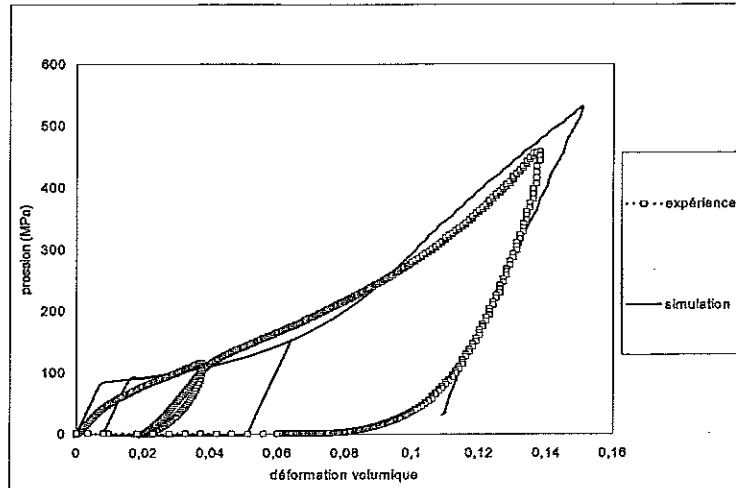


Figure 7 : Static compacting test

## 4.3 Dynamic compacting tests

A very simple method to reach high values of pressure consists in making oedometric tests. Using a technique derived of the method used by Burlion [13] under a quasi-static loading, the specimen tested is described in fig.8. Longitudinal and transversal strain gages are glued on the metallic ring. The first ones are to evaluate the friction between the ring, on one side, and metallic plugs and concrete on the other side. Transversal ones are measuring the radial expansion of the ring from what is deduced the actual lateral pressure on concrete. The loading is provided by a classical Split Hopkinson Bar System [14].

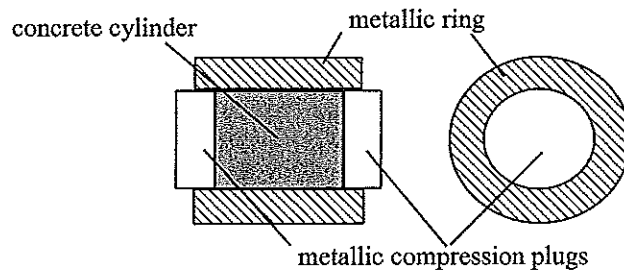


Figure 8 : experimental device for dynamic compacting tests

For each test, the evolution of the stress according to time, the evolution of the pressure according to the volumetric deformation as that of the second invariant according to the first are provided. The following figures present a example of comparison between the experimental results and those obtained by simulation. Figure 9 characterises the evolution of the normal stress according to the time. The figure 10 presents the evolution of the deviation stress according to the pressure.

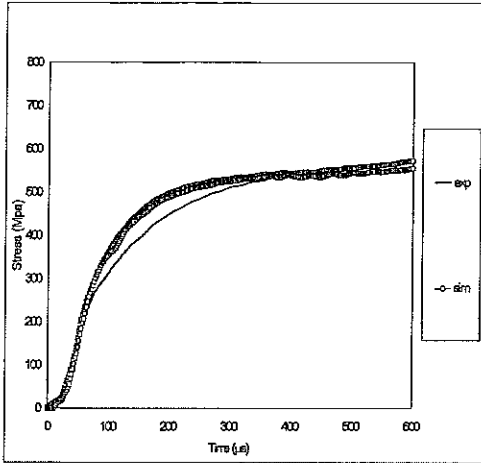
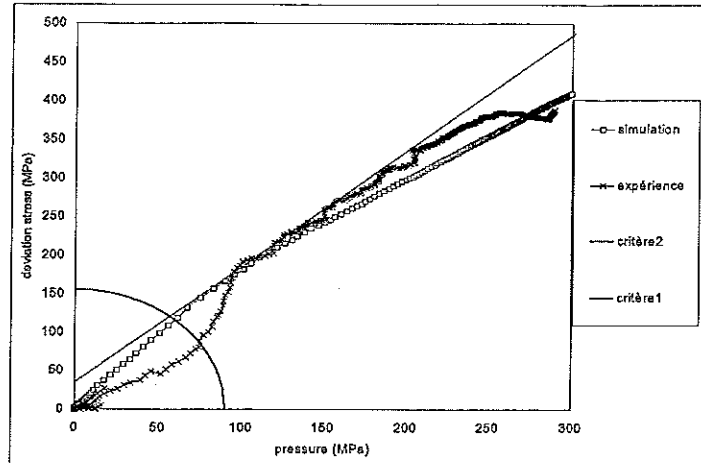


Figure 9 : the normal stress according to time.



The figure 10 : the deviation stress according to the pressure.

During these tests, it is difficult to obtain a measuring accuracy less than 1 % of the strain. The signals of the strain are a little disturbed in the elastic phase. It is nevertheless possible to obtain the evolution of the pressure according to the volumetric strain as that of the second invariant according to the pressure but the elastic part presents a certain inaccuracy. These simulations, carried out with a cell of containment out of steel, are satisfactory. For this test, the evolution of the stress according to time is well reproduced.

The evolution of the way of loading (deviation stress according to the pressure) is not very well reproduced during the elastic phase, but these experimental results is not very good for this part of the curve. Figure 10 shows that the loading path obtained by simulation is very close to the criterion of shearing. Also the viscosity used to calculate the viscoplastic strain has only a little influence.

## 5 Conclusion

The taking into account of the phenomenon of compacting is carried out by using a viscoplastic criterion. This one, of circular form, is coupled with the criterion of shearing. This coupling, carried out between two viscoplastic criteria, does not lead to numerical problems at the angular point between the two criteria. Viscosity, considered in the criterion of shearing, is related to a characteristic length and intervenes primarily like limiting device of localisation. Under low pressure, the strain rate dependence is, for the most part, a structural effect in the specimen. The viscosity intervening in the criterion of compacting has a significant value and makes it possible to translate the phenomenon of viscosity observed in experiments. The law of work hardening, extremely simple, seems to give satisfactory results.

## Acknowledgement

This work was partially supported by AEROSPATIALE Company.

The experimental tests were performed through the French Laboratory Network "GEO"

(LMS : G. Gary, LMT : N. Burlion et F. Gatuingt, LPMM : J. Klepaczko)

The computation were worked out by H. Le Nard with the code DYNA 2D

## 6 References

- [1] Gary G., Klepaczko J.R., "Essai de compression dynamique sur béton", GRECO Geomaterial scientific report, 105-118, 1992.
- [2] Bishoff P.H., Perry S.H., "Compressive behaviour of concrete at high strain rates", Materials and Structures, Vol.24, pp.245-450, 1991.
- [3] Bailly P. "Une modélisation d'un matériau fragile avec prise en compte d'effets dynamiques" C.R. Acad. Sci. Paris, t. 318, Série II, p. 727-732, 1994.
- [4] Gary G, Bailly P., "Behaviour of quasi-brittle material at high strain rate, Experiment and modelling", European Journal of Mechanics, 1998.

- [5] Rossi P., "Influence of cracking in the presence of water on the mechanical behaviour of concrete", Magazine of Concrete Research, 43, N°154, Mars, 53-57, 1991.
- [6] Brara A., "Étude expérimentale de la traction dynamique du béton par écaillage", Thèse, Université de Metz, 1999.
- [7] Bailly P. et al., "Comportement dynamique sur béton", GRECO Geomaterial, final scientific report, 1999.
- [8] Chen W.F., Han D.J. "Plasticity for structural engineers", Springer-Verlag - New York, 1988.
- [9] Han D.J., Chen W.F. "A nonuniform hardening plasticity model for concrete materials", Mechanics of materials, 4, 283-302, 1985.
- [10] Elwi A.A., Murray D. W. "A 3D hypoelastic concrete constitutive relationship". Journal of the engineering mechanics division, Vol. 105, N° EM4, August 1979.
- [11] Pietruszczak, Jlang J., Mirza F.A. "An elastoplastic constitutive model for concrete" Int. J. Solids Structures, Vol. 24, N°7, pp. 705-722, American Institute of Physics, 1988.
- [12] Deng H. and Nemat-Nasser S. "Dynamic Damage Evolution of Solids in Compression : Microcracking, Plastic Flow, and brittle-Ductile Transition", J. of Eng. Mat. And Technology, Trans ASME, 116, 268-289, 1994.
- [13] Dubé J.F. "Modélisation simplifiée et comportement visco-endommageable des structures en béton". Thèse de doctorat de l'université Paris 6, 1994.
- [14] Bicanic D. and Zienkiewicz O.C. "Constitutive model for concrete under dynamic loading" Earthquake Engineering and Structural dynamics, Vol 11, pp 689-710, 1983.
- [15] Sercombe J., Ulm F.J., Toutlemonde F., "Modeling of concrete in high rate dynamics", Structural Dynamics-EURODYN'96, Balkema, August, 1996.
- [16] Holmquist W. and Johnson M. " A computational constitutive model for concrete subjected to large strains, high strain rates, and high pressures " 14 th International Symposium on Ballistics, Quebec, Canada, 26-29 September 1993.
- [17] Ottosen N.S., "Non linear finite element analysis" Ris. National laboratory DK 4000 Roskilde Denmark, May 1980.
- [18] Sandler I.S., DiMaggio F.L., Baladi G.Y. "Generalized CAP model for geological materials" Journal of the Geotechnical Engineering Division, Vol. 102, N° GT7, July 1976.
- [19] Perzyna P., "The constitutive equations for rate sensitive plastic materials"
- [20] Kachanov M., "Continuum model of medium with cracks", Journal of the Engineering Mechanics Division, vol. 106, EM5, october 1980.
- [21] Mazars J. "Application de la mécanique de l'endommagement au comportement non linéaire et à la rupture du béton de structure". Thèse de doctorat d'état de l'université Paris 6, 1984.
- [22] J. Lemaître, J.L.Chaboche, "Mécanique des matériaux solides", Dunod – Paris, 1985.
- [23] Buzaud E., "Caractérisation du comportement mécanique du microbéton MB50 sous chargement quasi-statique" - Résultats d'essais, Colloque « GEO », novembre 1997.
- [24] Burlion N., »Compaction des bétons, éléments de modélisation et caractérisation expérimentale, Thèse de l'E.N.S. de Cachan, 18 Novembre 1997.
- [25] Hopkinson B., "A method of measuring the pressure in the deformation of high explosive by impact of bullets", Philosophical Transactions of the Royal Society of London, A213, 437-452, 1914.
- [26] Kolsky H., "An investigation of mechanical properties of materials at very high strain rates of loading", Proceedings of the Physical Society London, B62, 676-700, 1949.

# HIGH VELOCITY IMPACT ON NEW POLYMERIC MATERIALS LOADED WITH CERAMIC PARTICLES

A. Arias, R. Zaera, J. López-Puente, J. Fernández-Sáez, C. Navarro

Mechanical Engineering Department, Carlos III University of Madrid

Avda. de la Universidad 30, 28911 Leganés, Madrid, Spain.

Tfn: 34-91-6249491, Fax: 34-91-6249430. E-mail: navarro@ing.uc3m.es

## Abstract

An experimental and numerical study work was done to investigate the ballistic performance of a new ceramic-particle-loaded polymeric material composed of vinylester resin and low cost ceramic particles of  $\text{Al}_2\text{O}_3$  (1-8 mm). The manufacturing process, simple and cheap, produces a material with a ballistic efficiency intermediate between the conventional metallic materials and the monolithic ceramic used in lightweight armours.

Full-scale fire tests were carried out on laterally confined tiles backed by an aluminum block. The measure of the residual penetration shows the effect of the ceramic particle size on the ballistic efficiency of the material. A model for this new material is proposed, implemented in a numerical code and validated with experimental data.

*(Keywords: ballistic efficiency; ceramic particles; depth of penetration; impact; lightweight armours)*

## 1.- INTRODUCTION

The main parameters of lightweight armours design are ballistic efficiency and cost. The ballistic efficiency is the relationship between the protection capacity and the areal density (weight/area) needed to arrest the projectile. Metallic materials present disadvantages due to their high density. Mixed armours, made of monolithic ceramic tiles and a metallic plate, seem to be a very efficient shield against low and medium calibre projectiles since they combine the light weight and high resistance of a ceramic with the ductility of metallic materials (Navarro et al. 1994, den Reijer 1991). However, the use of ceramic tiles in mixed armours has the limitation of its high cost. Weight versus cost in different armours are shown in Figure 1 (Roberson 1995). While the ballistic efficiency of the armour increases significantly when ceramic material is used, the cost also rises. The development of a new material that covers the gap between metallic and ceramic ones could be interesting for applications where weight is not the primary concern and cost saving should be achieved.

In this work a new material made of ceramic particles and vinilister matrix were developed. The task of the ceramic particles is to break up the impacting projectile and reduce its penetration capacity. The vinilester matrix gives the needed cohesion between particles and distributes the impact load over a large area of the metallic backing plate.

Full-scale fire tests have been carried out to evaluate the properties of the new material, and to consider its application to the design of new armours with intermediate detention capacity at low cost. A model that considers damage in the ceramic material has been implemented in a numerical code and compared with experimental results.

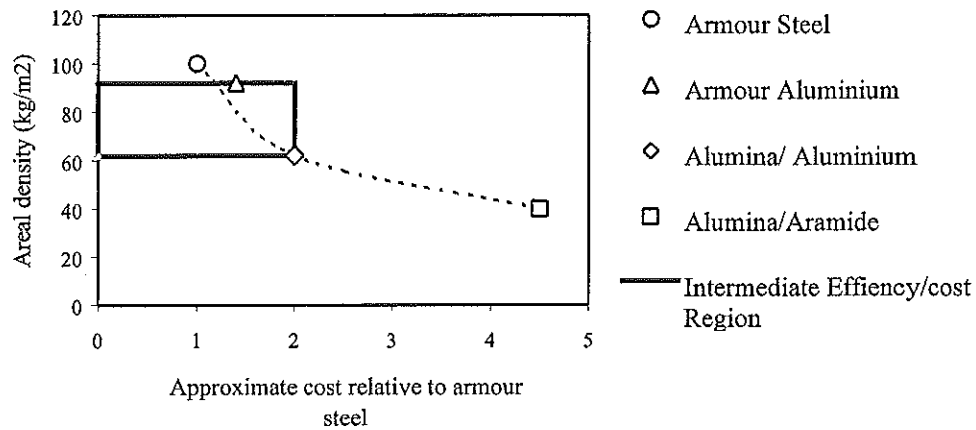


Figure 1. Performance vs Cost for armours to defeat 7.62 NATO AP. Cost relative to armour steel

## 2. MANUFACTURING PROCESS

### 2.1 Materials

For the ceramic load, alumina particles of 99,4 % purity (manufactured by Alcoa Chemical) were used. Table 1 shows the size distribution of the particles supplied by Alcoa. Different mean sizes  $\bar{\delta}$ , and compactation levels could be obtained by mixing particles of different intervals.

Grain intervals	[1-3] mm	[3-6] mm	[5-8] mm
$\bar{\delta}$ (mm)	1,92	3,37	6,67

Table 1. Size intervals for ceramic particles.

The properties of the vinylester resin are given in Table 2. Due to its low density, the composite will be lighter.

Mass density (kg/m <sup>3</sup> )	1100
Tensile strength (MPa)	70
Ultimate elongation (%)	2,3 – 4
Modulus of elasticity (MPa)	3300 MPa

Table 2. Mechanical properties of vinylester

The resin and ceramics particles are cheaper than the materials use normally in lightweight armours. Table 3 shows an approximate price comparison.

Material	Approximate Cost ( €/ kg )
Monolithic Alumina	28
Aluminium	8
Vynilester	4
Alumina Ceramic Particles	1
80 % Ceramic Particles + 20 % Vynilester (weight)	1.6

Table 3. Approximate cost comparison

## 2.2 Mixing and compactation

The manufacturing process is of two phases. In the first one, all the components (resin, catalyser, activator and particles) are mixed in their correct proportions until a homogeneous material is obtained. The resin must wet the particles to guarantee good cohesion, and the proportion of ceramic must be high enough to produce a material with erosive properties. These two requirements will be met when the composite has the same volume of vynilester resin and ceramic particles at the end of the manufacturing process.

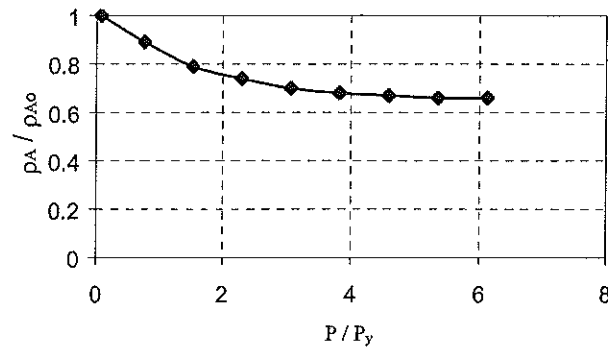


Figure 2. Compactation process

In the second phase, the mixture is compacted until the polymerization finishes. The uniaxial pressure (from 1 to 6 MPa) is the most important parameter to get a composite with good mechanical properties and low porosity (< 2 %). By controlling the pressure, tiles of different areal density tiles were obtained. On registering the values of load and displacement, a exponential equation that relates final areal density  $\rho_A$ , initial areal density  $\rho_{A0}$  and the compactation pressure  $P$  was fitted (Messing et al. 1982):

$$\frac{\rho_A}{\rho_{A0}} = m \cdot \left( \frac{P}{P_y} \right)^k \quad (1)$$

where  $P_y$ ,  $m$  and  $K$  are constants determined experimentally. This equation is plotted in Fig. 2.

### 2.3 Manufactured tiles

To analyse the ballistic behaviour of the composite material, tiles of different areal densities  $\rho_A$  and different proportions of grain size intervals were considered. The proportions of the grain size intervals for an optimal compactation was determined, with a Fuller reference curve, commonly used in the concrete industry. Particles larger than the tile half thickness were eliminated to get a homogeneous particle distribution throughout the tile. Table 3 shows the proportions chosen for two different grain mixtures.

	[1-3] mm	[3-6] mm	[5-8] mm	$\bar{\delta}$ (mm)
Large Grain	50%	30%	20%	4,7
Small Grain	20%	30%	50%	3,2

Table 3. Granulometry of manufactured tile

To compare the ballistic efficiency of the composite material with a monolithic ceramic, a 95% purity alumina (Matroc AD 95 Sintox FA, 80 x 80 x 6 mm) was taken as reference material, its areal density being  $\rho_{Ac}=22.7 \text{ kg/m}^2$ . Composite tiles with three different areal densities ( $\rho_{A1}=\rho_{Ac}$ ,  $\rho_{A2}=1,5\rho_{Ac}$ ,  $\rho_{A2}=2\rho_{Ac}$ ) were manufactured.

### 3.- FULL-SCALE FIRE TEST DOP.

The depth-of-penetration (DOP) test has been used to investigate the ballistic performance of ceramic tiles since around 1986 (Yaziv et al. 1986). This test is able to evaluate the efficiency of various ceramic materials. A ceramic material tile is backed by a "semi-infinite" metallic block and impacted by a projectile. Then the residual penetration  $p_r$  is measured and compared to the penetration  $p$  in the metallic block (Figure 3). These values are used to calculate the mass efficiency factors (Hohler et al. 1995)

$$MEF = \frac{\rho_b p}{\rho_c h_c + \rho_b p_r} \quad (2)$$

where  $\rho_b$  and  $\rho_c$  are the densities of the metallic material and of the ceramic, and  $h_c$  is the thickness of the ceramic tile.

The projectile used in this study was a LAPUA 7,62-AP with a tungsten carbide core of 5,9 g and length/diameter = 3,6 (Figure 4). The impact velocity was 940 m/s.

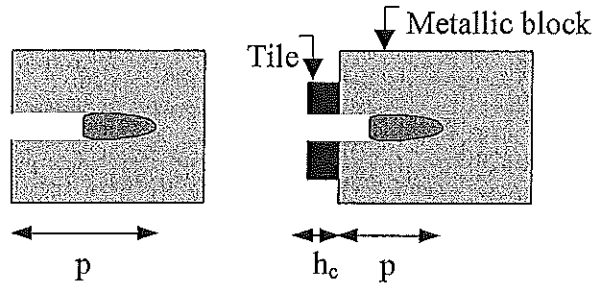


Figure 3. Residual penetration with and without tile in a DOP test

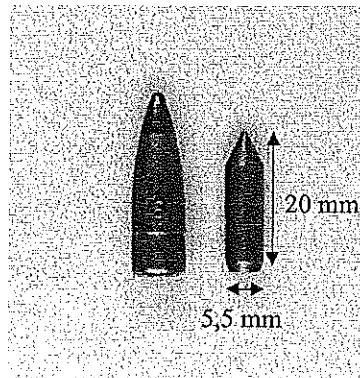


Figure 4. Projectile Lapua 7,62 AP and its tungsten carbide core

Ceramic and composite tiles were confined laterally and the tile was joined to a 2017-T451 aluminium block (commonly used in armouring) with a 0,4 mm thick epoxy layer. The reference penetration in the aluminium block was  $p=42$  mm.

#### 4- EXPERIMENTAL RESULTS

The penetrations in the aluminium blocks were measured using an ultrasonic device. The experimental data are summarized in Table 4.

	$\bar{\delta}$ (mm)	$h_c$ (mm)	Areal density (kg/m <sup>2</sup> )	$p_r$ (mm)
AD95 monolithic tile	-	6	23	21
$\rho_{A1}$ Large grain	4,7	10	23	26
$\rho_{A1}$ Small grain	3,2	10	23	28
$\rho_{A2}$ Large grain	4,7	15	34,5	22
$\rho_{A2}$ Small grain	3,2	15	34,5	24
$\rho_{A3}$ Large grain	4,7	20	46	17
$\rho_{A3}$ Small grain	3,2	20	46	19

Table 4. Penetration results

Different aspects are shown in Figure 5. The residual penetration of the composite material decreases linearly with the tile areal density. This behaviour is characteristic also of monolithic ceramic tiles (Anderson et al. 1992, Hohler et al. 1995). Grain size affects the efficiency of the composite: the larger the size the lower the penetration in the block. This behaviour has been observed in previous works (Sánchez et al. 1999). The efficiency of the composite material seems to be intermediate between armour aluminium and monolithic alumina.

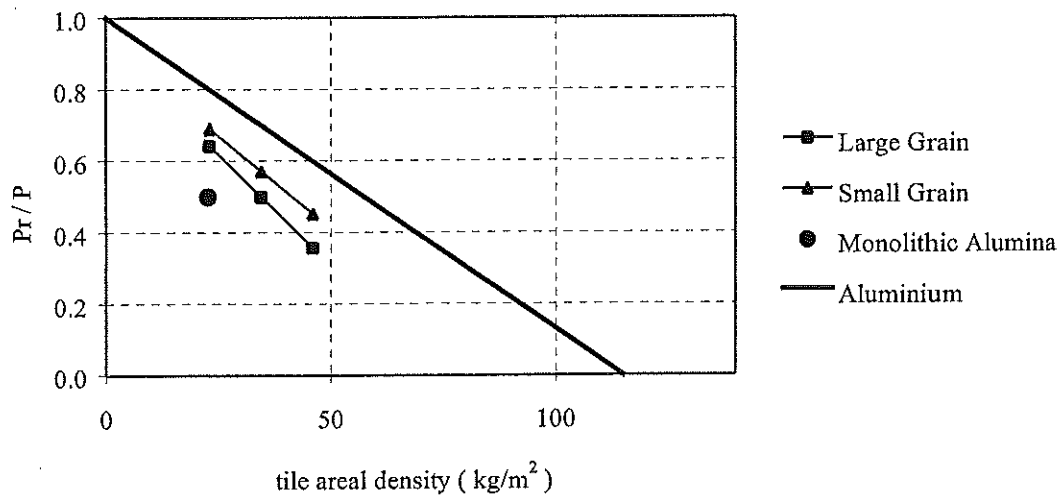


Figure 5. Adimensional residual penetration  $P_r/P$  versus areal density

Now considering the MEF, the same behaviour was observed: higher efficiency when larger ceramic particles were used, and intermediate MEF between monolithic alumina and aluminium.

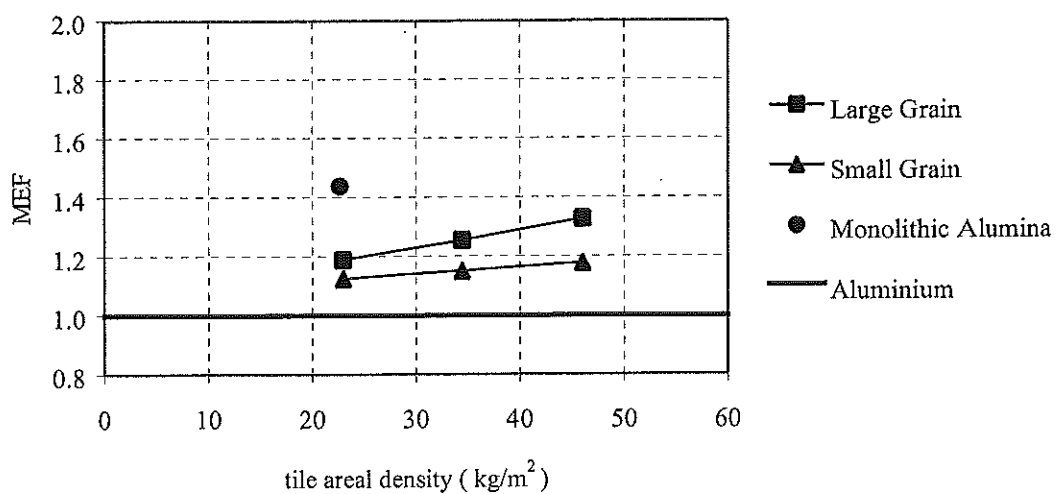


Figure 6. Mass efficiency factor MEF versus ceramic areal density tile

#### 4- SIMULATION

For the ceramic material fraction, the damage model proposed by Cortés et al. (1992) was adopted. This model considers a damage variable  $\eta$ , that defines the fragmentation of the ceramic,  $\eta=0$  standing for intact material, and  $\eta=1$  for comminuted material. At a given instant, a material point has a damaged fraction  $\eta$  and an intact fraction  $(1-\eta)$ . The evolution of the damage is specified by the following relation:

$$\dot{\eta} = \begin{cases} \dot{\eta}_0 \cdot (\sigma - \sigma_0) & \text{for } \sigma > \sigma_0 \\ 0 & \text{for } \sigma \leq \sigma_0 \end{cases} \quad (3)$$

where  $\sigma$  is the hydrostatic stress,  $\dot{\eta}_0$  is a parameter of the material, and  $\sigma_0$  the threshold of hydrostatic stress for the initiation of fracture. The yield stress is determined from the two fractions of the material as follows:

$$Y = (1 - \eta)Y_i + \eta Y_c \quad (4)$$

in which  $Y_i$  is the elastic limit of the intact material, and  $Y_c$  the elastic limit of the fragmented material. Since the latter does not undergo hardening, then

$$Y_c = \mu\sigma \quad (5)$$

$\mu$  being a coefficient of internal friction. For the intact fraction, a Drucker-Prager criterion is adopted:

$$Y_i = a - b\sigma \quad (6)$$

where  $a$  and  $b$  are defined using the values of static strength at tension and compression.

The ceramic fraction in composite material has an initial fragmentation degree. Thus, the initial fragmentation degree should be greater than zero before impact. This initial value depends on the different ceramic particle sizes in the composite tile and was determined by assigning a fragmentation degree  $\eta$  to each particle size,  $\delta$ , and calculating an average damage for the tile. To assign this fragmentation degree, the following function was proposed

$$\eta = \frac{K}{\delta + K} \quad (10)$$

The second material of the composite is the vinilester. For this resin, a Cowper-Symonds equation was used, relating the elastic limit  $\sigma_{ya}$ , the plastic strain  $\varepsilon_{pa}$ , and the plastic strain rate  $\dot{\varepsilon}_{pa}$ .

$$\sigma_{ya} = \left( Y_{a0} + C_1 \varepsilon_{pa}^x \right) \left( 1 + (C_2 \dot{\varepsilon}_{pa})^n \right) \quad (11)$$

in which  $Y_{a0}$ ,  $C_1$ ,  $C_2$ ,  $x$  and  $n$  are the material constants.

The mechanical properties of the composite (elastic limit, bulk modulus, shear modulus, density) were calculated from the volume fraction of the ingredients of the material. If  $v_{vin}$  is the volume fraction of vinilester,  $P_r^{vin}$  any property of the vinilester and  $P_r^{gran}$  same property of the ceramic particles, the property of the tile material is given by

$$P_r = P_r^{vin} \cdot v_{vin} + P_r^{gran} \cdot (1 - v_{vin}) \quad (12)$$

This model was implemented in the finite differences commercial code Autodyn-2D and all DOP tests were simulated. As shown in Figure 7, the numerical results agree with experimental results.

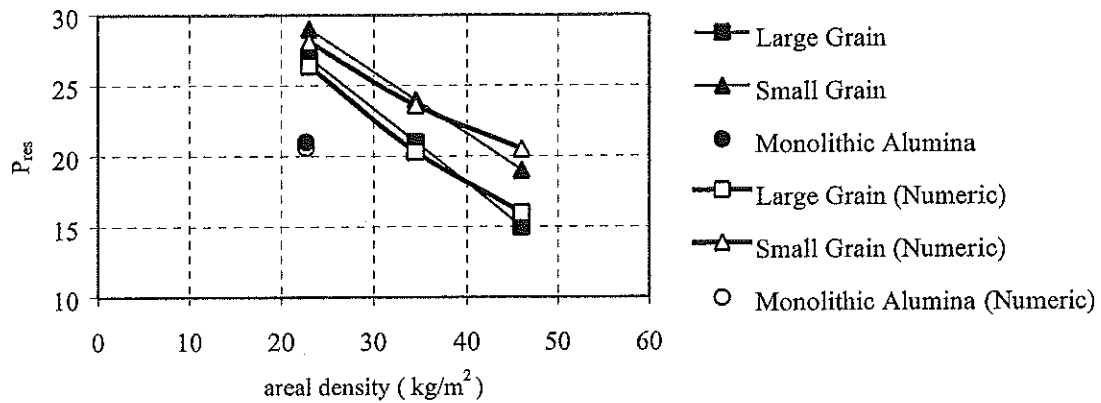


Figure 7. Experimental and numerical results

## 5- CONCLUSIONS

- The efficiency of the material developed is halfway between that of the traditional metallic materials and that of monolithic ceramic materials.
- Larger size ceramic particles improve the efficiency of the material.
- The low cost of the material makes it suitable for applications in which light weight is not of prime importance.
- The numerical model may be used to predict the ballistic behaviour of the material.

## 6- ACKNOWLEDGEMENTS

The authors are indebted to the Comunidad Autónoma de Madrid (Project 07N/0004/1998) for the financial support of this work.

## 7- REFERENCES

Anderson C.E, Jr, Morris B. L.(1992), "The ballistic performance of confined Al<sub>2</sub>O<sub>3</sub> ceramic tiles ", *Int. Journal Impact Engng.*, 5,33-59.

Autodyn-2D (2001), Century Dynamics Ltd., Dynamic House, Hurst Road, Horsam, U.K.

den Reijer P.C. (1991), "Impact on ceramic faced armours", Ph. D. Thesis, Delft University of Technology.

Hohler V., Stilp A.J., Weber K. (1995), "Hypervelocity penetration of tungsten sinter-alloy rods into alumina", *Int. J. Impact Engng.*, 17, 409-418.

Messing, G.L., Markhoff, C.J. y McCoy L.G., (1982), "Characterization of ceramic powder compaction", *Ceramic Bulletin*, 61, (8), 857-860.

Navarro C., Zaera R., Cortés R., Martínez Casanova M.A. (1994), "The response of ceramic faced lightweight armours under projectile impact", *Structures under Shock and Impact III*, 323-330.

Roberson C. J. (1995), "Ceramic Materials and Their Use in Lightweight Armour Systems", *Proceedings Lightweight Armour System Symposium*, Roya Military College of Science, Cranfield, U.K.

Sánchez-Saez S., Arias A., Zaera R., Navarro C. (2000), "Materiales compuestos de matriz polimérica y refuerzo cerámico en blindajes ligeros" *VI Congreso Nacional de Mecánica Aplicada e Computacional*, Aveiro, Portugal pp 304-310.

Yaziv D., Rosenberg Z., Partom Y., (1986), "Differential ballistic efficiency of lightweight armours", *Proceedings on the 9th International Symposium on Ballistics*, Shrivenham, U.K.

# **A THREE LAYERED AND BASED CERAMIC MULTIMATERIALS FOR ARMORS**

S.I. ANDERSEN<sup>1</sup> - L.GUILLAUMAT<sup>2</sup>

<sup>1</sup> RISOE National Laboratory  
Frederiksborvej 399 P.O. 49, DK – 4000 ROSKILDE  
[www.risoe.dk](http://www.risoe.dk)

<sup>2</sup> LA.M.E.F.I.P. - E.N.S.A.M.  
Esplanade des Arts et Métiers 33405 Talence Cedex FRANCE.  
[www.lamef.bordeaux.ensam.fr](http://www.lamef.bordeaux.ensam.fr)

**KEYWORDS** : Impact - drop weight - damage - ceramic - laminate

## **ABSTRACT**

The aim of this study is to introduce an impact damage into the armour constituents and materials, to simulate low energy collision and other accidental low velocity impacts.

The structure consists of a thick Dyneema laminate with a 15 mm thick Alumina Ceramic layer bonded to the laminate by an adhesive. The surface is covered by a 2 mm Al-plate (7075). The impact tests have been performed using a dropping mass with an energy from 30 up to 320 J.

The failure of the ceramic layer occurs for a force greater than about 40kN. The energy is about 100J. The failure induces a large fall in the curve force as function of time.

## **INTRODUCTION**

During handling, mounting and while fitted to the vehicle an add-on armour module will be exposed to impacts at low velocities and energy. The purpose of the low energy collision activity is to determine to what extent the ballistic properties of an add-on armour module is affected by such low energy impacts.

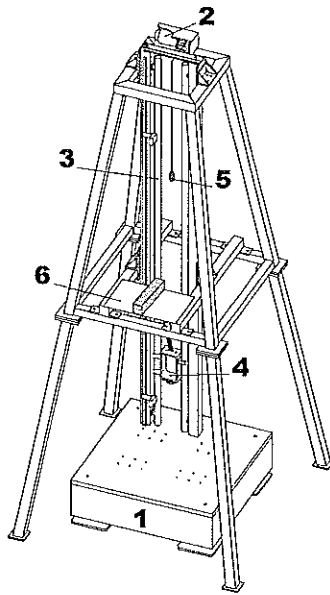
The aim of the testing is to introduce an impact damage into the armour constituents and materials, to some extent simulating low energy collision and other accidental low velocity impacts. The damage shall subsequently be quantified and its effect on the protection behaviour of the armour verified.

The low energy impact damage of the armour is in this context to be regarded as a conditioning of the material - similar to conditioning by temperature or moisture.

The present report covers the impact conditioning of the ceramic specimens and presentation of results obtained from the measurements performed during the impact tests.

## **EXPERIMENTAL DEVICE**

The impact tests have been performed using a dropping mass set-up completely designed in the LAMEFIP to simulate accidental falls on a structure (Figure 1).



- 1) base,
- 2) electric motor,
- 3) columns,
- 4) drop weight,
- 5) magnet,
- 6) set-up preventing the double hit.

**Figure 1.** *Schematic diagram of the impact testing machine.*

This original apparatus makes it possible to use adjustable mass which drops vertically from any height up to 3 meters. The impact testing machine has three main components. The first one is a metallic frame on which two steel columns are attached, the second one is a solid base made of concrete where the specimen frame is put and the last one is the impactor which consists of two components : a dropping crosshead and an impactor rod which was equipped with a 30 mm diameter steel end. An electric motor raises the mass by using a magnet. The drop height is determined by the position of a first infrared sensor, which stops the motor at the desired level. A second sensor located on the set-up close to the specimen triggered a rebound apparatus, which trapped the dropping mass automatically after impact to prevent a double hit on the structure.

The contact force history between the striker and the composite specimen is measured by means of a piezoelectric sensor, which is located between the impactor rod and its end. A first laser sensor placed just underneath the centre of the specimen provides the out-of-plane displacement history. A second laser sensor measures the striker displacement history, which makes it possible to calculate the velocity of the dropping mass just before and after the impact. Moreover, the tests have been filmed by a high-speed camera system Camsys+ (2,000 up to 11,000 frames/sec). Data was recorded using a plugging card in a P.C. computer.

The structures were simply supported using two steel supports (Figure 2).

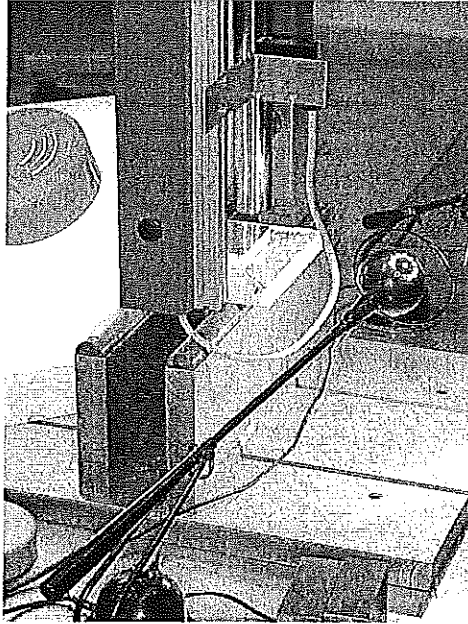


**Figure 2.** Specimen line support by two straight steel rails, support distance 120 mm. Radius at semi-circular supports 15 mm.

Experimental data was analysed with a Fast Fourier Transform (F.F.T.) and some numerical filters to identify all the frequencies which compose more especially the signal of the contact force history between the nose of the impactor and the specimen.

All tests were performed in the ambient temperature and humidity conditions of the laboratory.

### **SPECIMENS**

The specimens consists of a 200·200 mm, 24 mm thick Dyneema laminate. A 100·100 mm, 15 mm thick Alumina Ceramic tile is bonded to the laminate by an adhesive. The free surface of the tile is covered by a 2 mm Al-plate (7075), bonded to the tile (Figure 3). The total thickness of the specimen was 42 mm, as the thickness of the adhesive were 1 mm for each layer.

In order to simulate the confinement from neighbouring tiles, a steel frame surrounds the tile. The frame is made of steel bars (20 x 15 mm rectangular cross section) bolted together in the corners and bonded to both the laminate and the tile. A few of the frame bars had a window, through which the side of the tile could be observed. Four specimens without the retaining steel frame were tested for reference purposes.

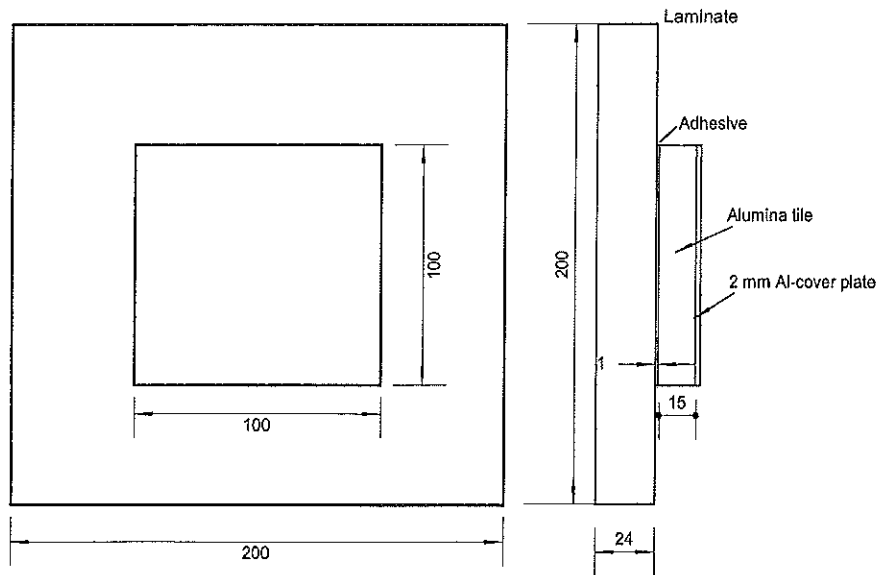


**Figure 3.** *Specimens for alumina damage.*

## TESTS

A total of 15 specimens were tested, and specimens without the retaining steel frame are marked with grey coloured rows in Table 1.

Specimen n°	Mass (kg)	Height (m)	Nominal energy (J)
1	5.8	0.5	28
2	21.8	0.4	85
3	5.8	1.5	85
4	9.8	1.0	96
5	9.8	1.0	96
6	13.8	0.71	96
7	9.8	1.21	115
8	13.8	0.85	115
9	13.8	1.0	135
10	17.8	1.0	175
11	21.8	1.5	320
12	9.8	1.0	96
13	13.8	0.71	96
14	13.8	1.0	135
15	17.8	1.0	175

**Table 1.** *Specification of specimen test parameters.*

The incoming energy increases from about 30 J up to 300 J. Moreover, for 85, 96 and 115 J we considered different couples mass – velocity for each energy value in order to investigate its influence on the failure of the specimen.

## TEST RESULTS

The measured data (Table 2) has initially been evaluated and visualised by plotting the measured parameters (force, acceleration, impactor movement and backside deflection) as function of time.

Specimen n°	Nominal Energy (J)	Measured Energy (J)	Nominal Velocity (m/s)	Measured Velocity (m/s)	Ceramic Failure	Max Force (kN)	Max Def (mm)
1	28	26	3.1	3.0	No	11.7	1.17
2	85	75	2.8	2.6	No	41.8	2.0
3	85	-	5.4	-	No	-	-
4	96	91	4.4	4.3	No	38.4	2.7
5	96	87	4.4	4.2	No	36.7	2.36
6	96	85	3.7	3.5	Yes	37.6	4.1
7	115	109	4.9	4.7	Yes	43.4	4.3
8	115	113	4.1	4.0	Yes	43.9	4.5
9	135	123	4.4	4.2	Yes	42.1	5.7
10	175	163	4.4	4.3	Yes	49.6	7.36
11	320	298	5.4	5.2	Yes	40.8	11.8
12	96	89	4.4	4.3	No	13.2	2.2
13	96	87	3.7	3.6	Yes	13.2	4.2
14	135	107	4.4	3.9	Yes	19.4	7.0
15	175	173	4.4	4.4	Yes	42.2	7.9

**Table 2.** Measured parameters.

For the force and displacements, two types of behaviour are observed (Figure 4):

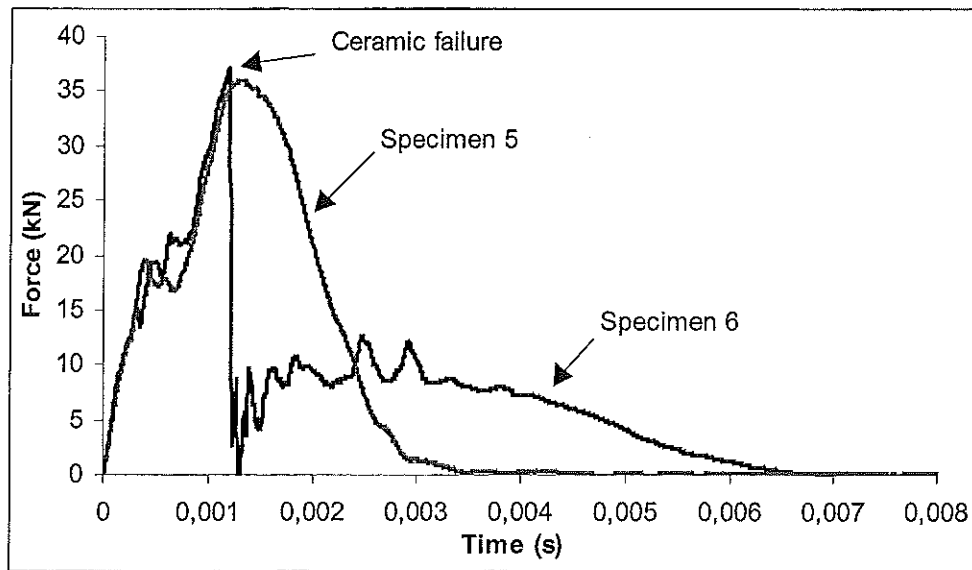


**Figure 4.** Force as function of time for specimen 5 and 6.

The curve for specimen 6 in Figure 4 shows a large fall for the value of the force after about 1.3 ms. The analysis of this specimen after the test gives that the ceramic tile breaks into several parts, Figure 5, and the only the laminate will absorb the remaining impact energy. It is why the curve seems to be the addition of two different behaviours.

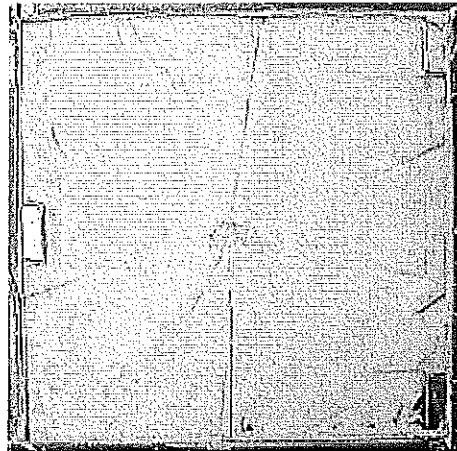


Figure 5. Failed tile for specimen 6.

The specimen 5 was tested with about the same nominal energy (96 J) but its curve shows that no failure occurred. Consequently, the value of about 100 J is probably a threshold for the failure of the ceramic because this part of the composite breaks for all the specimen tested with a larger energy.

Moreover, the measured contact duration is different according to the mechanical parameter that we take into account. The contact duration calculated from the force is for the specimen 6 about 6.5 ms against 12.5 ms (x 1.9) from the out-of-plane displacement (Figure 6). The difference is less for the specimen 5 : 3.5 ms from the force and 4.5 ms (x 1.3) from the displacement. But in this case the ceramic layer didn't fail.

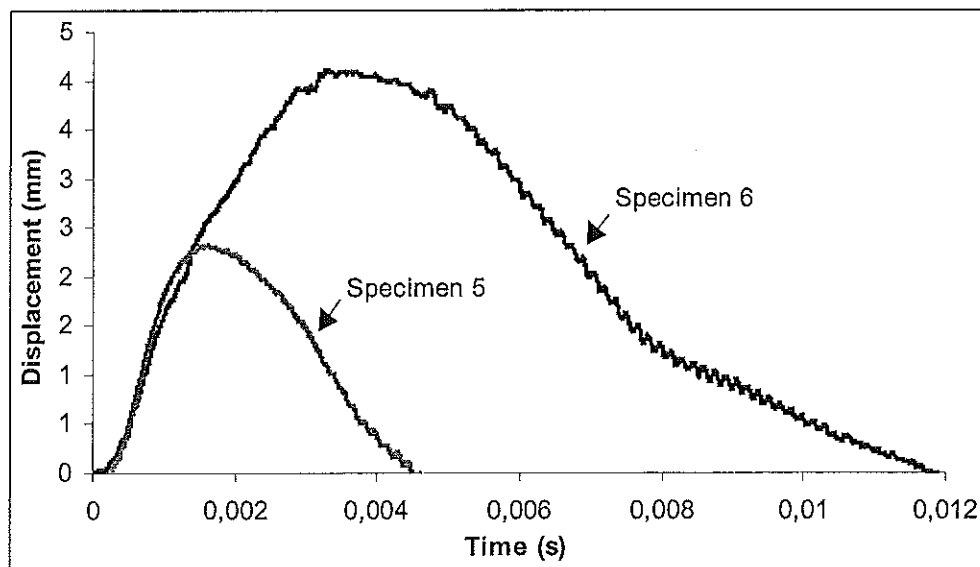
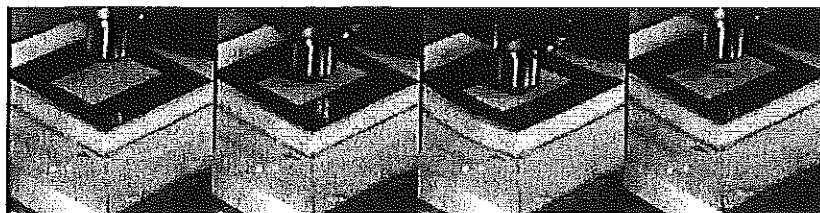


Figure 6. Out-of-plane displacement as function of time for specimen 5 and 6.

For the specimen 6 the significant difference could be attributed to the flexural stiffness which changes during the contact duration because of the failure of the alumina layer (Figure 7).



**Figure 7.** Impact sequence for specimen 15 17.8 kg, 4.4 m/s, 175 J from the high speed camera.

The failure of the ceramic as observed through the window in the support frame is shown in Figure 8 for specimen 11. In the first four pictures, which is in sequence with a time distance of 0.25 ms, the impactor penetrates into the coverplate, and the failure in the ceramic surface can be observed in picture no. 2. The two last images is 10 and 12 ms after no. 4. The plate is nearly unloaded in the second last picture.

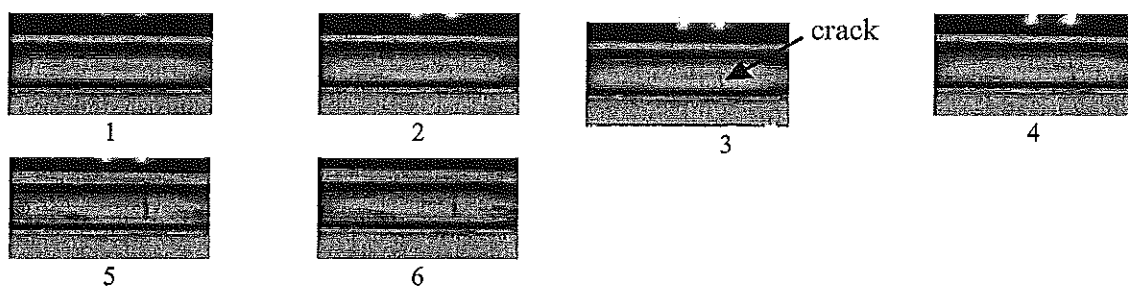


**Figure 8.** Failure sequence of ceramic as observed through the window in the steel frame, specimen 11. The contour of the impactor head is visible in image 3-5.

Although the flexural stiffness of the plate is important it is possible to observe a significant local deflection of the backside (Figure 9).

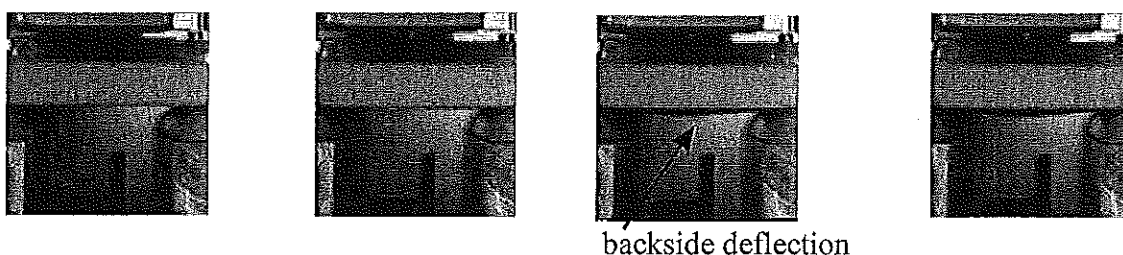


**Figure 9.** The support plate center deformations as observed for specimen 10. Time distance between images is 2 ms.

An analysis of the data shows that the ceramic failure occurs about for the same value of the out-of-plane displacement of the plate (2.0 mm). The value of the force is more scattered (Table 3) but always greater than about 40 kN.

Specimen n°	Measured Energy (J)	Failure Force (kN)	Failure Displacement (mm)
7	109	43.45	2.0
8	113	43.88	2.0
9	123	41.86	2.0
10	163	48.62	2.1
11	298	40.83	1.7
<b>Mean</b>		<b>43.73</b>	<b>2.0</b>
13	87	41.64	2.4
14	107	43.54	2.6
15	173	42.20	2.2
<b>Mean</b>		<b>42.46</b>	<b>2.4</b>

**Table 3.** Force and displacement for the alumina failure.

For the specimens which have no failure of the alumina layer the maximum displacement is close to the failed specimens but the maximum force is less (38 kN) (Table 4).

Specimen n°	Measured Energy (J)	Maximum Force (kN)	Maximum Displacement (mm)
1	26	11.52	1.1
4	92	38.07	2.2
5	87	36.18	2.3
12	89	33.50	2.1

**Table 4.** Maximal force and displacement for the specimens with no failure.

A vibratory analysis has been done on the curve force as function of time. The visible undulations (Figure 4) give interesting information on the vibratory response of the system : specimen - boundaries conditions - impact testing machine (Figure 10). This vibratory response (Figure 10-2 and 5) is obtained by subtracting the measured signal and the filtered one. Then, a Fourier analysis gives the frequencies spectrum.

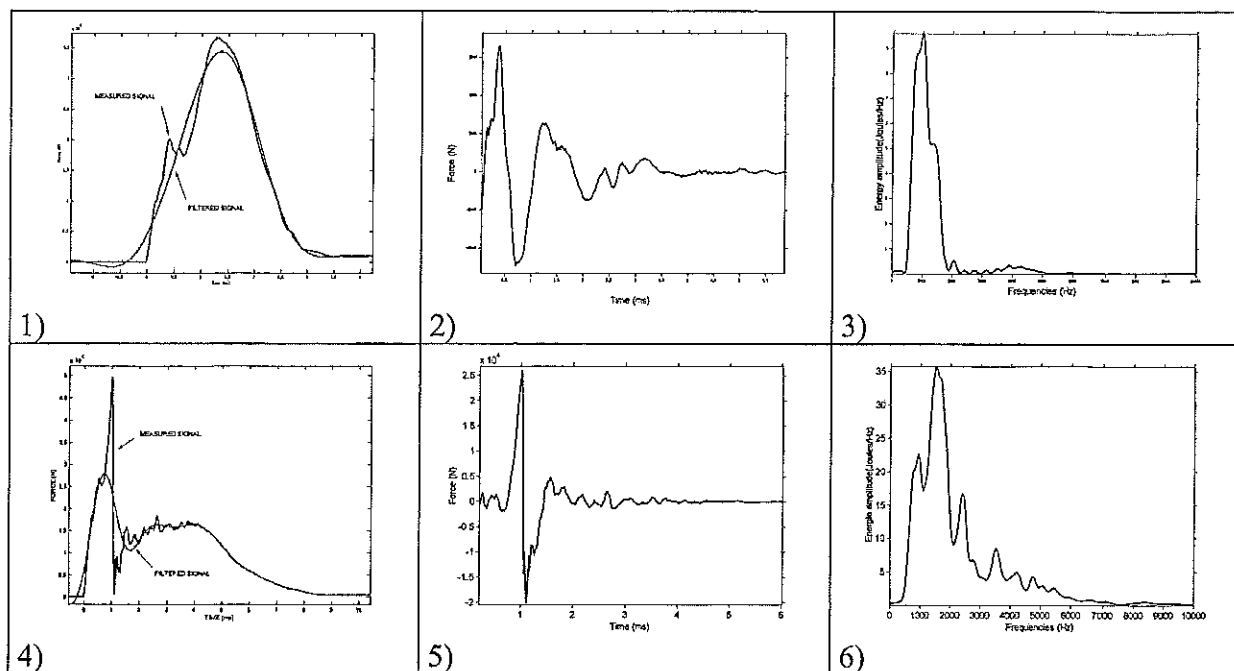


**Figure 10.** Frequencies spectrum for the specimen 5 (1 to 3) and 10 (4 to 6).

The vibratory response of the specimen 5 has two main frequencies : 1022 et 1401 Hz, for the specimen 10 there are four frequencies : 921, 1580, 2390 and 3497 Hz.

## CONCLUSION

The force as function of time shows two kinds of behaviour. The first one exhibits a failure of the ceramic layer and the value of the maximum force is greater than 40kN for a 2 mm out-of-plane displacement. The second one where no failure is immediate visible. A energy threshold is determined for the failure of the alumina layer for about 100J.

The contact duration between the impactor and the specimen measured from the force and the out-of-plane displacement is different suggesting a complex behaviour because of the materials and the failure of the ceramic layer.

# NONLINEAR ASPECTS OF DYNAMIC FRACTURE IN GLASSES AND CERAMICS

O. B. Naimark and J.-L. Lataillade

Institute of Continuous Media Mechanics, Russian Academy of Sciences, Russia  
LAMEFIP-ENSAM, University Bordeaux 1, France

## ABSTRACT

The nonlinear dynamics of failure in glasses and ceramics is discussed in the linkage with collective properties of mesodefekt ensemble (microcracks, microshears). The role of specific collective modes in defect ensemble in the transition from the steady state to the branching regime of crack dynamics, fragmentation, the excitation of failure wave in shocked brittle materials are studied experimentally and theoretically.

## 1. INTRODUCTION

Brittle materials such as monolithic ceramics, glasses are finding increasing applications. Certain types of ceramics exhibit some of highest strength properties measured in engineering materials. Limited plastic slip systems in these materials preclude plastic flow at low stress levels and dynamic strength approaches an appreciable fraction of the theoretical strength. There is a need to design these materials for the resistance to dynamic and impact loading. An understanding of damage evolution under dynamic loading conditions is important in the analysis of structures made of brittle materials [1]. Failure of ceramics and glasses under compression occurs at strains on the order of less than 1-2 %. From mechanical point of view the compressive failure of ceramics and glasses is closely related to the problem of sliding microcracks nucleating tensile wing cracks.

However, the post yield dynamic strength characteristics of typical ceramics (for instance for boron carbide and silicon carbide, which exhibit comparable high Hugoniot elastic limits) exhibit markedly different behavior [2]. The specific feature in the velocity interferometry data is observed. Profiles for silicon carbide are smooth and regular whereas corresponding profiles for boron carbide show an erratic and irregular component. The VISAR data at various spatial scales corresponding to irregular behavior show heterogeneous motion on the mesoscale that was indicated as random elastic wavelets from nearby points removed from the laser spot [3]. Past investigations have shown that damage in the form of microcracking plays an important role in deformation and failure of ceramics and glasses at the stresses below the Hugoniot elastic limit (HEL) under dynamic loading conditions. A dominant mechanism that commonly characterizes damage in brittle materials is microcracking which may nucleate at inhomogeneities such as pores, inclusions, second phase particles, twin/grain boundary intersections and triple point grain boundary junctions [4]. Above some critical strain rate which is typically in the order  $10^3 \text{ s}^{-1}$  most ceramic materials exhibit a strong strain rate sensitivity. It has been found [5] that the strain rate sensitivity exponent is nearly the same for all ceramics (around 0.27). The crack initiation has been considered as to be athermal. After the nucleation of crack the rate controlling process is considered to be inertia which is suggested to be

independent of material properties. This inertia effect was linked in [6] with initiation and propagation of cracks.

This situation has pronounced features for dynamic and shock wave loading, when the internal time of the ensemble evolution is approaching to the characteristic loading time. As the consequence, the widely used assumption in phenomenology of plasticity and failure concerning the subjective role of structural variables to stress-strain variables (adiabatic limit) can not be generally applied. However, in this case another fundamental problem arises concerning description of the defect ensemble behavior taking in view the multifield nature of the defect interaction and specific role of defects that could be considered in the continuum limit as the localized change of the symmetry and the global change of the system symmetry under the generation of new collective modes. The first change of the symmetry follows physically from the dislocation nature of defects (formally from the gauge field theory) and must be reflected in the corresponding structure of internal variables (the order parameters), the second symmetry change is the consequence of the group properties of the evolution equations for order parameter with specific non-linearity, which leads to the spatial-temporal localization in defect distribution and the generation of the structures responsible for new internal times, scales and finally scenarios of failure and plasticity. In this view the multifield theory of mesoscopic defects was developed in [7-9] and was applied for the explanation of the effects under dynamic crack propagation [10], structure of the shock waves [11], the delayed failure (failure waves) in shocked materials [12] and statistics of dynamic failure (dynamic fragmentation).

**Dynamic crack propagation.** The rebirth of interest in the issue of dynamic fracture is observed during last decade due to the variety of new experimental results which are not explainable within the prediction of classical fracture mechanics where it was shown [14] that the crack in infinite plane specimen has two steady-state velocities: zero and the Rayleigh speed. The recent experimental study revealed the limiting steady state crack velocity, a dynamical instability to microbranching [15,16], the formation of non-smooth fracture surface [17], and the sudden variation of fracture energy (dissipative losses) with a crack velocity [18]. This renewed interest was the motivation to study the interaction of defects at the crack tip area (process zone) with a moving crack. The still open problem in the crack evolution is the condition of crack arrest that is related to the question whether a crack velocity smoothly approaches to zero as the loads is decreased from large values to the Griffith point [19]. There is also problem at the low end of crack velocity. How a crack that is initially at rest might achieve its steady-state.

**Failure waves.** The materials with high strength or the high latent compressive stress (glasses, ceramics) exhibit the delayed failure, the so-called, failure wave. This phenomenon is the subject of intensive study during last two decades. The term "failure wave" was introduced in [20] as the limit case of damage evolution when the number of sliding microcracks (microshears) will be large enough for the determination of front with characteristic group velocity. Such a wave was considered in [21] where the concept of a wave of fracture was discussed to explain the nature of elastic limit. The existence of failure wave was established first in [22] by considering a small recompression signal in the VISAR record of the free surface velocity of K19 glass (similar to soda-lime). This recompression signal resulted from a release returning after reflection of the shock at the glass rear surface reflecting again in compression at the lower impedance failure front. Recent studies have suggested that a wave of failure propagates behind the elastic wave in glass with a velocity in the range 1.5-2.5 km/s. Failure wave appeared in shocked brittle materials (glasses, ceramics) as a particular failure mode in which they lose strength behind a propagating front. This front separates the structured material from the failed area. The important feature of failure wave phenomenon is that the velocity of failure wave doesn't depend on the velocity of propagation of the single crack

having the theoretical limit equals to the Rayleigh wave velocity. The stored elastic energy in material is the main factor, which provides the ability of brittle solid to the delayed failure. The high capacity of elastic energy in material can be created under the bulk compression or in the condition of loading providing the state close to the bulk compression, for instance, under impact loading. The necessity to provide the high capacity of elastic energy can be realized by the removal of surface defects or the structure homogenization. The brittle materials (glasses and ceramics) exhibit very high dynamic compressive strength, the Hugoniot elastic limits. For the glasses with high strength or the high latent compressive stress self-keeping failure can be observed not only for the compression but also for bending and tension.

Generally, the interest to the failure wave phenomenon is initiated by the still open problem of physical interpretation of traditionally used material characteristics as the Hugoniot elastic limits, dynamic strength, the relaxation mechanism of the elastic precursor. The phenomenon of failure wave could provide the information concerning the mechanisms of general rules of nucleation, growth of the multiple microdefects and will allow the interpretation of experiments with hard brittle materials like ceramics and rocks.

**Dynamic fragmentation.** Qualitative new features in the crack dynamics (transition from the steady state to the branching regimes and the fragmentation), the phenomenon of the delayed failure revealed specific features of dynamic failure that is the property of non-equilibrium system with nonlinear and stochastic behavior caused by the collective effects in defect ensemble. This allows us to develop the view on the dynamic fracture statistics (fragmentation problem) to link the nonlinear dynamic aspects of damage evolution with the change of the symmetry properties of system due to the generation of the collective modes in the defect ensemble.

Some basic theories have emerged within the past 10 years for predicting the consequences of dynamic fragmentation induced by high velocity impact or explosive events. These theories have focused on the prediction of mean fragment size through energy and momentum balance principles [23-26], and on statistical issues of fragment size distribution [27,28]. However, there are a number of unresolved issues within the development of statistical energy balance theories of fragmentation.

The dynamic fragmentation was analyzed in [29] on the approach based on local energy inequality and minimum fracture time requirement. This theory was later modified in [25] to include the kinetic energy available for fragmentation. However, the theories are not complete because the evolution process that leads to the catastrophic failure of the materials was not considered.

## **2. MESODEFECT PROPERTIES**

Direct observation of material state showed the important role of collective properties of typical mesodefects (microcracks, microshears) and the influence of these defects on the damage evolution. The influence of the defects on the transition from damage to fracture was studied experimentally with the usage of the X-ray diffraction method, light microscopy, the precise measurement of material density change in the bulk of the loaded specimen [10].

The important features of the quasi-brittle fracture were established for the understanding of various stages of failure: damage, damage localization, crack nucleation and propagation. It was shown that microcracks in the quasi-brittle crystalline materials have the dislocation nature and represent the hollow nuclei of the dislocation pile-ups. The model representation of microcrack as dislocation pile-up allowed the estimation of the own microcrack energy [30]

$$E \approx \left[ \frac{G}{V_0} \ln \frac{R}{r_0} \right] s^2, \quad (1)$$

where  $G$  is the elastic shear modulus;  $s = B S_D$  is the penny-shape microcrack volume;  $\bar{B} = n\bar{b}$  is the total Burgers vector;  $S_D$  is the microcrack base;  $V_0 = \frac{4}{3}r_0^3$  is the volume of the defect nuclei,  $r_0$  is the characteristic size of the dislocation hollow (defect nuclei);  $R$  is the characteristic scale of the elastic field produced by microcrack. The estimation showed that the power of the dislocation pile-up is close to  $n \approx 20$  [31]. Two reasons are important for the dislocation representation of microcracks. The first one is the determination of the microcrack energy as the energy of the dislocation pile-up. The second reason is the determination of the microscopic parameter for the microcracks as the consequence of the symmetry change of the displacement field due to the microcrack nucleation and growth. The change of the diffeomorphous structure of the displacement field due to the defects has also important consequence from point of view of the symmetry change of the system "solid with defects". This symmetry aspect can be used to model the arbitrary defects both in crystalline and amorphous materials without the assumption concerning the dislocation nature of the defects that originally is the property of crystalline materials. The order parameters responsible for the defects can be introduced to follow the gage field theory [32] as the localization of the corresponding symmetry group of the distortion tensor.

### 3. COLLECTIVE PROPERTIES OF DEFECT ENSEMBLE

#### 3.1. Microscopic and macroscopic variables for defect ensemble

Structural parameters associated with typical mesoscopic defects (microcracks, microshears) were introduced in [7] as the derivative of the dislocation density tensor. These defects are described by symmetric tensors of the form  $s_{ik} = s v_i v_k$  in the case of microcracks and  $s_{ik} = 1/2s(v_i l_k + l_i v_k)$  for microshears. Here  $\vec{v}$  is unit vector normal to the base of a microcrack or slip plane of a microscopic shear;  $\vec{l}$  is a unit vector in the direction of shear;  $s$  is the volume of a microcrack or the shear intensity for a microscopic shear. The average of the "microscopic" tensor  $s_{ik}$  gives the macroscopic tensor of the microcrack or microshear density  $P_{ik} = n \langle s_{ik} \rangle$ , which coincides with the deformation caused by the defects,  $n$  is the defect concentration.

#### 3.2. Statistical self-similarity. Statistical model of elastic solid with defects

Study of the microcrack (microshear) size distribution for the different spatial scales revealed the self-similarity of the mesodefekt pattern, Fig.1. The statistical self-similarity reflects the invariant form of the distribution function for the mesodefekt of different structural levels. This fact has important consequence for the development of the statistical multifield theory of the defect ensemble evolution.

Statistics of the microcrack (microshear) ensemble was developed in the terms of the solution of the Fokker-Plank equation [8,9]

$$\frac{\partial}{\partial t} W = -\frac{\partial}{\partial s_{ik}} K_{ik} W + \frac{1}{2} Q \frac{\partial^2}{\partial s_{ik} \partial s_{ik}} W, \quad (2)$$

where  $K_{ik} = \frac{\partial E}{\partial s_{ik}}$ ,  $E$  is the energy of the defect; and  $Q$  is the correlator of the fluctuating forces. The parameter  $Q$  characterizes the mean value of the energy relief of the initial material structure (the energy of defect nuclei). According to the statistical self-similarity hypothesis the distribution function of defects can be represented in the form  $W = Z^{-1} \exp\left(-\frac{E}{Q}\right)$ , where  $Z$  is the normalization constant. As it follows from (2) the statistical properties of the defect ensemble can be described after the determination of the defect energy  $E$  and the dispersion properties of the system given by the value of  $Q$ .

In the term of the microscopic and macroscopic variables and according to the presentation of the mesodeflects as the dislocation pile-ups the energy of these defects can be written in the form

$$E = E_0 - H_{ik} s_{ik} + \alpha s_{ik}^2, \quad (3)$$

where the quadratic term represents the own energy of defects (1) and the term  $H_{ik} s_{ik}$  describes the interaction of the defects with the external stress  $\sigma_{ik}$  and with the ensemble of the defects in the mean field approximation:  $H_{ik} = \sigma_{ik} + \lambda p_{ik} = \sigma_{ik} + \lambda n \langle s_{ik} \rangle$ , where  $\alpha, \lambda$  are the material constants. The average procedure gives the self-consistency equation for the determination of the defect density tensor

$$p_{ik} = n \int s_{ik} W(s, \vec{v}, \vec{l}) ds_{ik}. \quad (4)$$

For the dimensionless variables  $\hat{p}_{ik} = \frac{1}{n} \sqrt{\frac{\alpha}{Q}} p_{ik}$ ,  $\hat{s}_{ik} = \sqrt{\frac{\alpha}{Q}} s_{ik}$ ,  $\hat{\sigma}_{ik} = \frac{\sigma_{ik}}{\sqrt{Q\alpha}}$  self-consistency equation has the form

$$\hat{p}_{ik} = \int \hat{s}_{ik} Z^{-1} \exp\left(\left(\hat{\sigma}_{ik} + \frac{1}{\delta} \hat{p}_{ik}\right) \hat{s}_{ik} - \hat{s}_{ik}^2\right) d\hat{s}_{ik}, \quad (5)$$

that includes the single dimensionless material parameter  $\delta = \frac{\alpha}{\lambda n}$ . The dimension analysis allowed us to estimate that

$$\alpha \sim \frac{G}{V_0}, \quad \lambda \sim G, \quad n \sim R^{-3}.$$

Here  $G$  is the elastic modulus,  $V_0 \sim r_0^3$  is the defect nuclei volume,  $R$  is the distance between defects. Finally we obtain for  $\delta$  the value  $\delta \sim \left(\frac{R}{r_0}\right)^3$  that is in the correspondence with the hypothesis concerning the statistical self-similarity of the defect distribution on the different structural level. The solution of the self-consistency equation (5) was found for the case of the uni-axial tension and simple shear [9], (Fig.1).

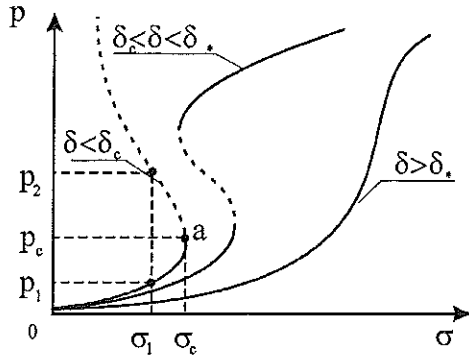


Fig. 1. Characteristic responses of materials on defect growth.

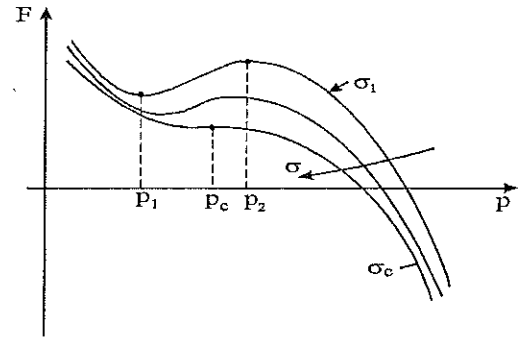


Fig. 2. Free energy dependence on stress and defect density for  $\delta < \delta_c \approx 1$ .

The existence of characteristic nonlinear behavior of the defect ensemble in the corresponding ranges of  $\delta$  ( $\delta > \delta_* \approx 1.3$ ,  $\delta_c < \delta < \delta_*$ ,  $\delta < \delta_c \approx 1$ ) was established, where  $\delta_c$  and  $\delta_*$  are the bifurcation points. It was shown [9,10] that the range  $\delta < \delta_c \approx 1$  is characteristic for the quasi-brittle failure and the form of the free energy  $F$  for the nonlinear system “elastic solids with defects” corresponds to the form predicted by Fraenkel [33] for  $\sigma < \sigma_c$  (Fig.2).

The metastability for the stress  $\sigma < \sigma_c$  is the consequence of the orientation interaction in the defect ensemble. The free energy form, that was predicted by the statistical model, approaches to the Griffith form [34] with the growth of the applied stress (Fig. 2). It is the consequence of the nucleation of the defects with more pronounced orientation mode induced by the applied stress.

### 3.3. Phenomenology of failure. Free energy

The statistical description allowed us to propose the phenomenology of solid with defects based on the appropriate presentation of the free energy form  $F$ . Taking in view that Eqn.5 corresponds to the equation  $\frac{\partial F}{\partial p} = 0$ , the simple phenomenological form of the part of the free energy caused by defects (for the uni-axial case  $p = p_{xx}$ ,  $\sigma = \sigma_{xx}$ ,  $\varepsilon = \varepsilon_{xx}$ ) is given by the six order expansion which is similar to the well-known Ginzburg-Landau expansion [35].

$$F = \frac{1}{2} A (1 - \delta/\delta_*) p^2 - \frac{1}{4} B p^4 + \frac{1}{6} C (1 - \delta/\delta_c) p^6 - D \sigma p + \chi (\nabla_1 p)^2. \quad (6)$$

The bifurcation points  $\delta_*$ ,  $\delta_c$  play the role that is similar to the characteristic temperatures in the Ginzburg-Landau expansion in the phase transition theory. The gradient term in (7) describes the non-local interaction in the defect ensemble in the so-called long wave approximation;  $A, B, C, D$  and  $\chi$  are the phenomenological parameters.

### 3.4. Damage kinetics in quasi-brittle failure

The damage kinetics in quasi-brittle materials is determined by the evolution inequality [8]

$$\frac{\delta F}{\delta t} = \frac{\delta F}{\delta p} \frac{dp}{dt} \leq 0$$

that leads to the kinetic equation for the defect density tensor

$$\frac{dp}{dt} = -\Gamma \left( A \left(1 - \frac{\delta}{\delta_*}\right) p - B p^3 + C \left(1 - \frac{\delta}{\delta_c}\right) p^5 - D \sigma - \frac{\partial}{\partial x_i} \left( \chi \frac{\partial p}{\partial x_i} \right) \right), \quad (7)$$

where  $\Gamma$  is the kinetic coefficient.

Kinetic equation (7) and the equation for the total deformation

$$\varepsilon = \hat{C} \sigma + p$$

( $\hat{C}$  is the component of the elastic compliance tensor) represent the system of the constitutive equations of quasi-brittle materials with considered types of the defects.

### 3.5. Self-similar solutions. Damage localization

Transitions through the bifurcation points  $\delta_c$  and  $\delta_*$  lead to a sharp change in the symmetry of the system under the appearance of some characteristic collective modes in the defect ensemble. These modes are the consequence of the specific non-linearity, the group properties of the equation (7) in the corresponding ranges of  $\delta$  ( $\delta > \delta_*$ ,  $\delta_c < \delta < \delta_*$ ,  $\delta < \delta_c$ ). The qualitative relationships governing the changes in the behavior of the system are reflected in Fig.3 in the families of heteroclines, which are solutions of equation

$$A \left(1 - \frac{\delta}{\delta_*}\right) p + B p^3 - C \left(1 - \frac{\delta}{\delta_c}\right) p^5 + D \sigma + \frac{\partial}{\partial x} \left( \chi \frac{\partial p}{\partial x} \right) = 0. \quad (8)$$

In the region  $\delta > \delta_*$ , this equation is of the elliptic type with periodic solutions with spatial scale  $\Lambda$  and possesses  $p_{ik}$  anisotropy determined mainly by the applied stress. As  $\delta \rightarrow \delta_*$  (separatrix  $S_2$ ) the periodic solution transforms into a solitary-wave solution  $p(x - Vt)$ , where  $V$  is the front velocity, and a formation of the area  $\Lambda \approx -\ln(\delta - \delta_*)$  with pronounced orientation mode of the defects (adiabatic shear bands).

As  $\delta \rightarrow \delta_*$  Eq. (8) changes locally from elliptic to hyperbolic (separatrix  $S_2$ ), and the periodic solution transforms into a solitary-wave solution. This transition is accompanied by divergence of the inner scale  $\Lambda: \Lambda \approx -\ln(\delta - \delta_*)$ . In this case the solution has the form  $p(\zeta) = p(x - Vt)$ .

The wave amplitude and velocity and the width of the wave front are determined by the parameters of nonequilibrium (orientational) transition:

$$p = \frac{1}{2} p_a [1 - \tanh(\zeta l^{-1})], \quad l = \frac{4}{p_a} \left( 2 \frac{\chi}{A} \right)^{1/2}. \quad (9)$$

The velocity of the solitary wave is  $V = \chi A(p_a - p_m)/(2\zeta^2)$ , where  $p_a - p_m$  is the jump in  $p$  in the course of an orientational transition. A transition through the bifurcation point  $\delta_c$  (separatrix  $S_3$ ) is accompanied by the appearance of spatio-temporal structures of a qualitatively new type characterized by explosive accumulation of defects as  $t \rightarrow t_c$  in the spectrum of spatial scales (peak regime of damage localisation) [9].

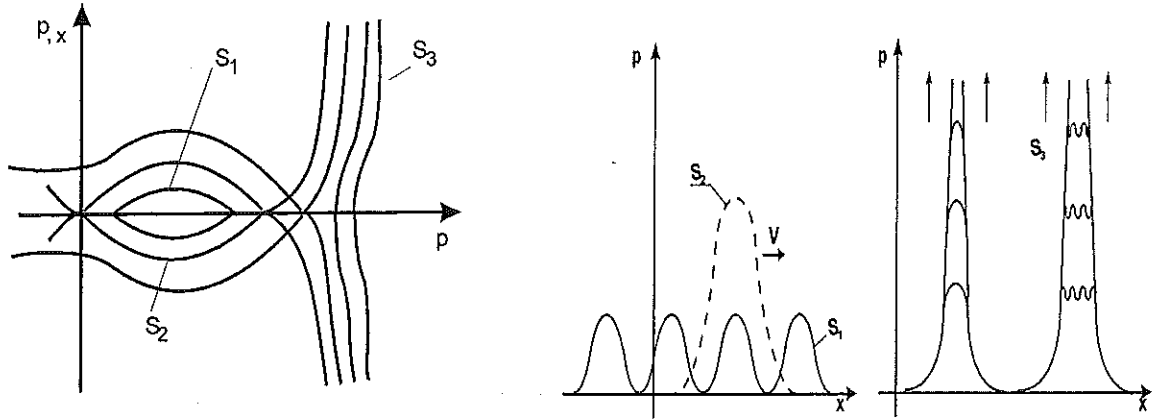


Fig.3. Types of heteroclines and the corresponding characteristic forms

At the approaching of stress to the critical value  $\sigma_c$  ( $p \rightarrow p_c$ ) the damage kinetics is subject to specific spatial-temporal structures, which appear in the defect ensemble in the course of the interaction between defects [10]. The subjection of damage kinetics to these structures reflects the qualitative change of the system symmetry due to the reduction of the number of independent coordinates in the damage field. The spatial-temporal structures are given by the self-similar solution of the kinetic equation (7) under the pass of the critical point  $p_c$  and reads

$$p(x,t) = \phi(t)f(\zeta), \quad \zeta = x/L_c, \quad \phi(t) = \Phi_0 \left(1 - \frac{t}{t_c}\right)^{-m}, \quad (10)$$

where  $m > 0$ ,  $\Phi_0 > 0$  are the parameters related to the nonlinear form of Eqn.7;  $L_c$  and  $t_c$  are the scaling parameters which can be found under the solution of the corresponding nonlinear eigen-function problem. The self-similar solution (10) describes the blow-up damage kinetics for  $t \rightarrow t_c$  on the set of the spatial scales  $L_H = kL_c$ ,  $k = 1, 2, \dots, K$  [36]. The loss of metastability of the free energy under  $\sigma \rightarrow \sigma_c$  (Fig.3) leads to the qualitative change of the general property of the system including the symmetry properties. In the area  $\sigma > \sigma_c$  the stress field doesn't control the system behavior and the failure scenario is determined by the generation of the blow-up damage localization structures in the process zone.

## 4. DYNAMIC CRACK INSTABILITY

### 4.1. Limited crack velocity

Theoretical explanation of the limited steady-state crack velocity and the transition to branching regime was proposed in [10] due to the study of collective behavior of the microcrack ensemble in the process zone. It was shown by the solution of evolution equation for the defect density tensor that the kinetics of microcracks accumulation at the final damage stage includes the generation of spatial-temporal structures (dissipative structures) with blow-up damage kinetics that is the precursor of the nucleation of the "daughter" cracks.

The kinetics of damage localization is determined by two parameters, which are given by the self-similar solution (10). These parameters are the spatial scales  $L_C$  of the blow-up damage localization and the so-called "peak time"  $t_c$ , which is the time of damage localization in the self-similar blow-up regime. The velocity limit  $V_C$  of the transition from the steady-state to the irregular crack propagation is given by the ratio:  $V_C \approx L_C/t_c$ . The steady-state crack propagation is realized in the case when the stress rise in the process zone provides the failure time  $t_f > t_c = L_C/V_C$  for the creation of the daughter crack only in the straight crack path. The failure time  $t_f$  follows from the kinetic equation (7) and represents the sum of the induction time  $t_i$  (the time of the approaching of the defect distribution to the self-similar profile on the  $L_H$  scale) and the peak time  $t_c$ :  $t_f = t_i + t_c$ . For the velocity  $V < V_C$  the induction time  $t_i \gg t_c$  and the daughter crack appears only along the initial main crack orientation. For the crack velocity  $V \approx V_C$  there is a transient regime ( $t_i \approx t_c$ ) of the creation of number of the localization scales (daughter cracks) in the main crack path. The crack velocity growth in the area  $V > V_C$  leads to the sharp decrease of the induction time  $t_i \rightarrow 0$ ,  $t_f \rightarrow t_c$  that is accompanied by the extension of the process zone in both (tangent and longitudinal) directions where the multiple blow-up structures (daughter cracks) and, as the consequence, the main crack branching appears. The set of the dissipative structures localized on spatial scales  $L_H$  (daughter crack sizes), represents new set of independent coordinates (collective modes of the defect ensemble) of the nonlinear system for  $\sigma > \sigma_c$ . These coordinates characterize the property of second attractor that could subject the behavior of nonlinear system. The first attractor corresponds to the well known self-similar solution for the stress distribution at the crack tip (that is the background for the stress intensity factor conception). This solution is available in the presence of the metastability (local minimum) for  $p$  in the range  $\sigma < \sigma_c$ .

### 4.2. Experimental study

Direct experimental study of crack dynamics in the PMMA plane specimen was carried out with the usage of high-speed digital camera Remix REM 100-8 (time lag between pictures  $10 \mu s$ ) coupled with photoelasticity method, Fig. 4 [37].

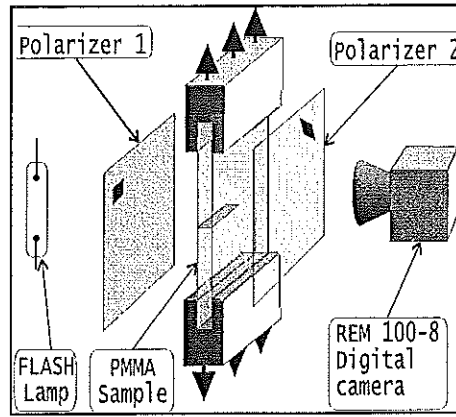


Fig. 4. Scheme of experiment

The experiment revealed that the pass of the critical velocity  $V_c$  is accompanied by the appearance of stress wave pattern produced by the daughter crack growth in the process zone. Independent estimation of critical velocity from the direct measurement of crack tip coordinates and from pronounced stress wave Doppler pattern gives the correspondence with the Fineberg data ( $V_c \approx 0.4V_R$ ) [16].

#### 4.3. Characteristic crack velocity

The pictures of stress distribution at the crack tip is shown in Fig.5 for slow ( $V < V_c$ ), fast ( $V > V_c$ ) and branching ( $V > V_B$ ) cracks.

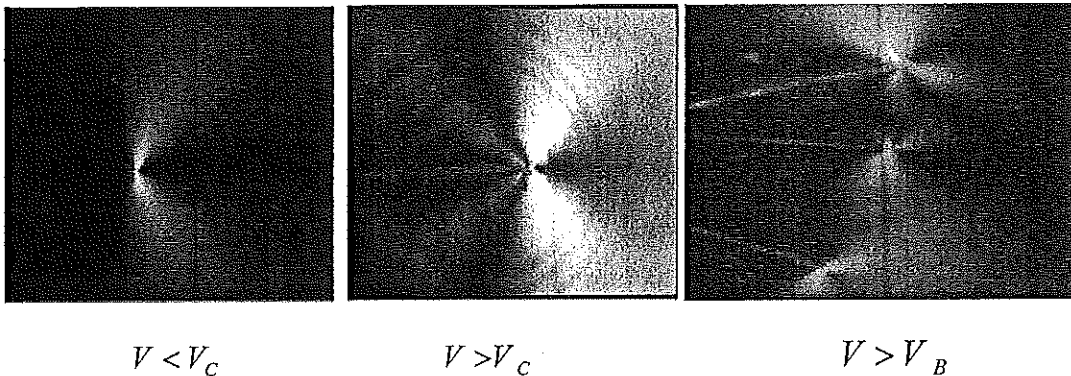


Fig. 5. Different regimes of crack dynamics.

The dependence of crack velocity on the initial stress is represented in Fig.6 and includes three characteristic portions. These portions determines three characteristic velocities: the velocity of the transition from the steady-state to the non-monotonic straight regime  $V_s \approx 220 \text{ m/s}$ , the transient velocity to the branching regime  $V_c \approx 330 \text{ m/s}$  and the velocity  $V_B \approx 600 \text{ m/s}$  when the branches behave autonomous. In our experiments the dependence of the density of the mirror zones  $N$  on the stress also were studied (Fig.7). The characteristic velocity  $V_c \approx 330 \text{ m/s}$  allowed the estimation of the peak time  $t_c$  to measure the size of the mirror zone  $L_c \approx 0.3 \text{ mm}$ :  $t_c = L_c / V_c \approx 1 \cdot 10^{-6} \text{ s}$ . This result allowed also the explanation of the linear dependence of the branch length on the crack velocity. Actually, since the failure time for

$V > V_c$  is approximately constant ( $t_f \approx t_c \approx 1\mu s$ ), there is unique way to increase the crack velocity to extend the size of the process zone. The crack velocity  $V$  is linked with the size of the process zone  $L_{PZ}$  by the ratio  $V = L_{PZ}/t_c$ .

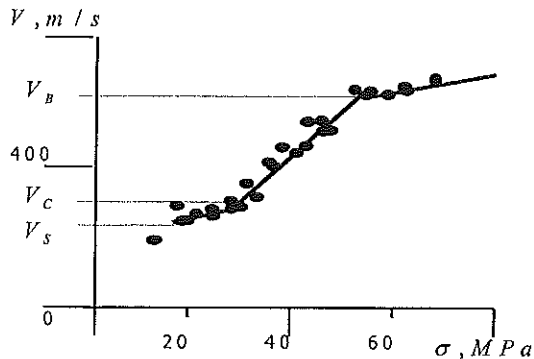


Fig. 6. Crack velocity via applied stress

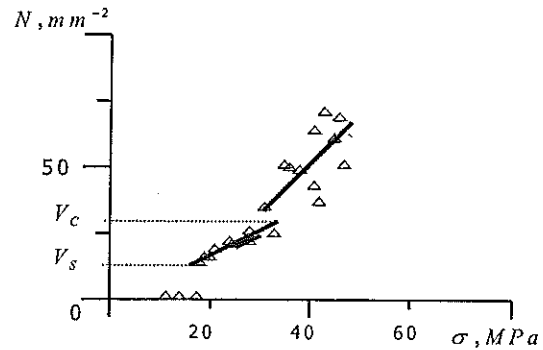


Fig. 7. Concentration of mirror zones

Since the branch length is limited by the size of the process zone, we obtain the linear dependence of branch length on the crack velocity. This fact explains the sharp dependence (quadratic law) of the energy dissipation on the crack velocity established in [38].

## 5. FAILURE WAVES

### 5.1. Failure wave as structural transition

Qualitative changes in silicate glasses behind the failure wave under the measure of the refractive index (refractive index increased) allowed Gibbons and Ahrens [39] to qualify this effect as the structural phase transformation. These results stimulated Clifton [40] to propose the phenomenological model in which the failure front was assumed to be a propagating phase boundary. According to this model the mechanism of failure wave nucleation and propagation results from local densification followed by shear failure around inhomogeneities triggered by the shock.

The description of failure wave phenomenon as the consequence of the generation of collective burst modes of mesodeflects was proposed in [11,12,41] in the course of study of non-equilibrium transition in defect ensemble. It was shown the existence of the self-similar solution for the microshear density tensor, which describes the qualitative changes in the microshear density kinetics in the course of the non-equilibrium transition. The failure waves represent the "blow-up" dissipative structures in the sliding microcrack ensemble that could be excited due to the pass of the elastic wave in the target. The progressive reduction in normal stress behind the failure wave was observed in [42], that allowed the conclusion about well-defined kinetics of inelastic process responsible for the reduction in shear strength.

### 5.2. Self-Similar Solution

Equation (4) describes the characteristic stages of damage evolution. In the range of stress  $\sigma < \sigma_c$  and the defect density  $p < p_c$  the damage kinetics is subject to the "thermodynamic branch"  $oa$  corresponding to the local minimum of the free energy (Fig.1,2). At the approaching

of stress to the critical value  $\sigma_c$  ( $p \rightarrow p_c$ ) the properties of the kinetic equation (4) change qualitatively (from elliptic to parabolic) and the damage kinetics is subject to specific spatial-temporal structures which appear in the defect ensemble in the course of the interaction between defects [9]. These structures describe the damage localization and the nucleation of the crack hotspots. Assuming the power law for the driving force  $\partial F/\partial p = S_0(p_c)p^q$  (free energy release) and the non-locality parameter  $\chi = \chi_0(p_c)p^\beta$  for  $p > p_c$  the kinetic equation for  $p$  can be written in the form:

$$\frac{\partial p}{\partial t} \approx S_0(p_c)p^q + \frac{\partial}{\partial x} \left( \chi_0(p_c)p^\beta \frac{\partial p}{\partial x} \right). \quad (11)$$

The spatial-temporal structures are given by the self-similar solution (10) of the kinetic equation (7) under the pass of the critical point  $p_c$ . The blow-up structures (10) describe the damage localisation kinetics on the spatial scales  $\xi_f$  given by the solution of corresponding eigen-value problem [36]. The value of  $\xi_f$  and the profile of  $f(\xi)$  allow us to define the law of propagation of failure front

$$x_f = \xi_f \chi_0^{1/2} S_0^{-\frac{q}{2(\beta-1)}} t^{\frac{\beta-q+1}{2(\beta-1)}} \quad (12)$$

as the dissipative structure localized on the scale  $x_f$  propagating with some group velocity.

Eqn. (12) gives three of self-similarity regimes depending on the relations between the parameters of the non-linear medium. If the stress level provides the nucleation of damage localization area with parameters  $\beta > q+1$  the failure wave front will propagate in the self-keeping regime.

### 5.3. Some Experimental Results

The blow-up kinetics of damage localization allowed us to link the hotspots of failure with the above mentioned self-similar structures. The correspondence of these hotspots having the image of the mirror zones to above self-similar structures was confirmed experimentally in [43,44]. The multiple mirror zones with an equal size were excited on different spall cross sections in the shocked PMMA cylindrical rod when the stress wave amplitude exceeded some critical value corresponding to the transition to the so-called "dynamic branch" under spalling (Fig. 8). The constant size of damage localization corresponds to the damage kinetics (free energy release rate) given by the following relationship between non-linearity parameters  $\beta \approx q+1$ .

The "dynamic branch" corresponds to the stress  $\sigma > \sigma_c$ , where the failure scenario is determined by the generation of the collective modes in defect ensemble in the form of the dissipative structure with the blow-up damage kinetics. The precursor of the delayed failure was established also in the experiment for dynamic crack propagation. The low rise of velocity for  $\sigma > 60 \text{ MPa}$  (Fig. 6) reflects the stress independent character of failure similar to the dynamic branch in spall experiment.

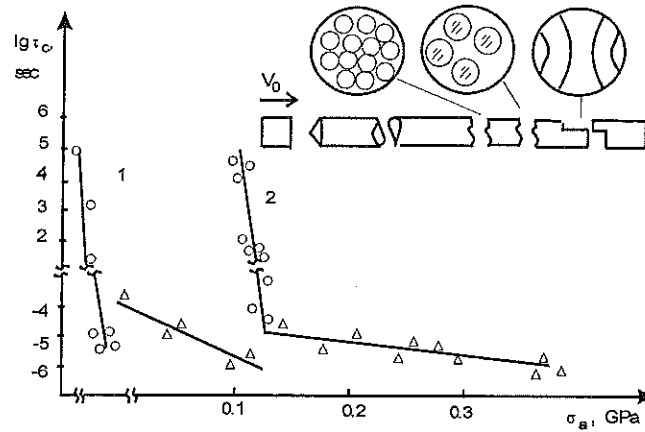


Fig. 8. Fracture time  $t_f$  for shocked rod of PMMA (1) and ultraporcelain (2) versus stress amplitude  $\sigma_a$ . Inset: surface pattern with mirror zones in different spall cross sections.

It is natural to assume that there is the ultimate energy densities in the process zone at the crack tip when the failure waves can be excited. These energy densities are created by the stress wave in above spall experiment and provide the resonance failure excitation (multiply mirror zone generation) on the set of spatial scales  $L_H \approx k L_C$  ( $k=1, 2 \dots N$ ) with the peak stress independent kinetics.

#### 5.4. Simulation of failure waves

The study of failure wave initiation and propagation was carried out on the basis of constitutive equation (4) coupled with momentum transfer equation.

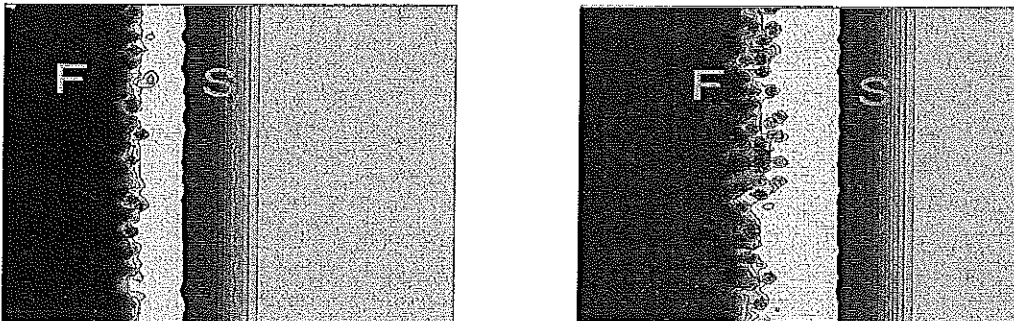


Fig. 9. Propagation of stress (S) and failure (F) waves.

The system of equations was solved using original finite element code [12]. The simulation confirmed spontaneous propagation of the failure front behind the stress wave front, Fig. 9. We observed also that the shear stress vanishes in the failure wave. The failure wave propagation leads to qualitative change in the transverse stress when this stress is approaching to the longitudinal stress level, Fig. 10.

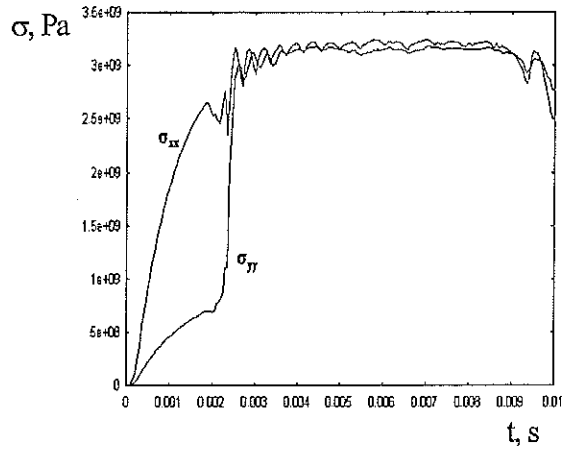


Fig. 10. Longitudinal  $\sigma_{xx}$  and transverse  $\sigma_{yy}$  stress kinetics.

## 6. DYNAMIC FRAGMENTATION

### 6.1. Scaling properties of failure.

The scaling properties of failure has spurred great interest in the context of the general problem of disordered media and multifield theory, when the self-affinity of the failure surface was established in the terms of the universality of the so-called the roughness exponent  $h(r) \propto r^\zeta$ ,  $\zeta \approx 0.8 \pm 0.05$  [45,46]. This fact allowed the determination of the length scales  $r > r_0$ , where the roughness exponent is the invariant. For the scales  $r < r_0$  the roughness exponent can change. The scale invariant properties for  $r > r_0$  means the transition from the roughness statistics caused by the initial structural heterogeneity (size of blocks, grains) to the statistics given by the collective properties of defects under transition from damage to fracture. In our experiments the roughness profile was determined for the PMMA fracture surface using the laser scanner system [10].

The processing of the roughness data in the term of the roughness exponent showed the dependence of the scaling properties on the regime of the crack propagation. The existence of different scaling indexes for another regimes of crack propagation reflects the variety of the behavior of investigated nonlinear system. As it was shown, the crack dynamics in the quasi-brittle materials is subject to two attractors. The first attractor is given by the intermediate asymptotic solution of the stress distribution at the crack tip. The self-similar solution (9) describes the blow-up damage kinetics on the set of spatial scales and determines the properties of the second attractor. This attractor controls the system behavior for  $V > V_B$  when there is the range of angles with  $\sigma > \sigma_c$ . The universality of the roughness index can be considered as the property of this attractor. In the transient regime  $V_B > V > V_C$  the influence of two attractors can appear. This reason can be considered as a mechanism of the dispersion of experimentally measured roughness on the scale  $r > r_0$ .

### 6.2. Experimental study of dynamic scaling

The scaling properties of failure as the symmetry properties of above mentioned attractors were studied under the recording of the stress dynamics (Fig. 9) using the polarization scheme coupled with the laser system [10], Fig. 11 .

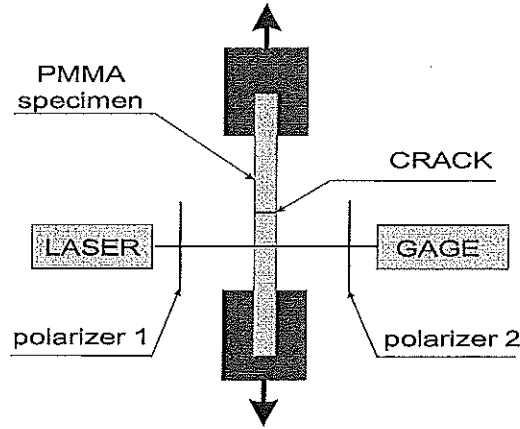


Fig. 11. Scheme of stress phase portrait recording

The stress temporal history was measured in the marked point deviated from the main crack path on the fixed (4 mm) distance. This allowed us to investigate the correlation property of the system using the stress phase portrait  $\dot{\sigma} \sim \sigma$  for slow and fast cracks, Fig.12. These portraits display the periodic stress dynamics that in the correspondence with the local ellipticity of Eqn.7 for  $\sigma < \sigma_c$  ( $V < V_c$ ) and the stochastic dynamics for  $V > V_c$  corresponding to the second type of the attractor. In the transient regime  $V \approx V_c$  the coexistence of two attractors can appear that can lead to the intermittency effect as the possible reason for the scaling index dispersion. The recording of the temporal stress history for  $V > V_c$  revealed the qualitative new structural changes in the process zone for the fast crack, Fig.14. The scaling properties as the above attractor properties were studied in the term of the correlation integral (Fig.13) calculated from the stress phase pattern using the formula

$$C(r) = \lim_{m \rightarrow \infty} \frac{1}{m^2} \sum_{i,j=1}^m H(r - |x_i - x_j|) \approx r^\nu,$$

where  $x_i, x_j$  are the coordinates of the points in the  $\dot{\sigma} \sim \sigma$  space,  $H(\dots)$  is the Heaviside function. The existence of the scales  $r > r_0$  with the stable correlation index was established for the regimes  $V < V_c$  and  $V_B > V > V_c$ .

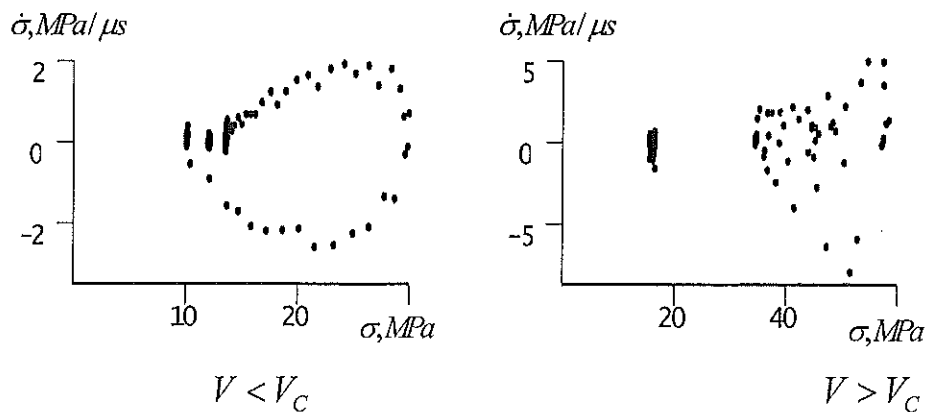


Fig. 12. Poincaré cross-sections

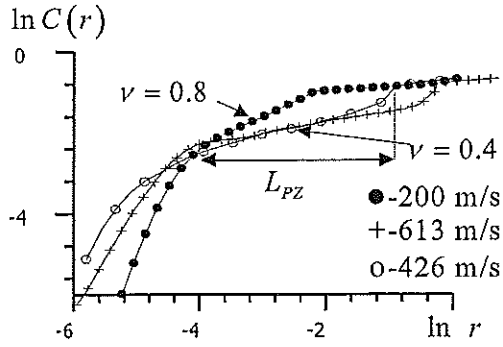


Fig. 13. Correlation integral

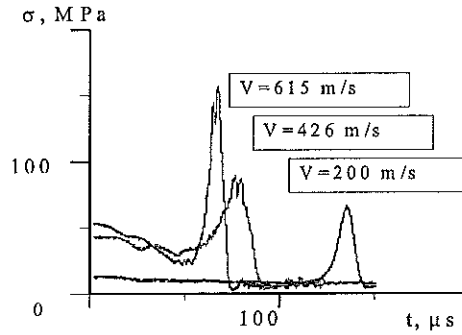


Fig. 14. The stress history

The values of the correlation indexes in these regimes show the existence of two scaling regimes with the deterministic ( $\nu \approx 1$ ) and stochastic ( $\nu \approx 0.4$ ) dynamics. The extension of the portions with a constant indexes determines the scale of the process zone  $L_{pz}$ . The length of the process zone increases with the growth of the crack velocity in the range  $V_B > V > V_C$  with the maintain of the scaling property of the dynamic system. Numerical simulation of the damage kinetics in the process zone allowed us to conclude that this scaling is the consequence of the subsection of the failure kinetics to the blow-up self-similar solution which determines the collective behavior of the defect ensemble in the process zone [13].

### 6.3. Fragmentation statistics

Taking in view the dramatic changes in the scaling properties of nonlinear system “solid with defects” due to the re-subjection of the system behavior to the collective modes of defects, the following scenario of the dynamic fragmentation can be discussed. The existence of characteristic stages of dynamic fracture under crack propagation (Fig.6) allowed us to establish the correlation of the dynamic fragmentation statistics with the energy density imparted to the material. The energy density  $E < E_C$  ( $E_C$  corresponds to the critical velocity  $V_C$  of the steady state – branching transition) provides the stress intensity controlled failure scenario. The transient densities  $E_B > E > E_C$  ( $V_C < V < V_B$ ) lead to the the fracture statistics that is sensitive to both self-similar solutions: the self-similar stress distribution at the crack tip and collective blow-up modes of damage localization. The intermittency effect, when the system reveals the complex statistics in the presence of two attractors, probably, has the phenomenological interpretation in the frame work of the Weibull statistics. Taking in view theoretically predicted low limit of damage localization scale  $L_C$ , it can be assumed the existence of critical energy density, which provides the limit size of fragmented structure close to  $L_C$ . Taking in view that these energy densities can be imparted in material generally by shock, this homogeneous fragmentation can be realized due to the failure wave excitation. The experiments in [47] with large specimens (optical glass K5 impacted by blunt steel cylinder) visualized the several fracture nucleation in the form of failure waves. Several spherical or nearby spherical waves were formed ahead of the main front.

## SUMMARY

The experimental data concerning the transition from the steady-state to the branching regime of dynamic crack propagation revealed the discrepancy in the prediction of the dynamic crack stability based on the stress intensity factor conception. The transition from the steady-state to the branching regime is the consequence of the subjection of the damage localization kinetics in the process zone at the crack tip to the self-similar solution corresponding to the blow-up regime of the damage localization that leads to the change of the symmetry properties of the system.

The scaling properties and the relaxation (dissipation) ability of material, the crack toughness can be linked with the scaling properties of the damage localization kinetics and the generation of collective blow-up modes in the defect ensemble. The resistance of materials to the dynamic crack propagation depends qualitatively on the collective properties of defect evolution in the process zone for  $V > 0.4 V_R$ .

Collective modes of the defect ensemble in the damage localization stage have the self-similar nature in the form of the blow-up dissipative structures with characteristic spatial-temporal scales. These modes could be excited in the resonance condition that could provide the anomalous failure responses (failure waves) in shocked glasses and ceramics.

The experiment in dynamic crack propagation allowed us to establish the qualitative changes in the statistics of dynamic failure that is in the correspondence with the theoretical prediction of the change of statistical properties of the system due to the generation of collective modes of the damage localization. The fragmentation statistics under intensive dynamic (shock wave) loading can be the consequence of these new statistical properties. The limit size of the fragments can be linked with the limit minimal scale of the damage localization in the self-similar blow-up regime.

This research was supported in part by the Russian Foundation of Basic Research (Grant 99-01-00244).

## REFERENCES

1. Ashby, M.F. and Hallam, S.D., The failure of brittle solids containing small cracks under compressive states, *Acta Metal.*, **34**, pp.497-510 (1986).
2. Grady, D.E., Shock wave properties of boron carbide and silicon carbide, *J. de Physique III*, **4**, pp. 385-391 (1994)
3. Mesherjakov, Yu.I., Atroshenko, S.A., Vasil'kov, V.B. and Chernushenko, A.I., Criteria of transition from translational to rotational motion of media under shock loading, In: *Shock Compression of Condensed Matter*, Elsevier, pp. 407-410 (1991)
4. Lankford, J., Compressive strength and microplasticity in polycrystalline alumina, *J. Mater. Sci.*, **12**, pp. 791-796 (1977)
5. Lankford, J., Mechanisms responsible for strain rate dependent compressive strength in ceramic materials, *J. Amer. Ceram. Soc.*, **64**, pp. C33-C34 (1981)
6. Grady, D.E. and Lipkin, J., Criteria for impulsive rock fracture, *Geophys. Res. Lett.*, **7**, pp. 255-258 (1980)
7. Naimark O.B., On thermodynamics of deformation and fracture of solids with microcracks. Preprint of Institute of Continuous Media Mechanics, USSR Academy of Sciences, Sverdlovsk (1982).

8. Naimark, O.B., Kinetic transitions in ensembles of microcracks and some nonlinear aspects of fracture, In: *Proceedings of the IUTAM Symposium on Nonlinear Analysis of Fracture* J.R. Willis (Ed). Kluwer Academic Publishers, Dordrecht, pp.285-298 (1997).
9. Naimark, O.B. , Defect induced instabilities, *JETP Letters*, **67**, 9, pp. 751-758 (1998)
10. Naimark, O.B., Collective behavior of crack and defects (plenary lecture), In: *Proceedings of EUROMAT 2000. Advances in Mechanical Behavior. Plasticity and Damage*, Eds. D Miannay, P.Costa, D. Francois, A.Pineau. Elsevier, 1, pp.15-28 (2000).
11. Naimark, O.B., Structural transitions in ensembles of defects as mechanisms of failure and plastic instability under impact loading, In: *Proceedings of IX Int. Conference of Fracture, Sydney*, Ed. B. Karihaloo, **6**, pp.2795-2806 (1997)
12. Plekhov, O.A., Eremeev, D.N. and Naimark, O.B., Failure waves as resonance excitation of collective burst modes of defects in shocked brittle materials, *J. Physique IV*, **10**, pp.811-816 (2000).
13. Naimark, O.B., Davydova, M.M. and Plekhov, O.A., Nonlinear and structural aspects of transitions from damage to fracture in composites and structures, *Computers and Structures*, Vol. 76, pp.67-75 (2000).
14. Freund, L.B., *Dynamic Fracture Mechanics*, Cambridge University Press, Cambridge, England (1990)
15. Fineberg, J., Gross, S., Marder, M. and Swinney, H.: Instability in dynamic fracture, *Phys.Rev.Lett.* **67**, pp.457-462 (1991).
16. Sharon, E., Gross, S.P. and Fineberg, J., Local crack branching as a mechanism for instability in dynamic fracture, *Phys.Rev.Lett.*, **74**, pp.5096-5099 (1995).
17. Boudet, J.F., Ciliberto, S. and Steinberg, V., Dynamics of cracks propagation in brittle materials, *J. de Physique*, **6**, pp.1493-1516 (1993).
18. Sharon, E., Gross, S.P., Fineberg, F., Energy dissipation in dynamic fracture, *Phys.Rev.Lett* , **76**, pp. 2117-2120 (1996) .
19. Holian, B.L., Thomson, R., Crack limiting velocity, *Phys. Rev.*, E, **56**, 1, pp. 1071-1079 (1997).
20. Galin, L.A. and Cherepanov, G.P., On self-keeping failure of stressed brittle solid, *Doklady AN SSSR*. **167**, pp. 543-548 (1966).
21. Nikolaevskii, V.N., Limit velocity of fracture front and dynamic strength of brittle solids, *Int. J. Engng. Sci.*, **19**, pp.41-56 (1981)
22. Rasorenov, S.V., Kanel, G.J., Fortov V.E. and Abasenov, M.M., The fracture of glass under high-pressure impulse loading, *High Pressure Research.*, **6**, pp.225-232 (1991).
23. Grady, D.E., Local inertia effects in dynamic fragmentation, *J. Appl. Phys.*, **53**, pp.322-325 (1982)
24. Kipp M.E. and Grady D.E., Dynamic fracture growth and interaction in one dimension, *J. Mech. Phys. Solids*, **33**, pp.399-415 (1986)
25. Glenn, L.A. and Chudnovsky, A., Strain energy effects on dynamic fragmentation, *J. Appl. Phys.*, **59**, pp. 1379-1380 (1986)
26. Grady, D.E., The spall strength in condensed matter, *J. Mech. Phys. Solids*, **36**, pp. 353-384 (1988)
27. Grady, D.E. and Kipp, M.E., Geometric statistics and dynamic fragmentation, *J. Appl. Phys.*, **58**(3), pp. 1210-1222, (1985)
28. Grady, D.E., Particle size statistics and dynamic fragmentation, *J. Appl. Phys.*, **68**, pp. 6099-61105 (1990)
29. Grady, D.E., Fragmentation under impulsive stress loading, *Fragmentation By Blasting* (edited by Fourney and Costin), Experimental Mechanics, Brookfield Center, pp. 63-72 (1985)

30. Betehtin, V.I, Naimark, O.B. and Silbershmidt, V.V., The fracture of solids with microcracks: experiment, statistical thermodynamics and constitutive equations. *Proceedings of Int. Conf. of Fracture (ICF 7)*, **6**, pp. 38-45 (1989)
31. Betehtin, V.I. and Vladimirov, V.I., Kinetics of damage of crystalline solid, In: *Problems of Strength and Plasticity of Solids*, Zhurkov, S.N. (Ed.). Nauka, Leningrad, pp.142-154 (1979)
32. Naimark O.B., Nanocrystalline state as atotopological transition in an ensemble of grain-boundary defects, *The Physics of Metals and Metallography*, **84**, 4, pp.327-337 (1997).
33. Frenkel, Ya.I., Theory of reversible and irreversible cracks in solid, *Journal of Technical Physics*, **22**, 11, pp.1857-1866 (1952)
34. Griffith, A.A., The phenomena of rupture and flow in solids, *Phil. Trans. of the Royal Society*, London, **A221**, pp.163-198 (1921).
35. Landau, L.D. and Lifshitz, E.M., *Course of Theoretical Physics. Statistical Physics*, Pergamon Press, Oxford (1980)
36. Kurdjumov, S.P., In: *Dissipative Structures and Chaos in Non-Linear Space*, Utopia, Singapore, **1**, pp.431-459 (1988).
37. Naimark, O.B., Davydova, M.M., Plekhov O.A. and Uvarov, S.V., Experimental and theoretical study of dynamic stochasticity and scaling under crack propagation, *Physical Mesomechanics*, **2**, 3, pp.47-58 (1999).
38. Fineberg, J., Gross, S.P. and Sharon, E., Microbranching and instability in dynamic fracture, In: *Proceedings of the IUTAM Symposium on Nonlinear Analysis of Fracture*, J.R. Willis (Ed). Kluwer Academic Publishers, Dordrecht, pp.177-189 (1997).
39. Gibbons, R.V., Ahrens, T.J., *J. Geophys. Res.* **76**, 5489. (1971)
40. Glifton, R.J., Analysis of failure waves in glasses, *Appl. Mech. Rev.* **46**, 540 (1993).
41. Naimark, O.B., Collombet, F. and Lataillade, J.-L., Super-deep penetration phenomena as resonance excitation of self-keeping spall failure in impacted materials, *J. de Physique III*, **7**, pp. 773-778 (1997)
42. Espinosa, H.D., Xu, Y. and Brar, N.S., Micromechanics of failure wave in glass, Part. 1: experiments. *J. Am. Cer. Soc.*, **80**(8), pp.2061-2073 (1997)
43. Beljaev, V.V. and Naimark O.B., Kinetics of multicenter fracture under shock wave loading, *Sov. Phys. Dokl.*, **312**, 2 pp. 289-293 (1990)
44. Bellendir, E., Beljaev, V.V. and Naimark, O.B., Kinetics of multicenter fracture under spalling conditions, *Sov. Tech. Phys. Lett.*, **15**, 3, pp. 90-94 (1989).
45. Bouchaud, E., Scaling properties of cracks, *J.Phys.: Condens. Matter*, **9**, pp.4319-4344 (1997).
46. Naimark, O.B., Davydova, M.M. and Plekhov, O.A., Failure scaling as multiscale instability in defect ensemble, In: *Proceedings of NATO Workshop "Probamat - 21 Century"*, G.Frantziskonis (Ed.). Kluwer, pp.127-142 (1998).
47. Senf, H., Strauburger, E. and Rothenhausler, H., Visualization of fracture nucleation during impact in glass. In: *Metallurgical and Material Applications of Shock Wave and High-Strain-Rate Phenomena*, Eds. L.E.Murr, K.P. Staudhammer and M.A. Meyers, pp.163-170, Elsevier Science B.V. (1995).

Cpt Beton (Klopaczko) } Concrète  
ref. R.P. Mechanics of Materials } Mortar

## Impact Analysis

à Delf barre Hopk verticale en tresse

Klep. barre  $\phi$  40 mm.

très forte sensibilité de la contrainte  
de rupture -  $\epsilon$  à 12 fois plus élevée  
que la statique -  $\epsilon$  de 1 à 100.0'

Voir aussi CEA

A. Bara et al Mechanics of Materials

33 (2001) 33-45.

Alan Ross (Univ. Florida)

Allen barre d'Hopk.  $\phi$  100 mm  
uniquement sur béton.

Int Journal of Impact Eng 24(2000) 985-998.

---

## Laitierade

- L'aspect visqueux est lié à la phase amorphe -

- la fragmentation dépend de  $\epsilon$ .

- Barre d'Hopk. si on mesure les ondes en 2 pb de  
la barre, les variations d'impédance peuvent  
être fracties.

- meilleure géométrie d'échantillon : le dia kolo (mais cher)

# Experimental and Numerical Approaches of the Quasi-Static and Dynamic Toughness of Two SiC Ceramics

Pascal Forquin,<sup>1</sup> Laurent Rota<sup>1</sup> and François Hild<sup>2</sup>

<sup>1</sup>DGA/CTA-Département Matériaux, Surfaces, Protection  
16 bis avenue Prieur de la Côte d'Or, F-94114 Arcueil Cedex, France.  
<sup>2</sup>LMT-Cachan, ENS de Cachan / CNRS-UMR 8535 / University Paris 6  
61 avenue du Président Wilson, F-94235 Cachan Cedex, France.

## Introduction

Over a few decades, the understanding and knowledge of ceramic toughness has improved significantly. Yet the techniques of toughness measurement are based on strong hypotheses. For example, the SENB (Single-Edge Notched Beam) method uses prenotched beams. The toughness associated with a notch may defer from that of a sharp crack. In particular, the measured value may be notch-radius-dependent. The indentation technique is also based on geometrical hypotheses concerning the crack shape. Consequently, methods for precracking brittle materials are investigated herein. Among the most promising methods, two of them are summarised: the BI (Bridge Indentation) method compresses a specimen sandwiched by a flat pusher and an anvil having a central groove. This technique was devised by Nunomura et al. [1] and used on ceramic materials by Tetsuro et al. [2]. The SB (sandwiched-beam) procedure is employed in the present work. This technique was first developed by Marshal et al. [3], Pancheri et al. [4] and used by Sglavo et al. [5] on ceramic materials. In this study, experimental and numerical investigations are performed on two silicon carbide grades to measure and predict their quasi-static and dynamic toughness.

## Properties of two silicon carbide grades

Two silicon carbide grades are examined. The first one, called S-SiC, is made by Céramiques & Composites (France) and is naturally sintered. The powders are pressed, then heated to 2000°C. This processing leads to a porosity of 1.8% [6] and thus induces sintering defects. These defects are visible on the fractured surface (Fig. 1a) of 3-point flexural experiments. As it can be seen on the micrograph, the material contains unmelt powders. The sintering process induces a low average strength (i.e., 370 MPa for an effective volume of 1.7 mm<sup>3</sup>) and a low Weibull modulus (i.e., 9.3 [8]).

The second grade, called SiC-N, is made by the US company CERCOM and is obtained by pressure assisted densification. The ceramic is heated to 2000°C under a pressure of about 20 MPa. An intergranular alumina phase eliminates the porosity. This homogenous microstructure gives a high strength compared to the previous grade when the material is loaded in 3-point flexure (i.e., 580 MPa for an effective volume of 2.5 mm<sup>3</sup>). The initiation location is found by following the hackles on the failure surface (Fig. 1b). A low Weibull modulus (i.e., 7.7) is obtained.

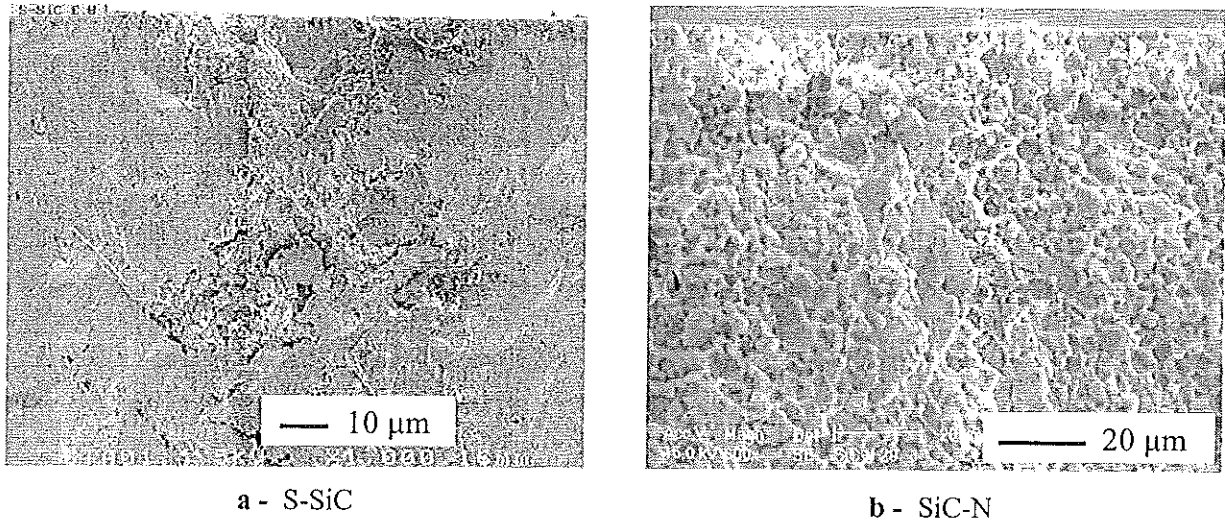


Fig. 1 – Failure location in 3-point flexure beams.

### Precracking S-SiC ceramics by using the sandwiched-beam technique

The aim of the present study is to analyse the toughness of the two SiC grades. Concerning the S-SiC grade, the SENB technique is chosen. This technique consists in performing a 3-point flexural test with precracked beams. To precrack S-SiC beams, the sandwiched-beam technique is used [5]. A through-thickness notched bar is inserted between two steel bars, and the assembly is loaded in a three-point flexural configuration (Fig. 2). The width (5 mm) and thickness (3 mm) of the ceramic beams were chosen to develop a sufficiently long crack compared to the thickness and to limit the rigidity of this bar with respect to the steel bars. Beam dimensions are summarised in Table 1.

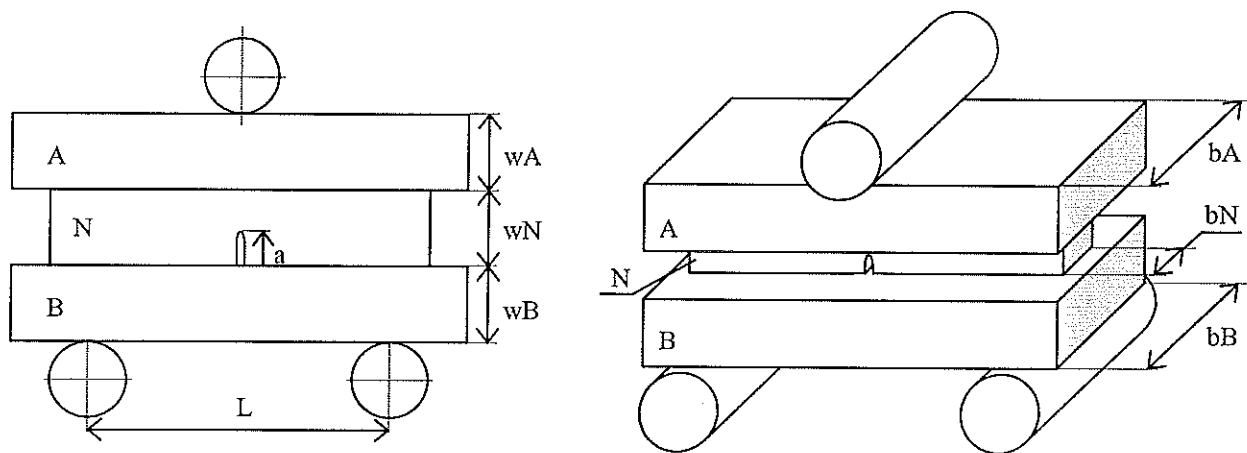


Fig. 2 – Schematic of the sandwiched-beam set-up.

Table 1. Dimensions for the sandwiched-beam set-up.

Beams	A	N	B
Materials	Steel	S-SiC	Steel
Height $w$ (mm)	5 ou 7	5	5.5
Thickness $b$ (mm)	9	3	9
Length (mm)	30	25	30
Young's Modulus (GPa)	210	410	210

Span length: 20 mm - Relative Prenotch Length:  $\alpha_0 = a_0/w \in [0.35, 0.45]$

The sandwiched-beam assembly permits to develop stable cracks for the following reason. The prenotched beam suffers a bending moment that is proportional to its flexural rigidity

$$M_n = M \frac{(EI)_n}{\sum_{i \in \{a, n, b\}} (EI)_i} \quad (1)$$

Therefore, when the crack length increases, the load applied to the ceramic bar decreases quickly. The stress intensity factor  $K$  can be written with the same equation used for the SENB test (single-edge notched beam) with an applied load  $P_n$

$$K = \left( \frac{P_n L}{b_n w_n^{1.5}} \right) f(\alpha) \quad (2)$$

The relative flexural rigidity of the cracked beam is a function of the relative crack length  $\alpha$  and  $r_0$

$$\frac{P_n}{P} = \frac{(EI)_n}{\sum_{i \in \{a, n, b\}} (EI)_i} = g \left( \alpha, r_0 = \frac{(EI)_a + (EI)_b}{(EI)_0} \right) \quad (3)$$

Figure 3 shows the change of the stress intensity factor with the relative crack length. When the curve is decaying, cracking is assumed to be stable. Consequently, relative prenotched lengths are always chosen greater than  $\alpha_{\text{critical}}$  (here equal to about 0.3).

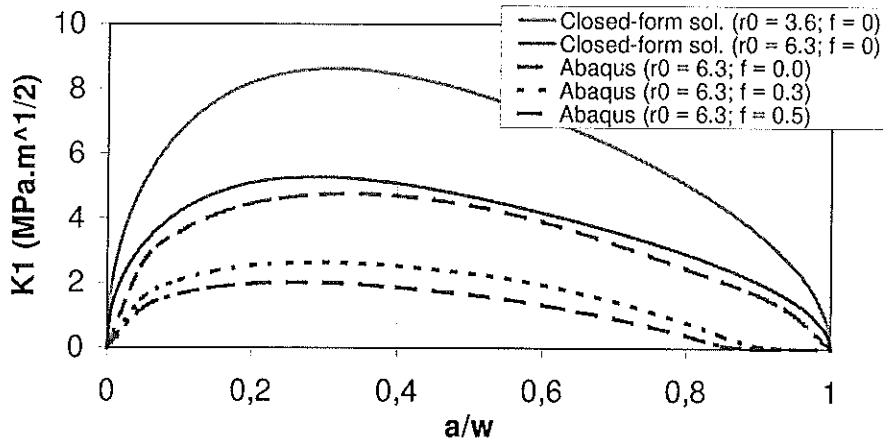


Fig. 3 – Stress Intensity factor given by FE simulations and the closed-form solution (S-SiC).

Simulations using the finite element code Abaqus were carried out to optimise the sandwiched-beam set-up. The parameters  $f$  (friction coefficient) and  $r_0$  (the relative prenotched flexural rigidity) were found to be essential concerning the crack propagation as it is shown in Fig. 3.

### Failure of precracked S-SiC bars by using the SENB technique

Once the ceramic bars are precracked, SENB (single-edge notched beam) tests are performed. The empirical relation

$$K_1 = \left( \frac{FL}{bw^{1.5}} \right) f(\alpha), \quad f(\alpha) = 1.5 \frac{\alpha^{0.5} [1.99 - \alpha(1-\alpha)(2.15 - 3.93\alpha + 2.7\alpha^2)]}{(1+2\alpha)(1-\alpha)^{1.5}} \quad (4)$$

relates the stress intensity factor to the applied force,  $F$ , dimensions  $L$ ,  $b$ ,  $w$ , and  $\alpha$  the relative crack length. A Weibull approach is followed (Fig. 4). The Weibull modulus is found equal to 24, which indicates a low scatter of the experimental results. The average toughness equals  $2.85 \text{ MPa m}^{1/2}$ . It is close to the value obtained by Riou [6] (i.e.,  $3.2 \text{ MPa m}^{1/2}$ ) for an S-SiC grade.

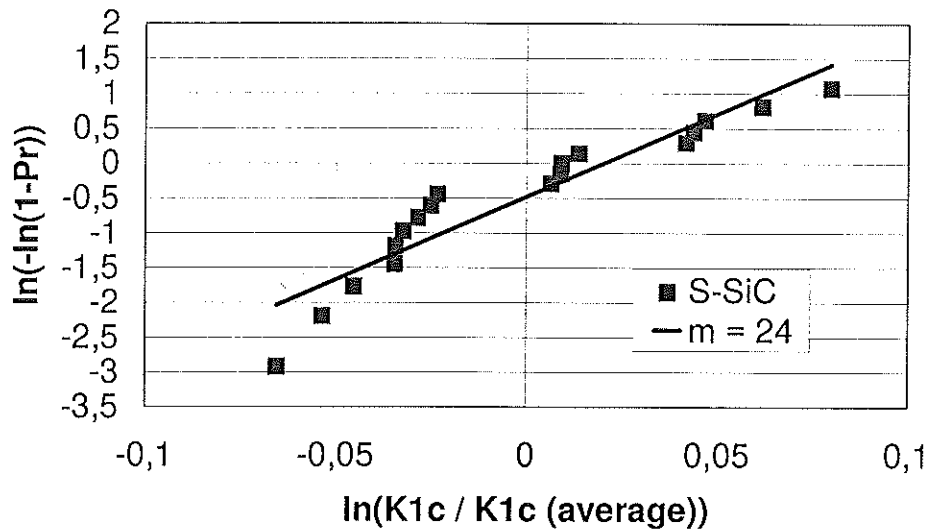


Fig. 4 – SENB tests, computation of Weibull parameters.

### CCS (Compact Compression Specimen) SiC-N Precracking

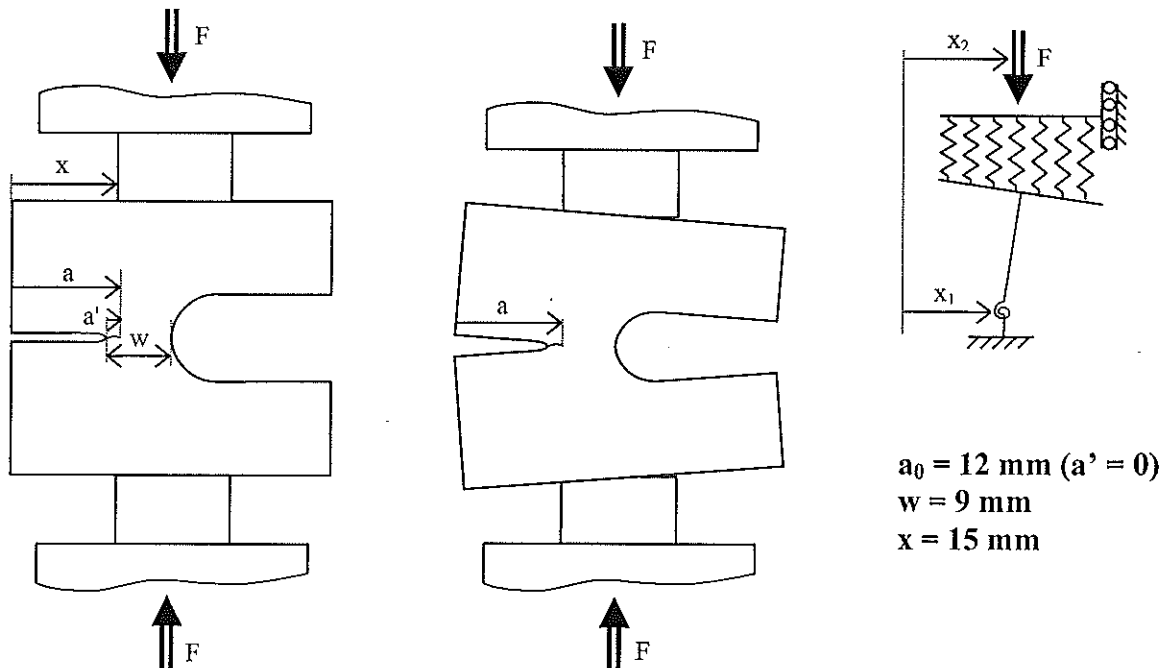


Fig. 5 – CCS precracking method.

To evaluate the ceramic toughness under dynamic loading conditions, a new geometry called CCS (compact compression specimens) is designed. To apply a dynamic loading, the specimen arms are put between two split Hopkinson pressure bars. A wave propagates along the Hopkinson pressure bar impacted by a striker. This wave is transmitted to the CCS specimen and opens the crack with a stress intensity factor rate of the order of  $1 \text{ MPa}\cdot\text{m}^{1/2}$  per  $\mu\text{s}$ . A set-up schematically drawn in Fig. 5 was used to precrack the specimen. The principle is the following: an applied load  $F$  whose co-ordinate is  $x_2$  deforms a steel anvil and causes a rotation of the CCS arms with respect to the notch plane. When the critical stress is reached at the notch tip, a crack develops within the ceramic. The crack propagates within a compressive stress field and stops. A simulation of the problem was performed with the finite element code Abaqus. Figure 6 shows the stress intensity factor as the function of the crack length. This plot predicts a stable propagation and arrest.

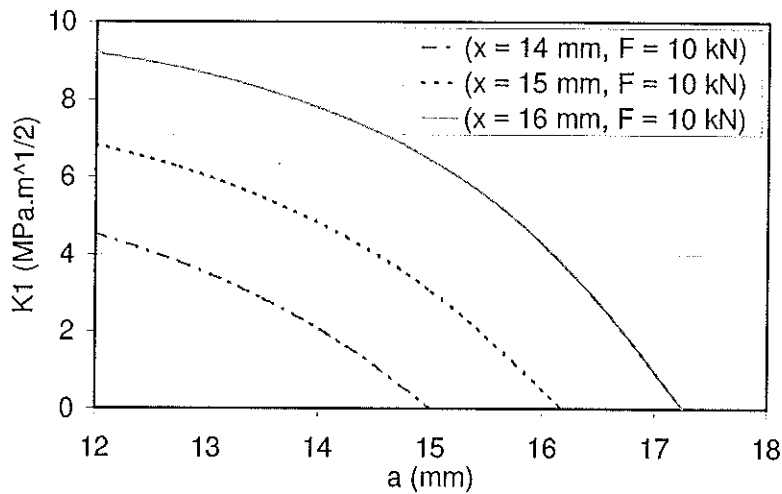


Fig. 6 – CCS precracking modelling (Abaqus).

The CCS precracking results are summarised in Table 2, where  $F_i$  and  $\alpha_i$  denote the applied load and the relative crack length just after crack initiation, respectively. The crack length  $a_i$  was measured by an image correlation technique.

Table 2. CCS precracking results (SiC-N).

Designation	x (mm)	$F_i$ (kN)	$\alpha_i = a'_i/w$ ( $F = F_i$ )	$F_m$ (kN)	$\alpha_c = a'_c/w$ ( $F = F_m$ )
9	15	18.3	0.08	24.0	0.18
5	15	7.14	0.04	10.0	0.22
6	15	11.2	0.17	12.0	0.17
3	15	7.2	0.05	10.0	0.17
4	15	14.0	0.31	14.0	0.31
7	15	7.2	0.07	10.0	0.21
8	15	9.23	0.22	10.0	0.23
10	15	8.3	0.04	10.0	0.18
16	15	9.75	0.22	11.0	0.25

An important scatter of the load level at initiation is observed as well as a correlation between this load and the relative crack length that develops in an unstable manner before arrest. Except for specimen No. 9, the higher the initiation load, the larger the relative crack length.

After initiation, the applied load was increased slowly. The maximum load varies between 10kN and 11kN, the scatter of the relative crack length is much smaller than previously.

### SiC-N CCS (Compact Compression Specimen) Failure

A device was necessary to break CCS samples under quasi-static loading to compare the quasi-static toughness with the dynamic data. The dynamic split Hopkinson pressure bar tests lead to a mixed mode  $K_I$  and  $K_{II}$  characterised by a crack angle at the notch tip close to  $45^\circ$ . Consequently, a device that allows also a mixed mode was investigated (Fig.7a). This set-up was modelled with the finite elements code Abaqus to predict the two stress intensity factors  $K_I$  and  $K_{II}$  and the angle at the inception of propagation. The influence of the position of the left cylindrical support is studied for two crack lengths. This position appears to change completely the two stress intensity factors. For small values, an axial displacement of the left face is impossible. The mode II loading dominates. The propagation will be characterised by a high crack angle with respect to the notch plane. If the position  $y$  is close to one half of the width, the load becomes virtually symmetric and the mode II becomes negligible compared to the mode I (Fig.7b).

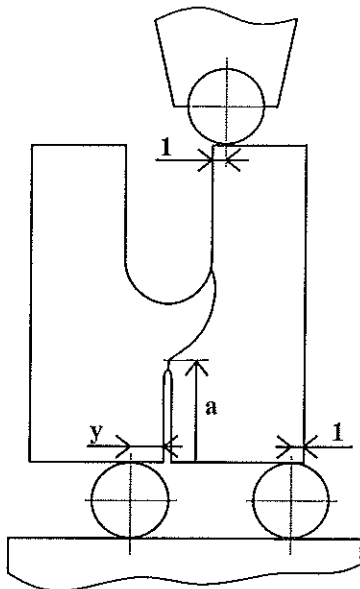


Fig. 7a - Schematic of CCS.

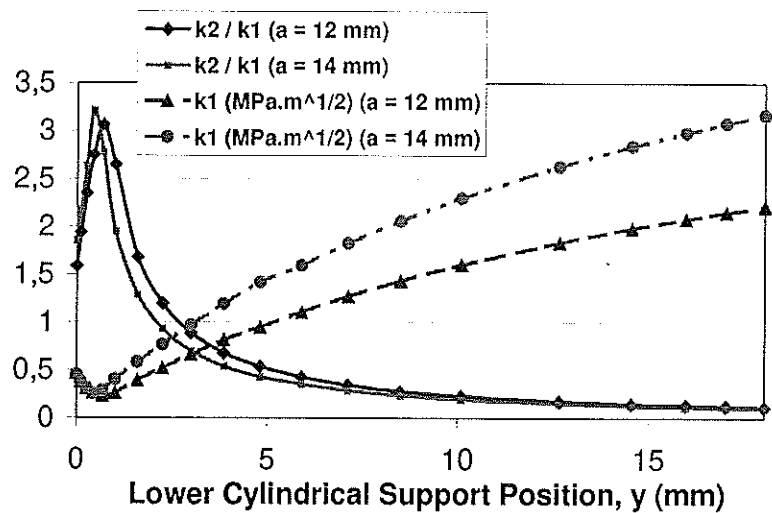


Fig. 7b - Stress intensity factors  $K_I$  and  $K_{II}$  vs. support position  $y$ .

The results of the CCS tests are presented in the following table. For each specimen, a simulation was performed. The two stress intensity factors  $K_I$  and  $K_{II}$  are computed with the crack opening displacement method. The toughness scatter is found to be very small.

Table 3. Quasi-static CCS toughness results (SiC-N).

Designation	$y$ (mm)	$a$ (mm)	$F_r$ (N)	$K_{Ic}$ ( $\text{MPa}\cdot\text{m}^{1/2}$ )	$K_2/K_1$	$\theta_{th}$
6	mode I	13.7	884	4.21	0.00	0
9	$y = 5$	14.7	3197	4.22	0.437	37.3
3	$y = 5$	14.1	2901	4.25	0.411	36.0
4	$y = 3$	14.0	4000	3.92	0.693	46.9
5	$y = 3$	14.6	4013	4.43	0.647	45.5

## CCS (Compact Compression Specimen) Dynamic toughness (SiC-N)

Dynamic tests were performed to evaluate the dynamic toughness of the same grade (SiC-N). To apply a dynamic load, a specimen arm was joined side by side to only one Hopkinson pressure bar. An elastic point element was put against the other face of the CCS specimen. This technique allows one to be independent of the parallelism of the two Hopkinson bar faces. One may wonder whether the absence of the second bar modifies the load pattern near the crack tip. A simulation of the problem was carried out with the explicit finite element code PamShock. It predicts a propagation inception for a time  $t = 77 \mu\text{s}$ . At this instant, the compressive wave has not reached the free surface of the CCS specimen (Fig. 8). The absence of the second Hopkinson pressure bar has no influence on crack initiation. Moreover, a high-speed camera is used during these tests. Picture no. 9 (Fig. 9) shows a failure of the right arm when  $t = 198.1 \mu\text{s}$ . The arms were indeed intact at  $t = 77 \mu\text{s}$ .

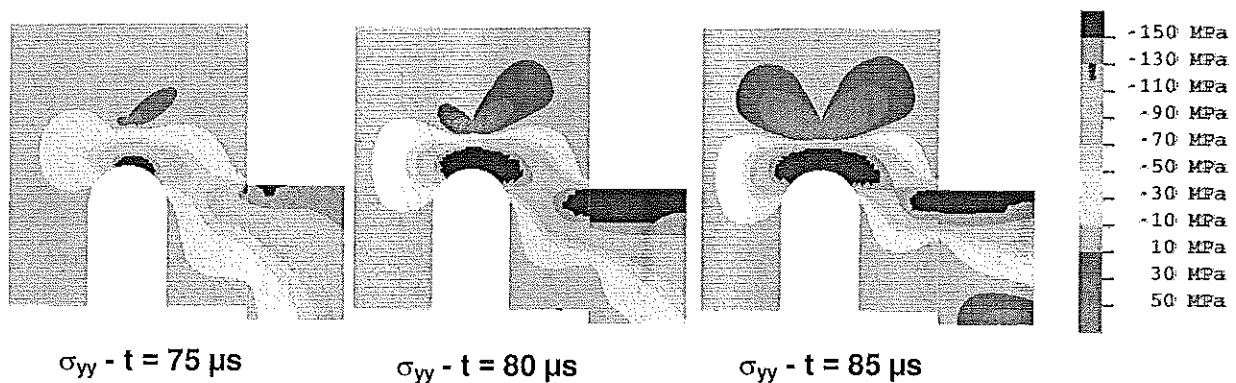


Fig. 8 – Simulation of a dynamic CCS test with Pamshock (3D Elastic Model).

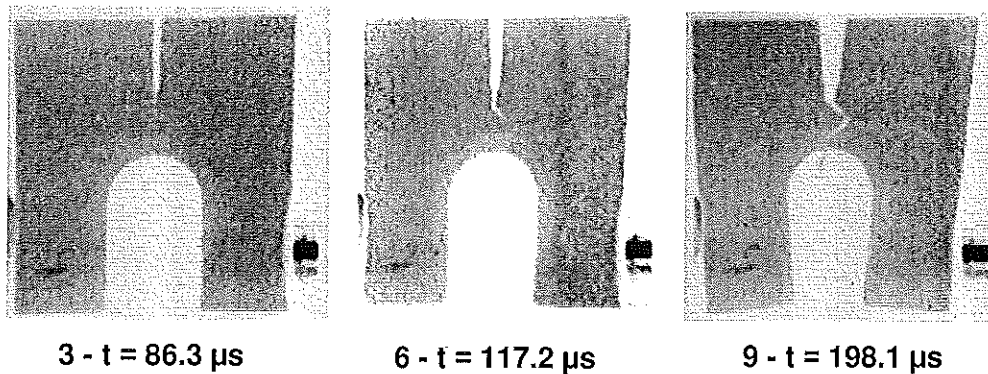


Fig. 9 – High-speed camera pictures, SiC-N 16, impact velocity = 4.9 m/s

The two stress intensity factors  $K_I$  and  $K_{II}$  histories are computed with a 3D elastic model. Their kinetics is given in Fig. 10. The ratio  $K_{II} / K_I$  decreases with time. The measurement of the kink angle allows us to deduce the ratio  $K_{II} / K_I$  and the toughness at this instant. The results are given in Table 4.

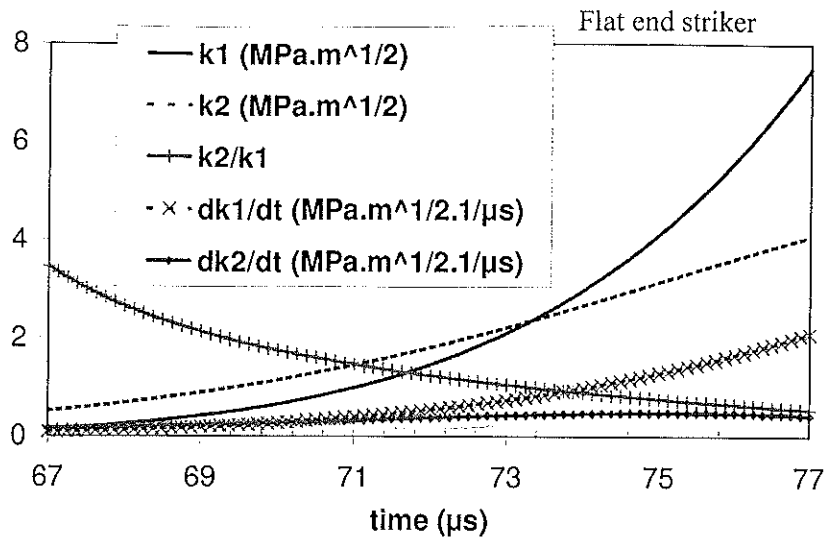


Fig. 10 – Stress intensity factors  $K_I$  and  $K_{II}$  vs. time predicted with Pamshock (elastic model).

Table 4. Dynamic CCS toughness results (SiC-N).

Designation	V impact (m/s)	a (mm) (left - righth)	$\theta_{\text{measured}}$ ( $^{\circ}$ ) (left - righth)	$K_{II}/K_I$	Initiation time ( $\mu\text{s}$ )	$K_{Ic}$ ( $\text{MPa}\cdot\text{m}^{1/2}$ )	$dK_I/dt$ ( $\text{MPa}\cdot\text{m}^{1/2}\cdot\mu\text{s}^{-1}$ )
8	5.1	14.5 - 15.5	31 - 36	0.33 - 0.41	74.4	6.3	1.5
16	4.9	14.35 - 15.1	37 - 42	0.43 - 0.54	77.0	7.5	2.1
7	4.7	14.1 - 14.8	37 - 42	0.43 - 0.54	77.0	7.5	2.1
Source	Gauge	Post-Mort.	Post-Mort.	$\text{Max}(\sigma_{\theta\theta})$	Pamshock	Pamshock	Pamshock

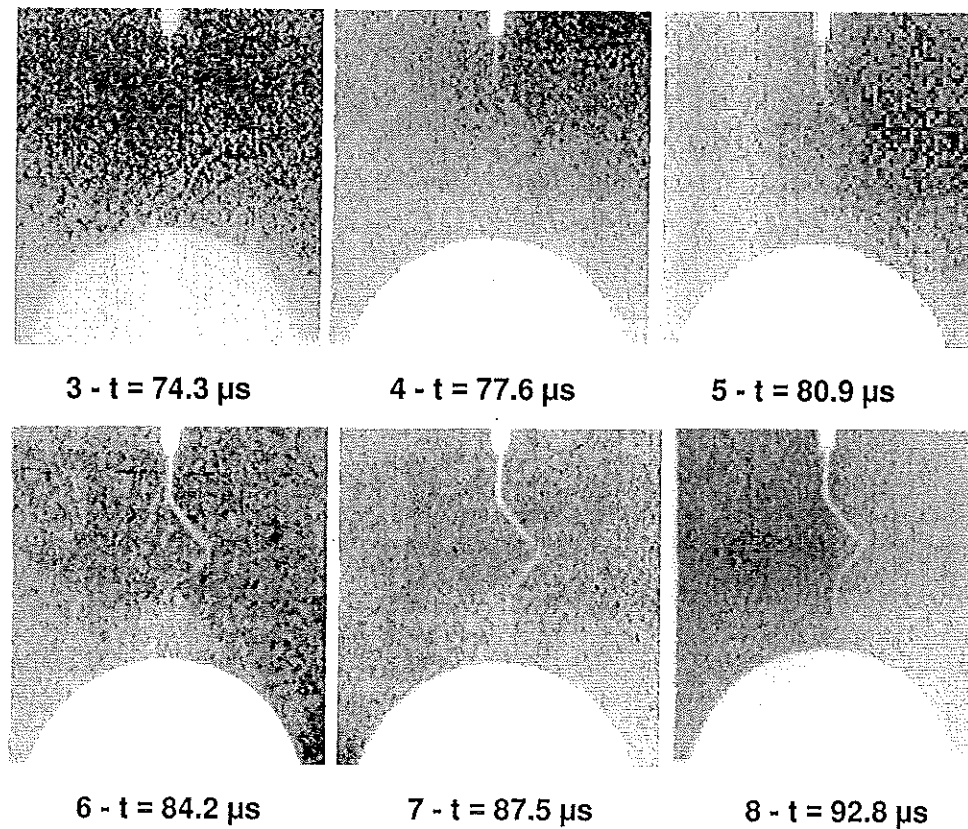


Fig. 11 – High-speed camera pictures, SiC-N 7, impact velocity = 4.7 m/s

The dynamic toughness values are close to the quasi-static data (Table 3). An increase of toughness with the toughness rate appears. Test No. 7 was carried out with the same conditions as test No. 16 (Fig.8), but a zoom was used in the crack propagation zone. A photograph was shot each 3  $\mu$ s. These pictures (Fig. 11) show a crack kinking between  $t = 74.3 \mu$ s and  $t = 77.6 \mu$ s. This result is also found when the propagation time is computed with PamShock (i.e.,  $t = 77 \mu$ s). To check this point, a damage model is used [8] (Fig.12). This modelling allows us to find again the shape of the crack and the timing of propagation.

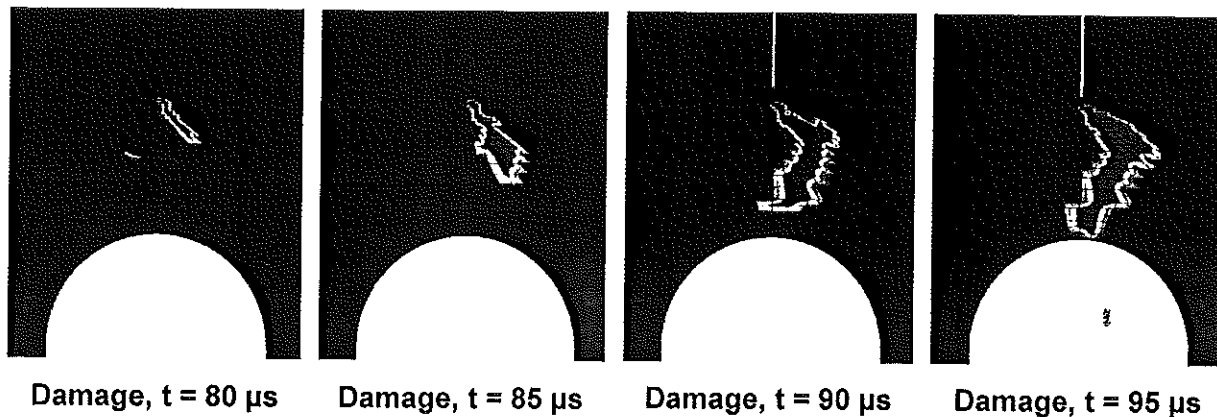


Fig. 12 – Damage field in a CCS configuration predicted by Pamshock.

## Conclusions

Two experimental configurations were designed and validated for two SiC grades (namely, S-SiC and SiC-N). In particular, a new set-up to precrack and break ceramics under quasi-static loadings of CCS samples was proposed. Toughness measurements were performed for the two ceramic grades. It was found that the scatter remains small in all cases. For the SiC-N grade, an increase of the toughness is observed under dynamic loading when compared to quasi-static data. All the toughness experiments were performed after precracking the samples. The toughness analyses were made possible only by a dialogue between experimental measurements and FE simulations, either elastic or with a damage model.

## References

- [1] Nunomura S. and Jitsukawa S., 1978. Fracture toughness evaluation for bearing steels by indentation cracking under multi-axial stress (in Japanese), *Tetsu to Hagane*, 64, S853.
- [2] Tetsuro N. and Toshimitsu F., 1988. Evaluation of fracture toughness for ceramic materials by a single-edge precracked beam method, *J. Am. Ceram. Soc.*, 71 [5], 328-33.
- [3] Marshall D.B., Ratto J.J. and Lange F.F., 1991. Enhanced fracture toughness in layered microcomposites of Ce-ZrO<sub>2</sub> and Al<sub>2</sub>O<sub>3</sub>, *J. Am. Ceram. Soc.*, 74 [12], 2979-87.
- [4] Pancheri P., Bosetti P., Maschio R.D. and Sglavo V.M., 1998. Production of sharp cracks in ceramic materials by three-point bending of sandwiched specimens, *Eng. Fract. Mech.*, 59 [4], 447-56.
- [5] Sglavo V.M., Bosetti P., Trentini E., Ceschini M., 1999. Sandwiched-beam procedure for precracking brittle materials, *J. Am. Ceram. Soc.*, 82 [8], 2269-72.
- [6] Riou P., 1996. Contribution à l'étude de l'endommagement du Carbure de Silicium lors d'un impact de basse énergie : application aux blindages, PhD dissertation, École Nationale Supérieure des Mines de Paris.
- [7] Denoual C., 1998. Approche probabiliste du comportement à l'impact du carbure de silicium: application aux blindages moyens, PhD dissertation, École Normale Supérieure de Cachan.
- [8] Denoual C. and Hild F., 2000. A damage model for the dynamic fragmentation of brittle solids, *Comp. Meth. Appl. Mech. Engrg.*, 183, 247-258.